Max-Planck-Institut für Quantenoptik

Technische Universität München

Atomic Cycles in Cavity QED

Karl Nicolas Tolazzi

Vollständiger Abdruck der von der Fakultät für Physik der Technischen Universität München zur Erlangung des akademischen Grades eines

Doktors der Naturwissenschaften (Dr. rer. nat.)

genehmigten Dissertation.

Vorsitzender : Prof. Dr. Frank Pollmann

Prüfende der Dissertation : 1. Hon.-Prof. Dr. Gerhard Rempe

2. Prof. Jonathan J. Finley, Ph.D.

Die Dissertation wurde am 02.03.2020 bei der Technischen Universität München eingereicht und durch die Fakultät für Physik am 10.09.2020 angenommen.

Abstract

In classical nonlinear media, interactions between single photons are negligible. However, a strong interaction can be reached using a single atom in a cavity. By driving a closed cycle in the atom's level structure we show parametric four-wave-mixing at the single photon level and a Zeno-blockade in the effective energy level structure. Extending to a multi-mode cycle, we show a giant cross Kerr nonlinearity between individual photons. The new platform shows novel physics in quantum nonlinear optics and is promising for real-time simulation of quantum systems.

Zusammenfassung

In klassischen nichtlinearen Medien sind Wechselwirkungen zwischen einzelnen Photonen vernachlässigbar. Eine starke Wechselwirkung kann jedoch mit einem einzelnen Atom in einem Resonator erreicht werden. Indem wir einen geschlossenen Kreislauf in der Levelstruktur des Atoms treiben, zeigen wir parametrisches Vierwellenmischen auf Einzelphotonenebene und eine Zenoblockade in der effektiven Energieniveaustruktur. Eine Erweiterung hin zu einem Multi-Moden-Kreislauf erlaubt die Demonstration einer riesigen Kreuz-Kerr-Nichtlinearität zwischen einzelnen Photonen. Die neue Plattform zeigt neuartige Physik in der nichtlinearen Quantenoptik und ist vielversprechend für die Echtzeitsimulation von Quantensystemen.

Contents

*Physics would be dull and life most unfulfilling
if all physical phenomena around us were linear.
Fortunately, we are living in a nonlinear world.*

*While linearization beautifies physics,
nonlinearity provides excitement in physics.*

Y. R. Shen
The Principles of Nonlinear Optics

1. Introduction

Performing research in general and doing a PhD thesis in particular is, aside from the scientific endeavor also a highly personal challenge. Therefore, before I motivate this thesis scientifically and put the performed research into context, I want to start on a personal note, with my own motivation to work in quantum optics and especially in cavity quantum electrodynamics (CQED). The spark for my deep fascination for CQED was ignited during my quantum optics lectures in my master's course, when I first heard about the ground breaking experiments at the École Normale Supérieure (ENS) in Paris by Serge Haroche and his collaborators. Their experiments demonstrated a live-observation of the birth and death of a single photon [1] and even allowed for nondestructive counting of the number of photons [2] that are trapped in a *photon box*. These are breathtaking experiments, bringing the abstract concept of a quantized energy portion of an electromagnetic field, a photon, to life. My deep fascination with experiments on the single photon level then led me to the Max Planck Institute of Quantum Optics where I could finally work in the field of CQED myself and satisfy my curiosity. I never regretted that decision and investigating this wondrous world of single photons and their interaction with single atoms still delights me every day and has ultimately also led to this thesis.

The quantization of energy in the theory of light-matter interaction was first introduced as merely a mathematical concept in a semi-classical theory of black-body radiation by Max Planck [3]. Soon after, Albert Einstein postulated for the first time that light itself is indeed quantized, a hypothesis with which he could explain the photoelectric effect [4, 5]. Although at first a controversial concept, the quantization of light with its newly coined name for the energy quantum, *photon*, was generally accepted after the discovery of Compton scattering [6]. As the history of the concept of a photon already shows, light is intertwined and to a certain extent only meaningful in conjunction with, the interaction with matter. A complete theory of light-matter interaction [7], combining quantum theory with special relativity, was only developed in the late 1940s by Feynman, Tomonaga and Schwinger, which earned them the Nobel prize in 1965. It is one of the most precisely tested theories to date. At its heart lies the interaction of a single charged particle, in the case of this thesis, the outermost electron of an atom, with a single photon. Although the interaction between one atom (electron) and one photon is conceptually easy, it is very challenging to observe experimentally. Experiments with single particles were once considered impossible [8] and still remain challenging because they require an extremely high amount of control and isolation from the environment. This also brings the problem that the interaction between a single atom and a single photon remains very weak. Still, these obstacles have been overcome by the gradual improvements in cooling [9, 10], and trapping of atoms [11, 12] and the dramatic increase of the interaction probability of one photon with one atom in a high finesse resonator [13]. This was only possible by vastly improved fabrication techniques of high quality mirrors for resonators that store and focus a photon repeatedly onto an atom. Another key ingredient is a coherent source of light, which was achieved with the invention of the laser in the 1960s [14]. This ultimately led to the development of experimental cavity quantum electrodynamics

(CQED) [15]. This field allows not only for the study of light-matter interaction at its most fundamental level, but for the mediation and investigation of interactions between photons as well. This photon interaction has been shown in experiments like single [16] and two photon blockade [17]. It also paves the way for all optical quantum computing, where photons are used as traveling qubits, which can be generated [18], stored [19], distributed to different computation nodes [20], or used as quantum gates [21].

Another field of research which, at first glance, appears to be very different, is electromagnetically induced transparency (EIT). In EIT, a resonantly driven, and therefore absorbing, medium becomes transparent when an additional coherent light field irradiates the medium. This happens in a three level atom, where the two lasers drive two distinct transitions in the medium to one common state. Each laser beam alone would excite the medium and drive transitions, but a quantum interference effect prevents excitation if both transitions are driven at the same time. This is because the transition probability amplitudes interfere destructively, rendering the medium transparent. EIT only happens in a narrow spectral window around the absorption line, where the two light fields are in two-photon resonance. The medium then evolves into a superposition state between the two originating states, called a dark state, as it can no longer absorb or emit photons of the applied laser fields. The phenomenon was first observed in the 1970s in the form of the related phenomena of coherent population trapping in gases [22] and more extensively researched in the 1990s [23–26]. An important aspect for many experiments on EIT was, in particular, the narrowness of the EIT window. A large change in the absorption of a medium in a small frequency window leads to a large change in the refractive index of the medium over an equally small frequency window (Kramers-Kronig relation). Such a rapid change in refractive index leads to an extremely low group velocity of light. As the transparency of one light beam is tunable with the intensity of the second light beam, the group velocity is also tunable, leading to the observation of slow light [27, 28] or even stopped light [29]. EIT systems are also interesting in the context of quantum information systems, as they allow for storage and subsequent readout of photons [30], controlled phase shifts [31], single photon switches [32], transistors [33, 34], and the implementation of photon-photon gates [35].

The two research fields mentioned so far, cavity quantum electrodynamics with a single atom and electromagnetically induced transparency, can be combined leading to the new field of single atom cavity electromagnetically induced transparency (CEIT), which only very recently started to be investigated [36–40]. Here, the system is implemented in a Λ-type atomic level scheme, with two atomic ground states which both exhibit transitions to one common excited state. One of the two laser beams used to drive these transitions in classical EIT is here replaced by the vacuum field of the cavity. This brings EIT to the level of individual photons. Due to the quantized nature of the strongly coupled CQED system, the atomic dark states of EIT become entangled with the photon number states of the cavity, leaving dark states with n and $n+1$ photons orthogonal in Hilbert space. This leads to the emergence of an infinite ladder of dark states that are separated by one photon each [41], compared to the single dark state that is created in normal EIT. The theoretical and experimental results in this thesis contribute to the deeper understanding of this still new, and largely unexplored field of CEIT.

Adding a transition channel between the two ground states of the CEIT system, leads to the formation of a closed cycle in the atomic energy level structure. A closed atomic cycle is defined here as a situation in which an atom is driven with multiple light fields addressing transitions of at least three different electronic states. These transitions form a closed loop in the energy level scheme of the atom. The CEIT system offers a plethora of ways to realize different cycles and investigate them in detail. As the cavity is an integral part of such a cycle, monitoring the output provides valuable insight into the internal cycling dynamics. Closed atomic level schemes represent the common thread of all experiments in this thesis which therefore carries the title "Atomic Cycles in Cavity QED".

The thesis is structured as follows: After a theoretical discussion of the system in **Section 2** and the introduction of some experimental techniques in **Section 3**, the thesis begins with the simplest possible experiment, driving the CEIT system with a weak probing field via the cavity. This already reveals many interesting aspects that are discussed in **Section 4**. One surprising effect manifests itself in the photon statistics of the output field, which shows long lasting oscillations. These are due to the generation of a new field that beats with the input drive. This new and tunable field is also measured spectrally via heterodyne detection, revealing that it is narrow-band. The generation of this new field is due to a four-wave mixing like process in a partially closed cycle in the atomic level scheme. This system still suffers from an incoherent part in the cycle, because the atom exhibits decay from an excited state. This sets the stage for further experiments in **Section 5**, where this incoherent part is replaced with a Raman transition, connecting the atomic ground states and therefore coherently closing the atomic cycle. This experiment reveals a plethora of interesting effects. First of all, the system shows four-wave mixing with an output field that exhibits full phase coherence to all input fields and a very narrow linewidth while exhibiting antibunching and sub-Poissonian behavior. Furthermore, the photon emission occurs continuously and produces significantly more photons than expected from an all resonantly driven atom in free space. A thorough theoretical treatment in this section reveals that this is due to the aforementioned ladder of dark states. The coherent drive between the ground states acts like an effective drive between different rungs of the dark state ladder. In a certain parameter regime a continuous quantum Zeno effect is observed, leading to a blockade of higher rungs than the first two of the ladder. This manifests itself as a generation of single photons during Rabi-oscillations between these two states. In a different regime, this Zeno-blockade is lifted, which allows the ladder to be climbed, resulting in a strong change of the photon statistics. From there on, it is interesting to extend the system by considering an additional atomic excited level and an additional cavity mode, because this allows for an atomic cycle, in which multiple fields are generated that can also interact. As **Section 6** shows, already the half-closed system with two cavity modes, proves itself as very rich with interesting phenomena in the interaction between the two cavity fields. This also nicely builds a bridge to the initial motivation of studying light matter interaction at its most fundamental level. In such a system, an atom interacts with single photons of two different fields at the same time and therefore mediates an effective interaction between the photons. In the dispersive regime, in which the atomic transition and the cavity mode exhibit a substantial detuning, this

expresses itself in the emergence of a giant cross Kerr nonlinearity, where photons in one cavity mode (gate) have a back-action on photons in the other cavity mode (probe). This is only possible due to the unique combination that CEIT offers, where the system inherits the steep change in refractive index from EIT and the single photon sensitivity from CQED. This system then allows for non-destructive and all-optical sensing of the average number of photons in the gate mode. Furthermore, already a single photon in the gate mode leads to a significant phase shift of the light field in the probe mode, which is especially interesting in the context of quantum information processing. Finally, **Section 7** presents an outlook into future experiments.

2. Theory

The theoretical foundation presented in this chapter is the prerequisite for all experiments in this thesis and sets the stage for the more specialized theoretical introduction in the respective chapter. This theoretical chapter provides a short insight into the general form of the light-matter interaction happening between a single atom and one quantized electromagnetic field mode of a cavity. Later on, the coupling of this system to another classical laser field is discussed and the emergence of cavity electromagnetically induced transparency is explained. This is complemented by a short discussion of how simulations in the real open quantum system are performed. In the end, the theory of heterodyne detection is explained, as this technique is needed to measure the phase of light for the experiments in Section 6 and the spectral properties of the emitted light field for the experiments in Section 5.

2.1. Cavity QED

The following is a very brief overview of the theoretical concepts. Several textbooks on the topic provide a more comprehensive coverage of the topic [15, 42]. Throughout the theoretical treatment $\hbar$ is set to one ($\hbar = 1$). When discussing light-matter interaction, a prime example used in many textbooks is the interaction of a single two-level atom with one electromagnetic field mode. This system is sufficiently easy to understand and already provides most of the insights needed for the understanding of more complex systems. A two-level system (TLS) typically has an infinitely lived ground state $|g\rangle$ and an excited state $|e\rangle$ that spontaneously decays into free space. The Hamiltonian of this simple system is given by:

$$H_a = \omega_a \hat{\sigma}^\dagger \hat{\sigma} \tag{2.1}$$

with the atomic transition frequency ω_a between state $|g\rangle$ and $|e\rangle$ and the raising (lowering) operator $\hat{\sigma}^\dagger(\hat{\sigma})$. The system and level scheme are shown in Figure 2.1(a). One mode of the quantized electromagnetic field with linear polarization, can be described as:

$$\hat{E}(z,t) = E_0(\hat{a}e^{i(kz-\omega t)} - \hat{a}^\dagger e^{-i(kz-\omega t)}) \tag{2.2}$$

with the field amplitude E_0, the frequency ω, the creation (annihilation) operator $\hat{a}^\dagger(\hat{a})$ of one photon in the field and the wave number k of the field. This is especially interesting in the context of a cavity, which consists of two mirrors facing each other, that reflect light back and forth between them. This confines the electromagnetic field spatially. Due to the boundary condition imposed by the mirrors, only light fields with frequencies which constructively interfere after multiple round trips in the cavity, can exist inside. Therefore a cavity separates out single modes from the continuum of modes that exist in free space. A cavity supports multiple modes whose spectral distance is called free spectral range (FSR) and depends on the distance between the mirrors. The following treatment considers only a single mode of the cavity (spectral width $2\kappa \approx 3\,\text{MHz}$), which is close to resonance to the atomic transition (spectral width $\gamma_{atom} \approx 6\,\text{MHz}$). All other
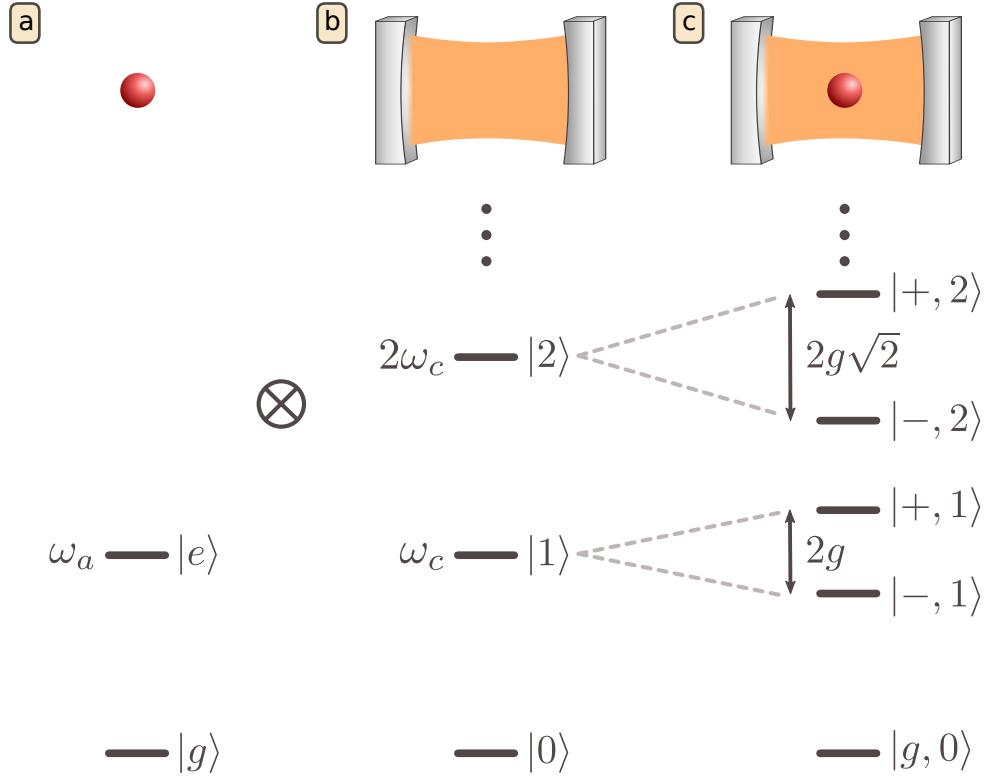
Figure 2.1: Sketch and according energy level diagram of the atom (a), the cavity (b) and the strongly coupled atom-cavity-system (c).

modes are spectrally far away from the atomic transition and therefore do not interact (FSR $\approx 500\,\text{GHz} \gg \gamma_{atom}, \kappa$). The Hamilton-operator in a cavity is given by:

$$H_c = \omega_c \hat{a}^\dagger \hat{a} \tag{2.3}$$

with the frequency of the considered cavity mode ω_c. The eigenstates to this Hamiltonian form a harmonic ladder of the form $|n\rangle$ with n photons inside of the mode. This is depicted visually in Figure 2.1(b).

The interaction between a two-level system with one electric field mode within a cavity via the dipole interaction can be described via the Hamiltonian (neglecting spatial and temporal variation of the field for now and assuming the polarization is parallel to the dipole moment):

$$H_i = \hat{d} \cdot \hat{E} \tag{2.4}$$

with the dipole operator $\hat{d} = d(\hat{\sigma}^\dagger + \hat{\sigma})$ and the transition dipole moment of the atom d. Introducing the coupling constant $g = E_0 d$ and neglecting fast rotating terms between the cavity frequency and the atomic frequency in the interaction picture (where the operators show an explicit time dependence), a process usually called rotating wave

approximation, results in the well known Jaynes-Cummings-Hamiltonian [43, 44]:

$$H_{JC} = H_c + H_a + H_i \tag{2.5}$$

$$H_{JC} = \omega_c \hat{a}^\dagger \hat{a} + \omega_a \hat{\sigma}^\dagger \hat{\sigma} + g(\hat{\sigma}\hat{a}^\dagger + \hat{\sigma}^\dagger \hat{a}) \tag{2.6}$$

The eigenstates to this Hamiltonian are given by the so-called *dressed states*:

$$|-, n\rangle = \cos\theta\, |g, n\rangle - \sin\theta\, |e, n-1\rangle \tag{2.7}$$

$$|+, n\rangle = \sin\theta\, |g, n\rangle + \cos\theta\, |e, n-1\rangle \tag{2.8}$$

where the eigenstates are of the form $|\text{atomic state}, \text{cavity photons}\rangle$ and θ is the mixing angle defined as:

$$\tan\theta = \frac{2g\sqrt{n}}{\Delta_{ac} + \sqrt{4g^2 n + \Delta_{ac}^2}} \tag{2.9}$$

with the detuning between atom and cavity of $\Delta_{ac} = \omega_a - \omega_c$. If the atomic and cavity frequency match each other, an excitation is exactly half in the atom and half in the cavity and the energies in the new ladder of eigenstates are:

$$E_n^\pm = n\omega_c \pm g\sqrt{n} \tag{2.10}$$

This ladder is anharmonic as it scales with $\sqrt{n}$, which is the basis for many interesting effects like single-[16] and two-photon blockade [17] or photon gateway [45]. A sketch that illustrates this ladder is shown in Figure 2.1(c). The effects of the detuning between the atom and the cavity become important in Section 6 and are discussed in more detail there.

2.2. Cavity EIT

So far the theory has involved only a two-level atom that is now extended to a three-level atom, which results in new and somehow unexpected effects. The new atomic level scheme is shown in Figure 2.2(a). It involves two atomic ground states $|1\rangle$ and $|2\rangle$ that do not decay and an excited state $|3\rangle$. The cavity is coupled to the transition $|1\rangle \leftrightarrow |3\rangle$ with coupling constant g and a detuning of $\Delta_{ac} = \omega_{a,12} - \omega_c$, where $\omega_{a,12}$ is the atomic transition frequency and ω_c the cavity frequency. In addition there is a classical coherent laser beam irradiating the system, whose frequency is close to the $|2\rangle \leftrightarrow |3\rangle$ transition with a detuning of $\Delta_{23} = \omega_{a,23} - \omega_{l,23}$, where $\omega_{a,23}$ is the atomic transition frequency and $\omega_{l,23}$ the laser frequency. This laser beam induces transitions with a resonant Rabi frequency of Ω_{23}. The Hamiltonian of the new system in the rotating wave approximation and transformed to a rotating frame reads:

$$H_{CEIT} = (\Delta_{ac} - \Delta_{23})\hat{\sigma}_{22} + \Delta_{ac}\hat{\sigma}_{33} + g(\hat{\sigma}_{13}\hat{a}^\dagger + \hat{\sigma}_{13}^\dagger \hat{a}) + \Omega_{23}(\hat{\sigma}_{23}^\dagger + \hat{\sigma}_{23}) \tag{2.11}$$

where $\hat{\sigma}_{kl}$ denote the atomic transition operators of the form $\hat{\sigma}_{kl} = |k\rangle\langle l|$ $(k, l = 1, 2, 3)$ for $k \neq l$ and the atomic population operator for $k = l$. The zero-point of energy is chosen
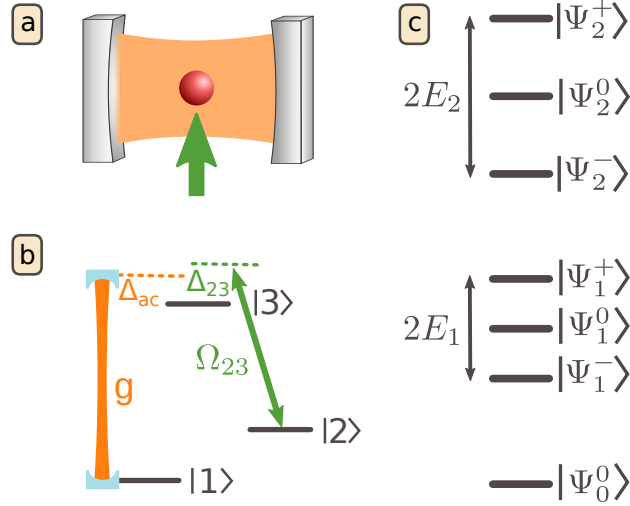
Figure 2.2: (a) shows the atom (red dot) within the cavity and the transverse classical drive (green arrow). (b) shows the atomic level scheme including the cavity and the detunings. (c) shows the first three manifolds in the infinite effective ladder of eigenstates.

at state $|1\rangle$. In the case of vanishing two-photon detuning $\Delta_{ac} = \Delta_{23} = 0$ the following eigenstates are solutions to the stationary Schrödinger equation:

$$\left|\Psi_n^0\right\rangle = N_n^0 \left[\Omega_{23}\left|1,n\right\rangle - g\sqrt{n}\left|2,n-1\right\rangle\right] \tag{2.12}$$

$$\left|\Psi_n^\pm\right\rangle = N_n^\pm \left[g\sqrt{n}\left|1,n\right\rangle + \Omega_{23}\left|2,n-1\right\rangle + E_n^\pm\left|3,n-1\right\rangle\right] \tag{2.13}$$

where the bare states are of the form $|$atomic state, cavity photons$\rangle$. The normalization factors are $N_n^{(0)} = \left(\Omega_{23}^2 + g^2 n\right)^{-1/2}$ and $N_n^\pm = \left(2g^2 n + 2\Omega_{23}^2\right)^{-1/2}$. The energies of the states in the chosen basis are given by:

$$E_n^0 = n\omega_c \tag{2.14}$$

$$E_n^\pm = n\omega_c \pm \sqrt{ng^2 + \Omega_{23}^2} \tag{2.15}$$

This new basis forms a ladder of manifolds where each value for the excitation number n in the system has three states. This ladder is shown in Figure 2.2(c). The states $\left|\Psi_n^\pm\right\rangle$ are called bright states, because they exhibit a component of the excited atomic state $|3\rangle$. Furthermore the splitting between them increases in each manifold, as their splitting depends on the number of excitations in the system, thereby forming a nonlinear ladder. The states $\left|\Psi_n^0\right\rangle$ are called dark states, as they do not have any contribution from the atomic excited state, but only from the ground states. They form a linear energy ladder, because the energy spacing between state n and n+1 is constant. If the system is probed and the drive is resonant to the dark states, the absence of atomic excitation renders the system transparent for a laser beam. That is the reason this effect is called cavity electromagnetically induced transparency (CEIT) in analogy to the long known effect in gases [22] and has already been described in several studies [36, 37, 40, 41, 46].

2.3. Heterodyne detection

The most employed technique to measure a light field is photon-detection (or photon-flux detection). This detection method measures the energy flux (photons per second) that hits a detector surface, which usually consists of a semiconductor photodiode. By measuring only the energy of a light field, part of the information about the field is lost, as the phase and amplitude are not accessible but only the time averaged intensity (depending on the bandwidth of the detector). In certain types of experiments, it is crucial to also measure the phase of the light field. A direct detection of the oscillating electromagnetic field is unfortunately not possible with photodiodes, as these are not fast enough by several orders of magnitude. There is a solution that mitigates these disadvantages, known as heterodyne detection. First employed in the beginning of the 20th century in the radio frequency domain, it soon became a standard technique for many high frequency applications and is extremely common in daily life applications such as radio receivers and mobile phones. Later this technique was also transferred to the optical domain, where it is called optical heterodyne detection. With this technique, the very high frequency of the electric field to be measured is transferred to an easily accessible frequency domain where off-the-shelve electronics can measure and process the signal, without losing any information about the original electric field. The basic principle of this so called down-mixing relies on interference between different light waves. When two waves are mixed, the superposition exhibits a beat signal at the sum and difference frequency of the two fields. The difference frequency is usually chosen to be in the MHz regime by engineering of the field with which the signal is mixed. The frequency of the sum frequency component in optical heterodyne is then too high to pass the measurement electronics. The amplitude of this beat signal is the product of the two wave amplitudes. Therefore it is possible to use one strong beam, usually called the local oscillator (LO), to down-mix and amplify the signal of a weak signal beam. This chapter only discusses the most important aspects. The treatment here follows [47], where more details of the scheme can be found. The electric field operator of a single mode of the electromagnetic field can be written as:

$$\hat{E}(t) = \sqrt{\frac{\hbar\omega}{2\epsilon_0 V}}(\hat{a}_\omega e^{i\omega t} + \hat{a}_\omega^\dagger e^{-i\omega t}) \tag{2.16}$$

where $\hat{a}_\omega (\hat{a}_\omega^\dagger)$ is the annihilation (creation) operator of a photon with frequency ω and V is the volume under consideration. As the local oscillator is generally in a bright coherent state $|\alpha\rangle$, it can be treated classically and is assumed to be monochromatic at frequency ω_{LO} (as it stems from a low bandwidth laser). So the electric field of that beam can be described as:

$$E_{LO}(t) = \sqrt{\frac{P_{LO}}{2\epsilon_0 Sc}}(e^{i\omega_{LO}t} + e^{-i\omega_{LO}t}) \tag{2.17}$$

with the beam power P_{LO}, the beam's cross sectional area S and the speed of light c. Superimposing the signal beam with electric field operator $\hat{E}_p$ and the LO beam at a

beam splitter results in superpositions of the fields at both outputs. These exhibit a phase difference, which is reflected in the sign. The new field operators are:

$$\hat{E}_\pm = \frac{\hat{E}_p(t) \pm E_{LO}(t)}{\sqrt{2}} \tag{2.18}$$

These lead to two current operators in the two photodiodes of the balanced detector $\hat{J}_\pm(t) = \hat{P}_\pm q_e/\hbar\omega$, where q_e is the elementary charge and $\hat{P}_\pm = \epsilon_0 S c \hat{E}_\pm^2$ are the power operators of both mixed fields. The output signal of the balanced photo detector is a voltage proportional to the amplified difference between the two currents $\hat{V}(t) = G(\hat{J}_+ - \hat{J}_-)$, with gain factor G. Thus the voltage operator for one frequency component ω of the signal beam becomes:

$$\hat{V}(t) = G\sqrt{\frac{\eta_{LO} P_{LO} q_e^2}{\hbar \omega_{LO}}} \left(\hat{a}_\omega e^{i[(\omega-\omega_{LO})t-\theta]} + \hat{a}_\omega^\dagger e^{-i[(\omega-\omega_{LO})t-\theta]} \right) \tag{2.19}$$

with the detection efficiency of the local oscillator beam η_{LO} and the phase difference between the respective mode and the local oscillator θ. As an example, the measured voltage of a coherent state $|\alpha_p\rangle$ with frequency ω_p in the probe beam is:

$$V(t) = \langle \alpha_p | \hat{V}(t) | \alpha_p \rangle = 2G\sqrt{\frac{\eta P_{LO} P_p q_e^2}{\hbar^2 \omega_{LO} \omega_p}} cos[(\omega_p - \omega_{LO})t - \theta] \tag{2.20}$$

where η is the total detection efficiency for the beat signal consisting of the quantum efficiency of the detector, optical path losses and the mode matching factor of the interference. This formula shows that the power of the local oscillator can be used to amplify the usually weak signal of the probe beam. The difference frequency, $\omega_p - \omega_{LO}$, is usually chosen by changing the local oscillator frequency such that it can be comfortably processed by the balanced photodiode, whilst still being high enough to avoid the high noise floor close to DC frequencies. Therefore, it is comparably easy to achieve shot-noise limited operation by choosing an appropriate difference frequency.

2.4. Quantum simulations

All real systems exhibit dissipation to the environment. That is called an open quantum system and it is possible to calculate ensemble averages in such systems via the density matrix formalism. The dynamics of an open system can be calculated using a Lindblad master equation of the form:

$$\dot{\rho} = -i[H, \rho] + \kappa(2\hat{a}\rho\hat{a}^\dagger - \hat{a}^\dagger\hat{a}\rho - \rho\hat{a}^\dagger\hat{a}) + \sum_m \Gamma_m(2\hat{\sigma}_m\rho\hat{\sigma}_m^\dagger - \hat{\sigma}_m^\dagger\hat{\sigma}_m\rho - \rho\hat{\sigma}_m^\dagger\hat{\sigma}_m) \tag{2.21}$$

where ρ is the density matrix, κ is the cavity-field decay rate, and Γ_m the polarization decay rate of an atomic decay channel. The summation runs over all possible decay

channels. In some of the experiments to follow, a second cavity mode is implemented. For these, an additional mode appears in the master equation as well. The first term in this equation describes the coherent evolution of the system and is called the *von Neumann equation*. It results directly from the Schrödinger equation for a density matrix. The other terms describe the dissipation processes. This master equation can be simplified in the form of the Lindblad super-operator $\mathscr{L}$:

$$\dot{\rho}(t) = \mathscr{L}\rho(t) \tag{2.22}$$

By integration of this equation the time dependence of any operator $\hat{O}$ can be calculated as:

$$\left\langle \hat{O}(t) \right\rangle = \mathrm{tr}\left(\hat{O} e^{\mathscr{L} t} \rho(0) \right) \tag{2.23}$$

This is especially interesting for the second-order correlation function, which can be derived from the quantum regression theorem [48] to:

$$\left\langle \hat{a}^{\dagger}\hat{a}^{\dagger}(\tau)\hat{a}(\tau)\hat{a} \right\rangle = \mathrm{tr}\left(\hat{a}^{\dagger}\hat{a} e^{\mathscr{L}\tau} (\hat{a}\rho_{ss}\hat{a}^{\dagger}) \right) \tag{2.24}$$

with the steady-state density matrix ρ_{ss}. That means the system is moved out of equilibrium by annihilation of a photon and the photon number during the subsequent equilibration process back to the steady state is observed. Throughout the theoretical investigation in this thesis, the master equation is solved numerically using QuTip [49].

3. Experimental setup

A characterization and detailed description of the experimental apparatus can be found in [50]. The system that is investigated is a single ^{87}Rb atom, in precisely prepared and addressable internal electronic states, inside of a high-finesse Fabry-Pérot resonator of very small mode volume. This leads to strong coupling of specific atomic transitions to resonator modes. The whole system is within an ultra high vacuum (UHV) chamber with a residual pressure of the order of 10^{-10} mbar [51]. The experiments presented in this thesis require loading and trapping of a single atom inside of the cavity, control over its internal degrees of freedom via lasers, detection of light retrieved from the system and evaluation of the data. These subsystems will be described within this chapter.

3.1. Cavity

A very detailed report about the cavity is given in [50]. All the parameters given within this chapter are for a wavelength of 780 nm unless otherwise noted. The cavity used in these experiments is a Fabry-Pérot resonator with a finesse of $\mathscr{F} = 195\,000(2000)$. All experiments use the TEM$_{00}$-mode (but different longitudinal modes) of the cavity. The spacing between the mirrors is 295 µm, which leads to a free spectral range of around 500 GHz. The mirror distance can be tuned macroscopically, because one of the mirrors is mounted on a inch-worm-motor, that allows a tuning range from 100 µm to over 1 mm. Fine tuning of the mirror distance is done via a piezo tube, that houses the second mirror. An active length stabilization, based on a Pound-Drever-Hall lock [52], keeps it resonant to the atomic transition under investigation and is described in [51]. The cavity is asymmetric, with one mirror having a much higher transmittance than the other ($T_1 = 2.5(5)$ ppm, $T_2 = 17.8(5)$ ppm). The losses sum up to $L = L_1 + L_2 = 11.0(5)$ ppm, which leads to a field decay constant of $\kappa/2\pi = 1.5$ MHz. The birefringence (≈ 180 kHz) is well within the cavity linewidth and therefore negligible. The mode waist, where the field falls off to $1/e$ of its initial amplitude, is $w_0 \approx 20$ µm and the Rayleigh length $z_0 \approx 1.7$ mm. Because of this long Rayleigh range, it is justified to make the assumption that the cavity field is cylindrical, and the coupling constant does not considerably change along the cavity axis (except for mode overlap effects, which only play a role in Section 6.3.2).

Some of the experiments in this thesis require strong coupling to two atomic transition at the same time. This demands that an integer multiple of the free spectral range exactly spans the frequency difference of these two transitions. A natural choice is the D1 and D2 line of rubidium, as these are the strongest transitions from the ground state of that atom. Due to a combination of selective light shifts with the dipole traps to fine tune one transition with respect to another and a macroscopic change of the cavity length via the inch-worm motor, it was possible to achieve this situation. A detailed description of this process is presented in the PhD thesis of C. Hamsen [53].

3.2. The atom

The atom that is used within this thesis, is ^{87}Rb which is one of two naturally occurring isotopes (with a relative abundance of around 27%) of the metal rubidium and is solid at room temperature. It is quasi-stable with a half-life of $5 \cdot 10^{10}$ years [54]. As it only has one electron in its outermost electron shell, it exhibits a comparably easy level structure. The electronic ground state of ^{87}Rb is the $5S_{1/2}$ state. The so called D-lines of rubidium are strong transitions from this ground state, arranged in a transition doublet, originating from the fine structure of the atom due to spin-orbit coupling. Especially important for cooling and trapping is the D2-line, with a transition wavelength in vacuum of 780.2 nm. This provides a cycling transition, in which the atom stays during repeated excitation and de-excitation processes due to selection rules. The D1-line, with a vacuum wavelength of 795.0 nm, does not have such a cycling transition due to fewer states in the hyperfine structure of the excited state manifold. Furthermore ^{87}Rb exhibits a hyperfine splitting of around 6.8 GHz in the ground state due to the coupling of the total angular momentum of the electron to the angular momentum of the nucleus. The level scheme is depicted in Figure 3.1. In the experiment, a magnetic guiding field is applied, lifting the degeneracy of the magnetic sub-levels and leading to a Zeeman-splitting on the order of a few hundred kHz.
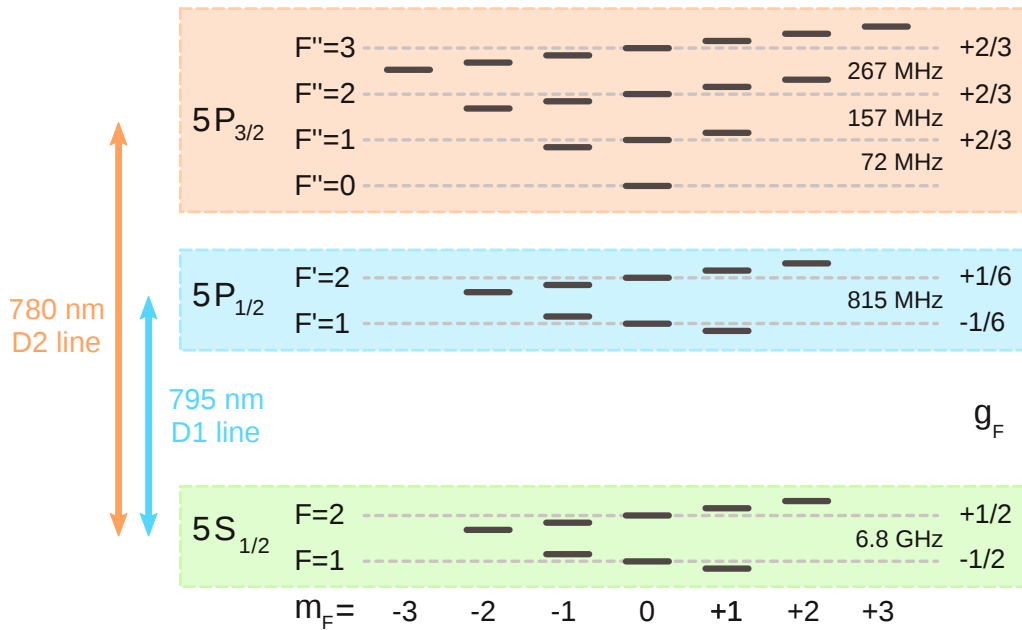

Figure 3.1: Level scheme of the ^{87}Rb atom, depicting the fine-structure splitting, the hyperfine splitting, the magnetic sub-levels, their Landé-factor g_F.

3.3. Loading and trapping of atoms

The experiments require the trapping of a single atom at the center of the cavity mode for a reasonable trapping time on the order of seconds. Rubidium is a solid metal so

the first step towards trapping a single atom is the evaporation by heating of a small metallic sample in a dispenser. The next step is the trapping of a cloud of atoms in a magneto-optical trap (MOT), which takes around 2 s. Subsequent molasses cooling leads to a temperature of the cloud of 4 μK [50]. The cavity is around 25 cm above the MOT. This distance is traversed by an atomic fountain that launches the cloud of atoms upwards with a speed such that they have their turning point, and therefore minimal kinetic energy, at the center of the cavity. A red detuned standing wave dipole trap [55] at 797.5 nm is focused transversely into the cavity, as can be seen in Figure 3.2(a). This trap attracts atoms to the maximum of its intensity, where the induced dipole of the ground state of the atoms maximally interacts with the light field by lowering the energy. When the atoms fall into this potential valley caused by the red detuned trap, they also gain kinetic energy that would lead to an escape out of the field again. To prevent this and
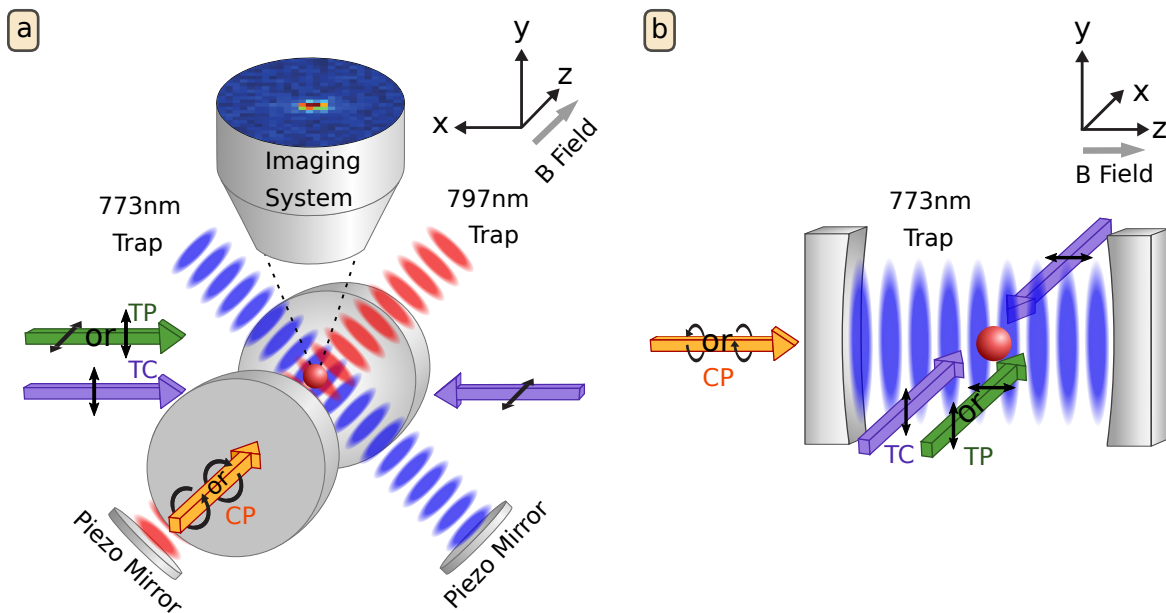
Figure 3.2: Two different views of the experimental setup and the beam paths. (a) shows a view along the cavity axis where the transverse traps are depicted but the intra-cavity trap is not shown. Also shown is the imaging system on top of the cavity. (b) shows a view transversely to the cavity axis and only depicts the blue intra-cavity trap, whereas the two transverse traps are left out. The abbreviations TP,TC and CP denote laser beams configurations and stand for transverse probe, transverse cooling and cavity probe respectively. The picture in (a) is a modified version of the sketch in [53].

eventually trap the atoms, an additional cooling field irradiates the atoms. This impinges transversely to the cavity direction, is retro-reflected and has linear polarization that is rotated by 90° in the retro-reflected beam. The light is red detuned by around 30 MHz to the $|F = 2\rangle \longleftrightarrow |F'' = 3\rangle$ transition of the D2-line of the atom. This leads to an intra-cavity Sisyphus-type cooling in all direction [9, 56]. Even though this is a cycling transition,

off-resonant scattering from $|F'' = 2\rangle$ leads to a decay into the $|F = 1\rangle$ ground state, that is repumped by a transverse $|F = 1\rangle \leftrightarrow |F' = 2\rangle$ laser on the D1-line.

In addition to the red detuned transverse dipole trap, there are two additional blue detuned standing wave traps. Blue detuned traps confine atoms to nodes of their field as they act repulsively. One of these two addition fields is within the cavity at 773.1 nm (7 free spectral ranges away from the D2-probing field). An additional blue detuned transversal trap of ≈ 772 nm is enabled once the first cooling cycle is finished. These in total three traps together confine the atoms to one point in a three dimensional optical lattice. The trap depth in this three-dimensional optical lattice was determined in a former thesis to $U \approx -h \cdot 70\,\text{MHz} = k_B \cdot 3.3\,\text{mK}$ for the red transverse trap, $U \approx h \cdot 18\,\text{MHz} = k_B \cdot 0.8\,\text{mK}$ for the blue transverse trap and $U \approx h \cdot 24\,\text{MHz} = k_B \cdot 1.1\,\text{mK}$ for the blue intra-cavity trap [53]. Due to the probabilistic nature of the whole loading process, the unknown number and position of trapped atoms and possible movement of the atoms within the cavity by tunneling processes from one lattice site to another, it is necessary to image the atoms. This also allows for optimizing the MOT duration to get exactly one atom most of the time (Poisson distributed). Imaging is done by collecting the scattered light during cooling via a high NA (0.47) objective with a magnification of 16.5, which consists of 5 spherical lenses for aberration compensation and an additional focusing lens. Details about the objective can be found in [57]. The collected light is then measured via an EMCCD camera with an integration time of 300 ms. The final diffraction limited resolution of the imaging system is $1.07(1)\,\mu\text{m}$. This allows for a precise determination of the atom position in the imaging plane. The out-of-focus blur of the atom image shows a linear dependence of the width of a Gaussian fit on the position along the y-direction. This can be used to deduce the atom's position transversely to the focal plane. The back-reflection mirrors of the transverse optical traps can be tuned in position via piezo elements, which then itself moves the position of the whole standing wave and with it the atom. Together with a live-fit of the atomic position, this allows for two-dimensional active position stabilization of the atom to maximize the coupling constant [53]. Control over the third dimension along the cavity axis is not yet possible but a control via optical tweezers is under construction.

3.4. Internal control of the atom

A key ingredient to all experiments presented here, is the control over the internal electronic degrees of freedom of the atom. A faithful preparation into a specific state and a subsequent controlled interaction with light of the right frequency and polarization is a prerequisite for all experiments. As shown in Figure 3.2, the setup basically allows for optical access in three different configurations. For a magnetic field along the cavity axis, the beam labels and their corresponding possible polarizations are shown in Table 1.

Possible are the depicted polarizations and superpositions of them. All beam directions allow for quick and easy exchange of the input light, as everything is fiber coupled and can be changed by fiber to fiber connectors to have different inputs.

Name	Abbreviation	Direction	Polarization
Cavity probe	CP	Cavity	σ^+, σ^-
Transverse cooling	TC	Transverse	linear $\perp$ linear
Transverse probe	TP	Transverse	$\sigma^+ + \sigma^-, \pi$

Table 1: Summary of the optical axes and their possible polarization.

3.5. Detection of light
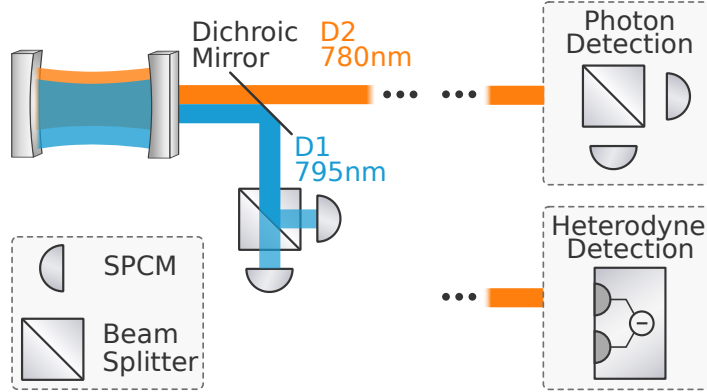
Figure 3.3: The detection setup with two different detection methods. The D1 light is always detected in single photon counting modules (SPCM), whereas the D2 detection method can be easily switched between a photon detection via SPCMs or a heterodyne detection.

The light that leaves the out-coupling mirror is first split into the different wavelengths that are used in the experiment by a dichroic mirror. The D1 light has a fixed beam path and is detected via two single photon counting modules (SPCM) in a Hanbury Brown and Twiss configuration (HBT) to allow for the measurement of second order photon correlation functions. The second-order correlation function is an important measure that helps to understand the dynamics of the underlying system. It can be described as the probability to detect a second photon after time τ, when a first photon was detected at time t. The function is normalized to the photon rate. In a formula it can be expressed as:

$$g^{(2)}(t, \tau) = \frac{\left\langle \hat{a}^\dagger(t)\hat{a}^\dagger(t+\tau)\hat{a}(t+\tau)\hat{a}(t) \right\rangle}{\left\langle \hat{a}^\dagger(t)\hat{a}(t) \right\rangle \left\langle \hat{a}^\dagger(t+\tau)\hat{a}(t+\tau) \right\rangle} \tag{3.1}$$

with $\hat{a}$ ($\hat{a}^\dagger$) the photon annihilation (creation) operator. A common simplification is setting $t = 0$ and assuming that the expectation value $\left\langle \hat{a}^\dagger(t)\hat{a}(t) \right\rangle$ is time independent. This leads to the usual expression for the $g^{(2)}(\tau)$ photon correlation function: $g^{(2)}(\tau) = \langle \hat{a}^\dagger \hat{a}^\dagger(\tau)\hat{a}(\tau)\hat{a} \rangle / \langle \hat{a}^\dagger \hat{a} \rangle^2$. Experimentally, the temporal resolution for photon detection times is 1 ns, but coincidence windows of typically 10 ns to 20 ns are used for computation

of correlation functions. This allows for binning of the correlation function to increase the number of events in each bin. To eliminate influence of detector dead-time and after-pulsing, photons are only correlated between different detectors within the HBT setup. The D2 light is coupled into a fiber, where it either goes to a photon detection setup in HBT configuration or to a heterodyne setup to allow for the detection of the electric field properties like the phase. The total detection efficiency for light from intra-cavity field to detection via the SPCMs is around 26% for the D2-light [53], which is composed of the intrinsic out-coupling efficiency of the cavity of 57%, a detector quantum efficiency according to the datasheet of 65%, a fiber coupling efficiency of 80% and a 90% efficiency for the rest of the optical elements (fiber and other optical elements not shown in picture for simplicity). From a cycling measurement, where exactly one D1 photon is generated for each D2 photon (see Appendix Appendix C), the total D1 light detection efficiency from intra-cavity field to detection with SPCMs is deduced to be 34%.

Heterodyne detection setup

The theoretical foundation is described in Section 2.3. The heterodyne detection setup is shown in Figure 3.4 and was built over the course of the Master thesis of Jonas Neumeier [47], in which a more detailed overview is given. The optical part of the heterodyne setup is shown in part (a). The output light field from the cavity (probe field) is mixed with a strong local oscillator and the two output beam paths are recorded by a differential photodiode. The quantum efficiency of the photodiode is determined to be 96(1)%. The output voltage of the photodiode follows the expression as derived in Section 2.3 and therefore oscillates with the difference (beat) frequency $\omega_b = |\omega_{LO} - \omega_p|$. In the experiment this difference frequency was chosen to 60 MHz, by adjustment of the local oscillator frequency due to two main reasons. First, 60 MHz is a good compromise between the available detector bandwidth and an already significantly reduced noise floor in comparison to DC voltages. Second, there is the possibility of back-scattering of light from the detection setup to the cavity. This can be severe because the local oscillator is strong, on the order of mW. Even though all components are anti reflection coated, back-scattered light on the level of nW is still possible, which would already surpass the typical probing power and therefore significantly influence the experiment. It is therefore advisable to operate the detection setup with a LO beam as far detuned as possible from the cavity resonance, to which the probe is typically resonant.

It would be possible to digitize the beat signal directly to extract the field quadratures, which unfortunately has severe disadvantages. With a beat frequency of 60 MHz, digitization of the signal requires at least twice the sampling rate according to the Nyquist-Shannon-theorem [58]. Together with a reasonable voltage resolution of at least 14 bit, this would lead to a data rate of around 210 MB/s. Although this is within the writing capabilities of current state of the art solid-state hard drives (SSD) (and surpasses normal HDDs), it is still impractical, as it would only allow for very short measurement intervals and would require a computationally heavy data evaluation. Therefore the experimental setup uses an analog down-mixing scheme to retrieve the field quadratures which is shown in Figure 3.4(b). The beat signal is split into two paths and mixed with two
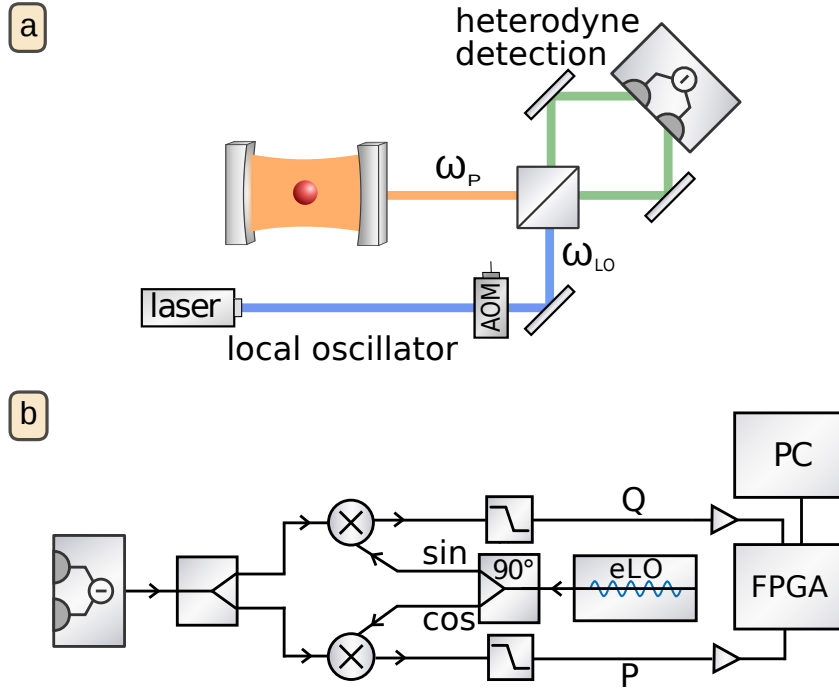
Figure 3.4: (a) shows the optical part of the heterodyne detection setup. The cavity output with frequency ω_p is mixed with a local oscillator at frequency ω_{LO} and measured via a differential photo diode. (b) shows the analog electronic down-mixing circuit, in which the output of the balanced photodiode is split, then mixed with an electronic local oscillator (eLO) at ω_{eLO}, then low-pass filtered and finally digitized by an FPGA and a PC.

sinusoidal signals called electronic local oscillator (eLO) with $\omega_{eLO} = 60\,\text{MHz}$, whereas one of them is 90° phase shifted with respect to the other. The resulting signal consists of the sum and difference frequency (which is close to DC). A low-pass filter transmits only the close to DC components, which are called quadratures Q and P. These are then digitized by a field-programmable gate array (FPGA) and stored on a PC with a time resolution of 250 kHz and therefore with a significantly lower data rate than without the analog down-mixing stage. The amplitude and phase of the electric field of the probe light can then be calculated by (see [47] for a detailed derivation):

$$A = \sqrt{P^2 + Q^2} \tag{3.2}$$
$$\phi = \arctan(-P/Q) \tag{3.3}$$

In the first mode of operation, the laser generating the local oscillator is split into two beams, where one beam probes the atom-cavity setup from which the output is then superimposed with the frequency shifted local oscillator beam. This allows a measurement of the influence of the experiment on the probe light in terms of phase and amplitude, which gives valuable information about the underlying physics. On a technical note, this requires the periodic recording of the reference phase between local oscillator and

probe beam to compensate for drifts in the optical path lengths, as described in [47]. The second mode of operation within this thesis is the operation without an explicit cavity drive. There, the heterodyne detection acts as a precise spectrum analyzer for an output field from the cavity with initially unknown frequency. In this type of experiment the local oscillator frequency is scanned via an AOM. The quadratures only show a non-vanishing amplitude if the following condition is satisfied: $|\omega_{eLO} - \omega_b| < \omega_{LP}$, where ω_{LP} is the cut-off frequency of the low-pass filters of the quadrature lines. This represents a scanning window which produces a non-zero output signal only when the probe frequency ω_p lies within this window. This leads to a frequency dependent amplitude and therefore a spectrum of the output light field.

3.6. Data acquisition and evaluation

While the atom is trapped, a sequence of experiments runs with a repetition rate of around 1 kHz. A typical sequence consists of a cooling interval, followed by a state preparation into a specific Zeeman substate and finally the actual experiment as shown in Figure 3.5.
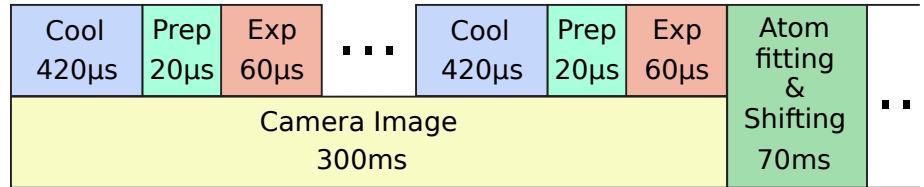
Figure 3.5: A sample experimental sequence consisting of cooling, state preparation and an experimental pulse. During the full sequence the camera is exposing. After one image the atom position is determined and adjusted.

Each pulse is characterized by a specific set of laser beams that illuminate the atom. The raw data in our experiment consists of time-tagged photon detection events registered by the single photon counting modules (SPCM) and is written to a hard disk. As this is only an unstructured list of photon clicks, the click stream is evaluated and linked to specific pulses in the sequence and their timestamps are changed to relative values with respect to the pulse starting time. Due to the probabilistic loading scheme and potential movement of the atom during the measurement it is necessary to continuously measure the exact position of the atom within the cavity. The atoms are imaged during 300 ms, which is the granularity for postselection on atom position later on. From such an atom picture, it is possible to determine the three dimensional coordinate of the atom from light that was scattered from the atom during cooling as described in the chapter about atom trapping. This imaging technique can detect the number of atoms in the cavity, as well as their positions. The atomic coordinate is determined in real time, while the experiment runs, and is stored in a PostgreSQL database for fast and parallel access. After determining to which atom image, pulse, and sequence each photon click belongs, the data is stored in the data format HDF5 [59]. This is an ultra fast and highly structured binary data format that is used in many areas of scientific research, especially in big data use cases. One
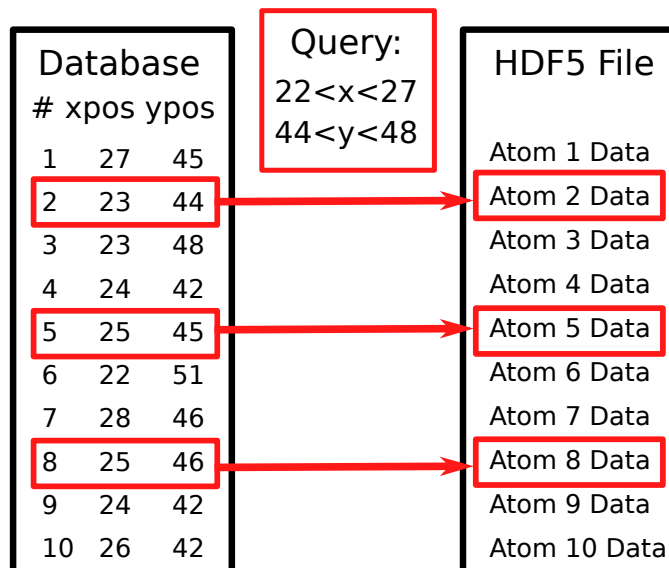
Figure 3.6: The sketch shows the interplay between the data format HDF5 and the database, when a specific atom position is requested.

distinct feature is that it allows for random access of the data without reading the full file. This accelerates selective accesses that are needed in the experiment to postselect data. Postselection of specific data portions is necessary, because the atom position varies due to the probabilistic loading scheme. To ensure a constant coupling constant and a specific overlap with the driving lasers, it is necessary to only use data collected while the atom was at the right position within the cavity. Postselection of data is done via a query to the database, where a range of x,y and possibly z positions is specified. The database then returns the IDs of all atoms that fulfill this condition for a specific measurement. The datasets corresponding to these atom IDs are then selectively read from the HDF5 file as sketched in Figure 3.6.

CavityTools

Over the course of this PhD thesis, an extensive evaluation tool called *CavityTools* was created to simplify the data evaluation process and enable the user to evaluate measurements without having detailed knowledge how the data is internally stored and how the postselection is done in detail. Most measurements, whether it is a phase and amplitude measurement via heterodyne detection, a Raman transfer, or a transmission measurement, can be evaluated with a single line of code. This significantly simplifies the data evaluation process and gives a high level of flexibility and fast workflow due to the abstraction from low level data access. A complete sample code for a spectrum is given in Listing 1.

```python
from Measurement import get_measurement_object

# position postselection of the atom
postselection = {
'x_min': 23,
'x_max': 33,
'y_min': 30,
'y_max': 38,
'y_dev_min': 10,
'y_dev_max': 18
}
# name of measurement, interval and
# cutoffs for evaluation
measurement_name = '180529_Open_NM_set12'
interval = 'Probe'
cutoff_start = 0.0
cutoff_end = 20.0

m = Measurement.get_measurement_object(measurement_name,
                                       selection=postselection,
                                       m_type='nm', x_range=[-1, 2])
x_data = m.get_xdata()
y_data = m.scan(interval, line='2',
            cutoff=[cutoff_start, cutoff_end])
```

Listing 1: Code showcasing how a spectrum can be obtained with the *CavityTools* package.

Validation of evaluation programs

The computer programs that evaluate the photon click data in the form of timestamps and compute spectra and correlation functions from that, are rather complex. It is highly nontrivial to ensure correctness over several thousand lines of code. Throughout this thesis, a new approach to that intrinsic problem was implemented. As already described in Section 2.4, it is possible to simulate the physical system via a master equation approach. Another approach is the quantum Monte-Carlo calculation of individual trajectories of the system and subsequent averaging [60]. These two approaches evolve towards the same results. The advantage of the Monte-Carlo approach is that it produces single traces and not averages of the system. This allows to really see when e.g. a dissipation operator is applied, or, in other words, when a photon decays out of the cavity. This is the analog process to a photon detection in the real experiment. Therefore the Monte-Carlo approach generates results of the exact same format as the real experiment. Using

the same evaluation programs used for the real experiment for theoretical data, and comparing the result with the master equation solution ensures that the programs used are indeed valid and do not skew the data.

3.7. State detection on an open transition

^{87}Rb exhibits hyperfine structure with two distinct ground states with a splitting of 6.8 GHz. Because electric dipole transitions between the two states are forbidden, the effective lifetime of the energetically higher lying state $|F = 2\rangle$ is infinite for all experiments within this thesis. Detecting whether the atom is in state $|1\rangle$ or $|2\rangle$ is crucial for many experiments performed, as this is the basis for benchmarking any state preparation as well as determining the beam waist. There are mainly two state detection techniques available. One technique uses the features of a strongly coupled atom-cavity system by probing the cavity. When the atom is in the not strongly-coupled ground state the cavity exhibits the same countrate of photons as when empty. On the other hand if the atom is in the strongly-coupled ground state, the normal-mode splitting blocks light from entering the cavity [61]. The other technique, which proved to result in a higher fidelity in the present experimental situation, relies on the excitation of the atom from the side, with a beam that is resonant to the transition from one of the ground states to an excited state and collection of scattered fluorescence light. As the atom emits in a solid angle of 4π, it is crucial to have a high NA objective collecting as many photons as possible. With an atom in a cavity, where the atomic transition used for probing is strongly coupled to the cavity mode, the efficiency increases considerably as discussed in [62]. This experiment then results in two different distributions of detected photon numbers in a specific probing time. These two distribution for the two ground states can be discriminated. For the non-coupled atomic ground state this typically leads to $\bar{n}_{uc} = 0$ photons except for dark counts of the detector or far off-resonant scattering. For the coupled ground state this leads to a Poissonian distribution with a mean of $\bar{n}_c$. Choosing a discrimination threshold n_d then allows for state detection with a fidelity depending on the overlap between both distributions. This method is typically applied on a cycling transition of the atom, as this results in a very high number of scattered photons, because there is no decay channel to uncoupled states. Unfortunately, this is not possible in the experiments of this thesis, as all the experiments demand a cavity that is resonant to an open transition. In such a system, the cavity-assisted florescence technique runs into problems, because each scattering event has a high probability to decay into uncoupled states of the system, where no further photons can be scattered. This limits the number of photons that can be scattered in total significantly. The atom can either decay into uncoupled Zeeman substates in the otherwise coupled ground state or into the other, uncoupled, ground state. Decay into uncoupled Zeeman substates can be mitigated by usage of the TC arm in Figure 3.2. Using this back-reflected axis has many benefits: Due to the spatially varying polarization of counter propagating laser beams in lin⊥lin configuration, the atom does not experience dark states within one ground state manifold anymore. Another technique to avoid pumping into dark state in the Zeeman-manifold is by active switching between different polarizations, which leads

to similar results [63]. An additional advantage of counter-propagating laser beams is that the radiation pressure is balanced and it is therefore less likely to kick the atom out of the trapping potential. The resulting photon distribution for a 10 μs probing, for an atom previously prepared in a specific ground state, is shown in Figure 3.7. Previous experiments showed that preparation of a specific ground state manifold is possible with a fidelity of more than 99%. This means any limit on the state detection fidelity found by this experiment stems from the detection, and not the preparation process. For the
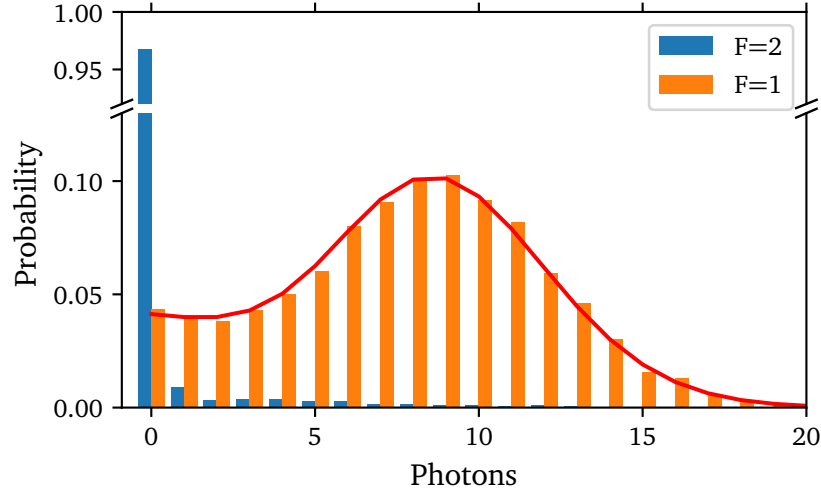

Figure 3.7: Photon detection probability for different previously prepared ground states for a exposure time of 10 μs. The red line is a theoretical fit to the data as described in the main text.

experiment, the cavity was resonant to $|F = 1\rangle \leftrightarrow |F'' = 1\rangle$ on the D2 line and the atom was probed for an exposure time of 10 μs with a transverse beam (TC axis) resonant with the cavity with a power of 0.2 μW. As can be seen, the dark ground state manifold $|F = 2\rangle$ almost always leads to zero photons. The problem is that the other manifold, $|F = 1\rangle$, also leads to zero photons in around 4.4% of cases, because it is possible for the first scattering event to already leave the atom in an uncoupled state. Furthermore, the chance that photons are undetected is non-negligible because the photon can either scatter out of the cavity into 4π or can be lost in the detection setup with its limited detection efficiency of around 26% for the D2 light. The overlap between both distributions for the dark and the bright ground state limits the discrimination fidelity to a little above 95%. This does not improve for a longer probing time, as there is a characteristic amount of photons that can be scattered given by the experimental situation. Also shown in the figure is a fit to the distribution for $|F = 1\rangle$, which is derived from the complex two-parameter fit function as derived in [63, 64], in which a detailed analysis of state detection on open transitions can be found. This allows for determination of the signal rate to $\Gamma_1 = 954(3)$ kHz and the decay rate into uncoupled states to $\Gamma_0 = 41(1)$ kHz. The theoretical lower limit for the state detection infidelity is given by $P = \Gamma_0/(\Gamma_0 + \Gamma_1) = 4.1\%$, which is close to the measured value. The achieved state detection fidelity is sufficient for the applications in this thesis.

3.8. Raman transitions and determination of the beam waist

In many experiments presented in this thesis, it is necessary to be able to drive direct transitions between the two ground state manifolds. The frequency splitting of 6.8 GHz between them, would allow to couple these states by irradiation of the system with a microwave. Unfortunately, this approach comes with plenty of disadvantages. The microwave's relatively long wavelength does not allow for strong focusing, which means the atom-light coupling remains low and the coupling Rabi frequency Ω_{12} (for the transition between the ground states $|F=1\rangle \leftrightarrow |F=2\rangle$) is limited to low values. Furthermore, past tests in the existing setup have shown that it was not possible so far to expose the atom with microwaves without disturbing the cavity length stabilization, preventing this mode of operation. There is an alternative approach for the coupling between two ground states called stimulated Raman transitions. There, two ground states are coherently coupled by two light fields, which exhibit a detuning to each other fitting the energy difference between the two ground states. The excited state is driven detuned from resonance to prevent actual excitation and subsequent spontaneous decay. The excited state is merely a mechanism to provide a virtual state with non-vanishing transition probability, that both fields can address. These kind of transitions have been used in many different systems with the purpose of coherent transitions between the ground states [65–67] and for cooling to the motional ground state [68–70]. A sketch of the Raman transitions with their respective polarization is shown in Figure 3.8(a). The virtual state was ≈ 30 GHz blue detuned to the D1-line transition of the atom. In the experiment in
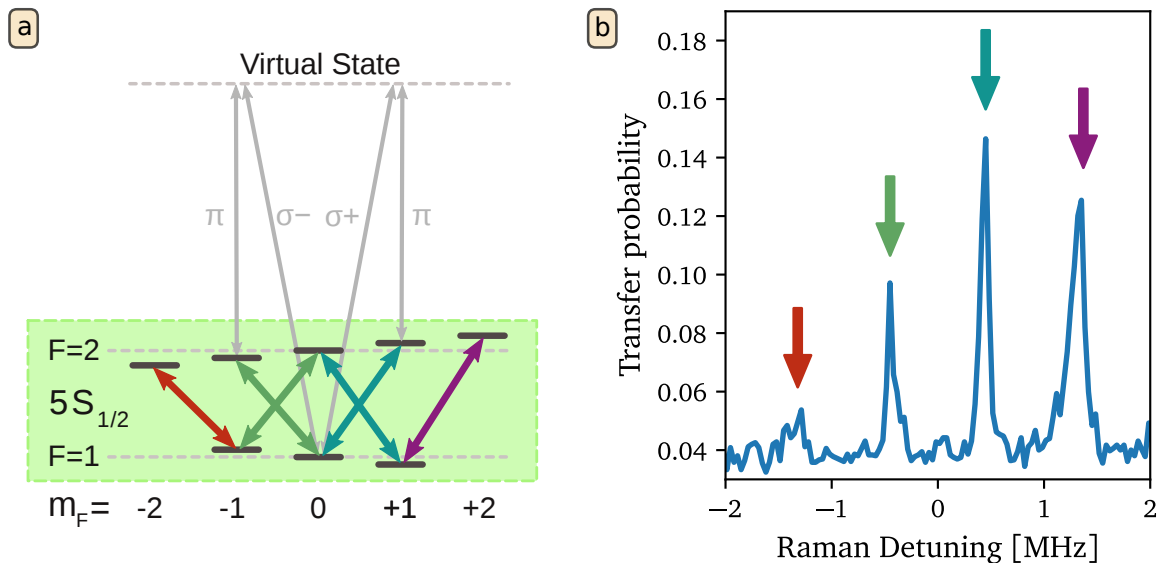
Figure 3.8: (a) shows a sketch with the possible Raman transitions in the chosen polarization of the laser beams. (b) shows the transfer probability to the other ground state against the detuning of one of the Raman beams. The arrow color corresponds to the arrow color in plot (a) and shows which peak belongs to which transition.

part (b), the system is initially prepared in one of the ground states, then the Raman lasers illuminate the system for a specific time. One of the two Raman lasers is scanned in frequency and whenever the combination of both is resonant to a transition between any ground states, a population transfer to the other ground state manifold is induced. This transferred population can be detected with the subsequent state detection as described in Section 3.7. The aforementioned state detection infidelity is visible as a baseline to the measurement. The spectrum shows four peaks, that stem from transitions between different Zeeman-substates, because their energetic degeneracy is lifted due to the magnetic guiding field. The manifold is more populated towards positive magnetic sub-levels as can be seen from the asymmetry of the peak heights. The frequency splitting between two peaks is given by:

$$\Delta E = h\Delta_f = g_F \mu_B m_F B \tag{3.4}$$

where g_F is the Landé-factor, μ_B the Bohr magneton, m_F the magnetic hyperfine state and B the magnetic field. The measured splitting corresponds to a magnetic guiding field at the atom of 0.6 G.

Determination of the beam waist

For many experiments throughout this thesis, it is important to know the Rabi frequency that a light field in the TP beam arm (see Figure 3.2) induces in the atom. In general, the Rabi frequency of a driven transition is given by:

$$\Omega = \frac{\vec{d} \cdot \vec{E}}{\hbar} \tag{3.5}$$

where $\vec{d}$ is the dipole vector and $\vec{E}$ is the electric field vector of the driving field. If both are parallel, this simplifies to the dipole matrix element d and the electric field amplitude E. In a real atom, the dipole matrix element can be expressed as:

$$d = d_{\text{trans}} \langle F_1, mF_1, F_2, mF_2 | F, mF \rangle \tag{3.6}$$

where d_{trans} is the dipole matrix element for the respective transition and

$$\langle F_1, mF_1, F_2, mF_2 | F, mF \rangle = \text{CG} \tag{3.7}$$

is the Clebsch-Gordon coefficient for coupling of two states with spins (F_1, mF_1) and (F_2, mF_2). For a Gaussian beam, the electric field at the focus can be expressed as:

$$E = \sqrt{\frac{4P}{c\epsilon_0 \pi w_0^2}} \tag{3.8}$$

with the power P, the speed of light c, the vacuum permittivity ϵ_0 and the beam waist in the focus w_0. In practice, it is not easy to measure Rabi oscillations between the ground state and an excited state, because of the fast decay time of the excited state.

It is nevertheless possible to calculate the Rabi frequency, when the exact waist of the beam at the position of the atom is known. This can be determined by driving Raman transitions between the two ground states and calculating the beam waist from the measured Rabi frequency between the ground states. This has several advantages. The ground states do not decay, which means also a slow Rabi oscillation survives long enough to be measured and also a read out technique of the atomic state is readily available. Experimentally, the atom is prepared in the ground state manifold $|F = 1\rangle$. Then the
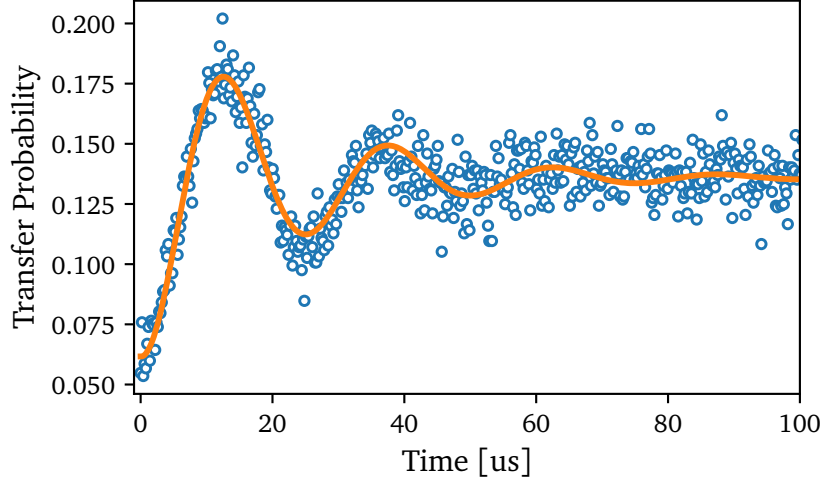
Figure 3.9: Shown is the transfer probability to ground state $|F = 2\rangle$ for different interrogation times of the Raman lasers (blue) and a damped sinusoidal fit (orange) to determine the Rabi frequency.

Raman lasers interrogate the atom on the transition $|F = 1, m_F = 1\rangle$ to $|F = 2, m_F = 2\rangle$ for a variable time. Subsequently, a state detection is performed and the transfer probability is calculated from repeated measurements. A scan of the interrogation time of the Raman beams is shown in Figure 3.9. A damped Rabi-oscillation is clearly visible and the frequency is determined via a sinusoidal fit. The damping is due to dephasing between the ground states. The theoretical value for the Rabi frequency is given by:

$$\Omega_{\text{eff}} = \frac{\Omega_1 \Omega_2}{\Delta} \tag{3.9}$$

where $\Omega_{1,2}$ are the resonant Rabi frequencies of the partial transitions and Δ is the detuning to the real atomic state, to which the Raman-transfer couples. Inserting Equation 3.5 and Equation 3.8 into this equation and solving it for the waist results in:

$$w_0 = \sqrt{\frac{4CG_1 CG_2 d^2 \sqrt{P_1 P_2}}{\hbar^2 \Delta \Omega_{\text{eff}} c \epsilon_0 \pi}} \tag{3.10}$$

For the transversal beam in the experiment this leads to an effective waist of:

$$w_0 = 150(10)\,\mu\text{m} \tag{3.11}$$

The error on the waist is estimated, because atoms that are trapped at different positions experience different driving strengths. The value given here is the average beam waist for a broad spread of atoms. Furthermore, this effective beam waist is not the actual beam waist of the TP arm but it includes potential losses along the path after the point at which the power of the beams is measured and it also includes misalignment. Nevertheless this effective beam waist is very useful, because it is possible to derive all other Rabi frequencies on the same beam arm (TP), by measuring the power of the respective beam.

4.   Incoherently closed cycle and wave mixing

4.1. Introduction

The experiments in this section explore the properties of a cavity EIT system under the influence of a weak probing field through the cavity. Especially the wave-mixing capabilities of such a system are in the focus in this section as this system already exhibits a partially closed atomic cycle. A new field is created which expresses itself as a beat, that is visible in the photon statistics of the light emitted by the cavity. A heterodyne measurement reveals further spectral properties of the field. First results of the system used within this chapter were already presented and discussed in a previous PhD thesis [46].

4.2. Results
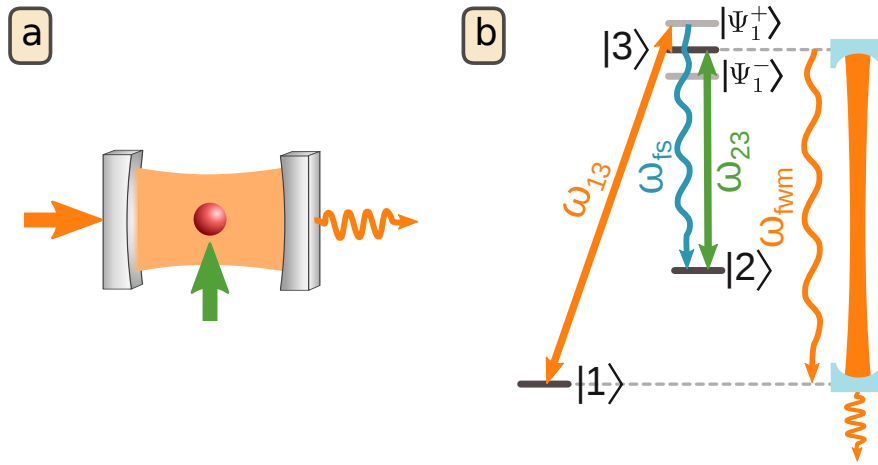
Figure 4.1: (a) shows a sketch of the setup with the driving geometry. (b) shows the level scheme in the atomic basis.

A sketch of the driving geometry is in shown in Figure 4.1(a) and the atomic level scheme is shown in Figure 4.1(b). The CEIT system consists of a three level atom, one transverse laser beam with frequency ω_{23} coupling the states $|2\rangle$ and $|3\rangle$ and a cavity that is strongly coupled to the transition $|1\rangle \leftrightarrow |3\rangle$ with coupling constant g. This is the same system as already introduced in Section 2.2. Neither the transverse laser nor the cavity exhibit a detuning to their respective atomic transition. This system is driven by an additional cavity driving probe laser with frequency ω_{13} that exhibits a detuning of $\Delta_p = \omega_c - \omega_{13}$ to the cavity frequency ω_c. As long as this additional laser drive is weak in comparison to the other fields in the system, it can be seen as a perturbation, that does not change the energy structure with the already introduced triplet structure for a specific excitation number. This is the case in the experiments in this chapter. Therefore the additional laser beam merely probes the existing energy landscape of the CEIT system and drives transitions to different manifolds of excitation. The concrete implementation in the ^{87}Rb atom uses

the two ground states $|1\rangle = |5S_{1/2}, F = 1, m_F = 1\rangle$ and $|2\rangle = |5S_{1/2}, F = 2, m_F = 2\rangle$ and the excited state $|3\rangle = |5P_{3/2}, F'' = 2, m_{F''} = 2\rangle$. The coupling constant and cavity field decay rate are $(\kappa, g)/2\pi = (1.5, 10.2)\,\text{MHz}$. When the frequency of the probing beam is scanned, it maps the energy landscape and the output field of the cavity shows the spectrum in Figure 4.2. The spectrum shows three distinct peaks. The center peak stems
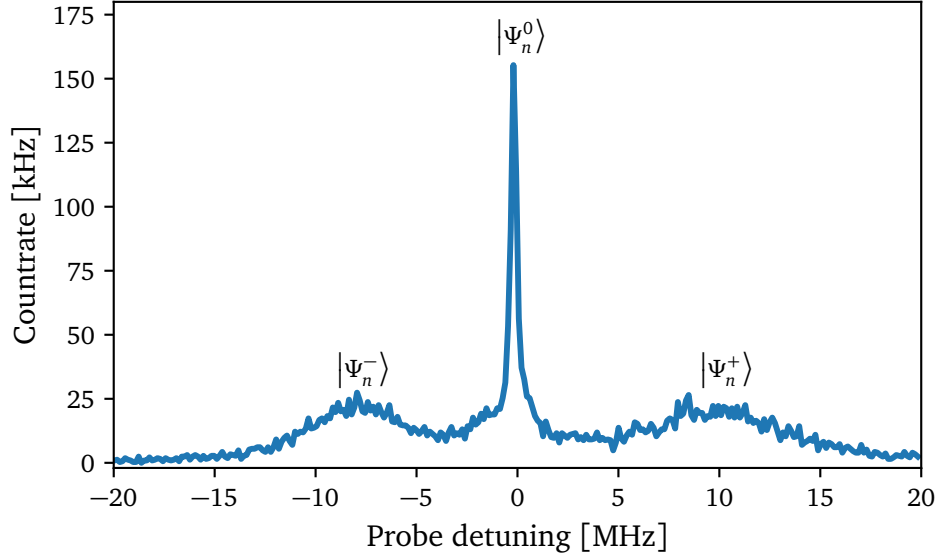
Figure 4.2: Shown is the photon detection rate of the cavity output field against the frequency detuning Δ_p of the probing field. The origin of each peak is denoted above and explained in the text.

from the actual EIT, and is very narrow. It is narrow because the dark states in cavity EIT do not have a contribution of the excited atomic state, which would introduce a fast decay. This can be seen very clearly in the ladder picture as introduced in Section 2.2. In this picture the coherent probing field leads to transitions in the dark states of the ladder $|\Psi_n^0\rangle$. Because the energy-splitting between each rung in the manifold is constant, all higher dark states are potentially addressed, limited by the driving strength of the probing field. There are two additional features at a frequency of around $\pm E_1^{\pm}/\hbar$, that stem from n-photon transitions to bright states in CEIT $\left(|\Psi_n^{\pm}\rangle\right)$. The ladder of bright states is nonlinear, meaning the probing laser is only resonant to one specific transition at a time. Nevertheless, the spectrum is mainly governed by transitions to the first manifold, because the excitation probability decreases for higher rungs, as the weak driving field contains only negligible higher photon components. This effect can be also observed in the photon correlation function $g^{(2)}(\tau)$. Driving the system around the transition frequency to the first bright state $|\Psi_1^+\rangle$, at 9.5 MHz blue detuned from the $|1\rangle \leftrightarrow |3\rangle$ transition frequency $(\Delta_p/2\pi = 9.5\,\text{MHz})$, leads to the photon correlation function in Figure 4.3(b).

The resulting correlation function shows slightly sub-Poissonian photon statistics at $\tau = 0$, which indicates that mainly the first manifold, with only one excitation in the system, is addressed by the probing laser field. Very pronounced is a long lasting oscillation with a
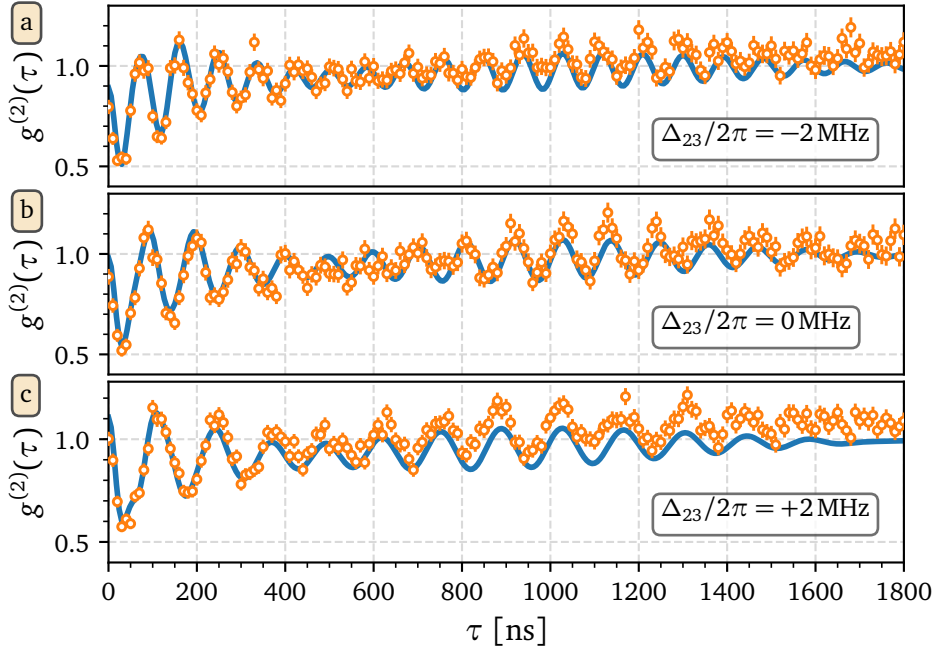
Figure 4.3: Photon correlation function for different parameters. (a) shows correlations for $\Delta_{23}/2\pi = -2\,\mathrm{MHz}$ and (c) for $\Delta_{23}/2\pi = 2\,\mathrm{MHz}$ in comparison to no detuning in (b). The beat frequencies are $\approx 11.5\,\mathrm{MHz}$ and $\approx 10.7\,\mathrm{MHz}$ in (a) and $\approx 7.5\,\mathrm{MHz}$ and $\approx 6.7\,\mathrm{MHz}$ in (c). Blue in the background is a quantum theory of the full relevant level scheme without any fit parameters.

frequency of about 9.5 MHz. The coherence time for which the oscillation is visible is on the order of 2 μs.

The oscillation occurs due to a beat between the drive field in the cavity with frequency ω_{13} and a newly generated field inside the cavity with ω_{fwm}. The generation of this new field can be explained in terms of a cycling process in the energy level scheme. To keep it concise, the following description only considers the first manifold of the CEIT system but can be generalized straightforwardly for higher rungs (which only need to be considered for higher driving strengths). For reference it is useful to compare the description with the level scheme in Figure 4.1. Initially the system is prepared in state $|1,0\rangle$, with |atomic state, cavity photons⟩. The probing beam with frequency ω_{13} drives the transition to state $|\Psi_1^+\rangle$ resonantly. This eigenstate has components of $|1,1\rangle$,$|2,0\rangle$ and $|3,0\rangle$, but can only build up incompletely as there is no coherent evolution to the atomic state $|2\rangle$ under the applied drives. As a result, a superposition state between the initial state, the state with one cavity photon $|1,1\rangle$ and the excited atomic state $|3,0\rangle$ forms. From there the system has the option to decay via the atomic excited state component $|3,0\rangle$ (a decay from $|1,1\rangle$ via the cavity is also possible but does not proceed in the cycle) to both atomic ground states $|1,0\rangle$ and $|2,0\rangle$. A decay to $|1,0\rangle$ does not continue the cycle as it is the initial state again. Only a decay into $|2,0\rangle$, which is accompanied by emission of a photon of frequency ω_{fs} into free space, allows for a continuation of the cycle. $|2,0\rangle$ is not an eigenstate of the system and therefore evolves into the dark

state $|\Psi_1^0\rangle$, under influence of the driving laser with frequency ω_{23}. This dark state has only components of atomic ground states $|1,1\rangle$ and $|2,0\rangle$ and therefore can solely decay via its cavity field component. For typical parameters the photonic component is small, as shown in Section 2.2. Therefore, the dark state is long lived but eventually decays spontaneously via the cavity back into the initial state $|1,0\rangle$ while emitting a photon with frequency ω_{fwm} out of the cavity. This closes the cycle, during which two new light fields are generated. The first one via the decay of state $|3,0\rangle$, which is emitted into free space due to being a purely atomic decay. This free space photon could not be measured in the experiment. The second field is generated by decay of the dark state $|\Psi_1^0\rangle$ to atomic state $|1,0\rangle$ via the cavity. This field with ω_{fwm} interferes with the drive field leaking from the cavity with frequency ω_{13} and manifests itself in the beat observed in the correlation functions.
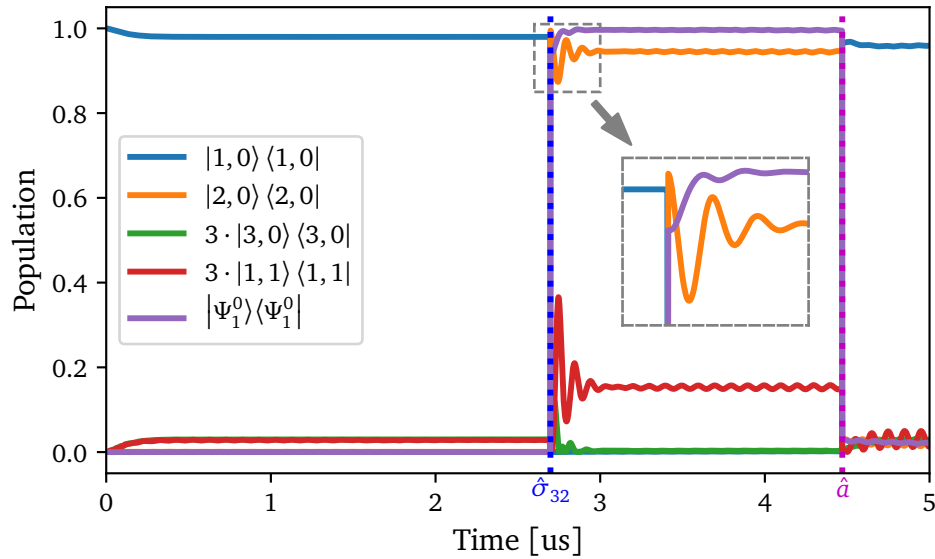

Figure 4.4: Population of different states in a single Monte-Carlo simulation trace over time for realistic parameters, showing the cycle that the atom undergoes. The dotted vertical lines denote quantum jumps stemming from the operators indicated below in corresponding color. The relevant simulation parameters are: $g/2\pi = 10\,\mathrm{MHz}, \Omega_{23}/2\pi = 2.4\,\mathrm{MHz}, \Delta_p/2\pi = 10\,\mathrm{MHz}$.

A Monte-Carlo simulation of the system with close-to-experiment parameters in Figure 4.4 validates this view. It especially shows, that there is no coherent evolution from state $|1,0\rangle$ to $|2,0\rangle$ without a spontaneous atomic decay, as happens at around 2.7 µs. Only after that point, almost 100% of the population is in state $|2,0\rangle$, which allows to continue the cycle via evolution into the dark state $|\Psi_1^0\rangle$ (which becomes clear in the magnified inset). Subsequently, the cavity decays at 4.5 µs into the state $|1,0\rangle$, after which the cycle restarts. The small deviations from that behavior, which are mainly visible in the simulation after the first cycle, are due to population of higher excitation rungs.

Another evidence of this cycling view, and especially the origin of the new light field of frequency ω_{fwm}, is provided by the coherence time of the generated field. It was
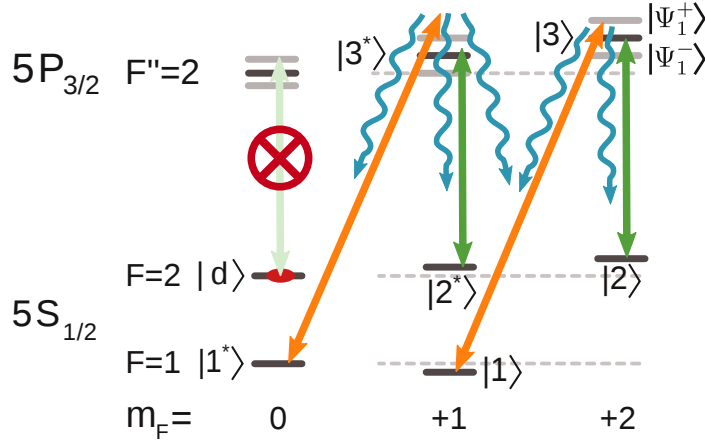
Figure 4.5: The relevant part of the level scheme including decays and both Λ-systems that play a role in the generation of the new light field within the cavity.

already mentioned that this is on the order of $2\,\mu s$. This agrees very well with the lifetime of the dark state $|\Psi_1^0\rangle$ (which is derived in Section A.3), indicating that this is indeed the source of the new field. Additionally, further experiments later presented in this section reveal that the coherence time is also tunable by Ω_{23} (Figure 4.7), exactly as expected from a field stemming from the decay of the dark state. The cycle is not closed in a fully coherent way, as it still relies on a spontaneous atomic decay into free space. This can be seen especially in comparison to the experiments in the next section of the thesis (Section 5), where the free space decay is essentially replaced by a coherent driving field, which leads to the generation of a spectrally substantially narrower field.

A more detailed look into the frequency of the newly generated field reveals that it fulfills an energy conservation condition that is typical for four-wave mixing schemes:

$$\omega_{\text{fwm}} = \omega_{13} + \omega_{23} - \omega_{\text{fs}} \tag{4.1}$$

Figure 4.3 show the correlation function for the same detuning in the probe beam ($\Delta_p/2\pi = 9.5\,\text{MHz}$) but for different values of the detuning of the $|2\rangle \leftrightarrow |3\rangle$ beam. As is clearly visible, the frequency of the beat changes according to the four-wave mixing condition. The system is modeled via a full quantum simulation incorporating all relevant atomic levels and the magnetic field in the experiment. The simulation results agree well with the experimental data, as can be seen by the agreement of the blue curve with the data in Figure 4.3. Note that this is not a fit, but is the direct simulation with experimentally determined parameters from independent measurements. Close examination of Figure 4.3(b) reveals that the observed beat actually has two frequency components at $\approx 9.5\,\text{MHz}$ and at $\approx 8.7\,\text{MHz}$, respectively. This can be explained by a depumping mechanism that is depicted in Figure 4.5. Initially the system is well prepared in ground state $|1\rangle$, but after excitation to state $|\Psi_1^+\rangle$ the system can also decay into the state $|2^*\rangle = |5S_{1/2}, F = 2, m_F = 1\rangle$. This forms a new Λ-system with states $|1^*\rangle = |5S_{1/2}, F = 1, m_F = 0\rangle$ and $|3^*\rangle = |5P_{3/2}, F'' = 2, m_{F''} = 1\rangle$. From this system it can

decay even further, which ultimately leads to accumulation of the atomic population in the dark state $|d\rangle = |5S_{1/2}, F = 2, m_F = 0\rangle$. There is no escape channel from that state, because the transition to $|5P_{3/2}, F'' = 2, m_{F''} = 0\rangle$ is dipole forbidden. Therefore, all detected photons are from either the original Λ-system or from the Λ^*-system. The frequency of the beat, that is visible in the $g^{(2)}$ correlation function, is given by:

$$\omega_{\text{beat}} = \omega_{\text{fwm}} - \omega_{13} \tag{4.2}$$

Due to energy conservation, the frequency of the free space field is given by:

$$\omega_{\text{fs}} = \omega_{13} - (\omega_{t1\Psi_1^+} - \omega_{t2\Psi_1^+}) \tag{4.3}$$

where $\omega_{t1\Psi_1^+}$ is the transition frequency of the $|1\rangle \leftrightarrow |\Psi_1^+\rangle$ transition and $\omega_{t2\Psi_1^+}$ the transition frequency of the $|2\rangle \leftrightarrow |\Psi_1^+\rangle$ transition. Inserting this into the four-wave mixing condition from Equation 4.1, the frequency of the field generated in the cavity becomes:

$$\omega_{\text{fwm}} = \omega_{23} + \omega_{t1\Psi_1^+} - \omega_{t2\Psi_1^+} \tag{4.4}$$

The energy difference between the two ground states $|1\rangle$ and $|2\rangle$ is given by:

$$\omega_{t1\Psi_1^+} - \omega_{t2\Psi_1^+} = \omega_{t13} - \omega_{t23} \tag{4.5}$$

where $\omega_{t13}(\omega_{t23})$ is the atomic transition frequency of the $|1\rangle \leftrightarrow |3\rangle (|2\rangle \leftrightarrow |3\rangle)$ transition. Inserting the relation leads to:

$$\omega_{\text{fwm}} = \omega_{23} + \omega_{t13} - \omega_{t23} \tag{4.6}$$

This results in a beat frequency of:

$$\omega_{\text{beat}} = \omega_{23} + \omega_{t13} - \omega_{t23} - \omega_{13} \tag{4.7}$$

This means the observed beat in the correlation function depends on the atomic transition frequencies ω_{t13} and ω_{t23}. These transition frequencies are different when the system depumps into the other lambda system $\Lambda^* \equiv |1^*\rangle \leftrightarrow |2^*\rangle \leftrightarrow |3^*\rangle$ because the applied magnetic guiding field lifts the degeneracy between different Zeeman substates. This explains the occurrence of two components in the beat. The applied magnetic guiding field of $0.6\,\text{G}$ results in a frequency difference of the two generated beats of $0.84\,\text{MHz}$, which is in very good agreement with the experimentally measured value of $0.8\,\text{MHz}$. These two frequency components are especially well visible in a Fourier transform of the correlation function, which can be seen in Figure 4.6 in blue (for a different detuning between ω_{13} and ω_{23}). This Fourier transform clearly validates the occurrence of two main frequency components, which stem from depumping as already explained before. The right peak belongs to the initial Λ-system, whereas the left peak can be attributed to the Λ^*-system. The height of the peaks is almost identical, which is due to the fact that this measurement had a measurement duration of $53\,\mu\text{s}$. For the applied driving
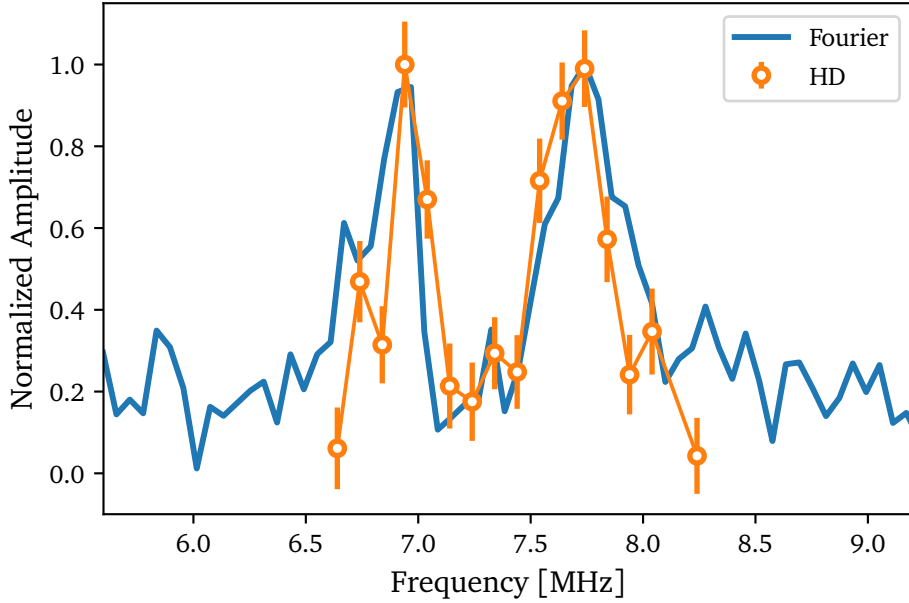
Figure 4.6: Shown in blue is the Fourier transform of the $g^{(2)}(\tau)$ correlation function over frequency. Shown in orange is the heterodyne measurement of the field amplitude over the frequency detuning of the local oscillator beam. This mode of operation is described in Section 3.5. The connecting line is a guide to the eye. The heterodyne spectrum is shifted in frequency as such that the highest values overlap. Both curves are normalized.

strengths, the system is already advanced in the depumping process at that time and the amount of photons detected from both Λ-systems is equal. The widths of the peaks, which differ due to different coherence times in the respective CEIT subsystems, is a result of the different Clebsch-Gordon coefficients of the transitions in the Λ- and Λ^*- systems. The effective driving strength varies from $\Omega_{23}/2\pi = 5.7\,\text{MHz}$ to $\Omega_{2^*3^*}/2\pi = 2.9\,\text{MHz}$.

So far the generated light field was only investigated by the beat with the probing field in a photon correlation measurement. Another, and in certain ways, more direct, approach is to use the heterodyne setup introduced in Section 3.5 as a spectrum analyzer and measure the output light field in an amplitude measurement of its electric field. The measurement is shown in Figure 4.6 in orange. The heterodyne measurement clearly shows two peaks with the expected frequency difference from each other. Also the expected relative height of both peaks agree well with the Fourier spectrum.

It was already observed in the widths of the peaks, that the Rabi frequency Ω_{23} plays a central role for the coherence time (coherence time is inversely proportional to peak width). Figure 4.7 shows the correlation function for different values of Ω_{23}, with the beating becoming shorter for higher Ω_{23}. This is because the Rabi frequency Ω_{23} determines the lifetime of the first dark state $|\Psi_1^0\rangle$ of the CEIT system. This is due to the fact, that the generated light is stemming from a decay of that long-lived state. For $\Omega_{23}/2\pi = 9.7\,\text{MHz}$ the time during which a beat is visible is reduced to about $100\,\text{ns}$. Aside from the change in the coherence time, the equal-time photon statistics of the cavity output also change
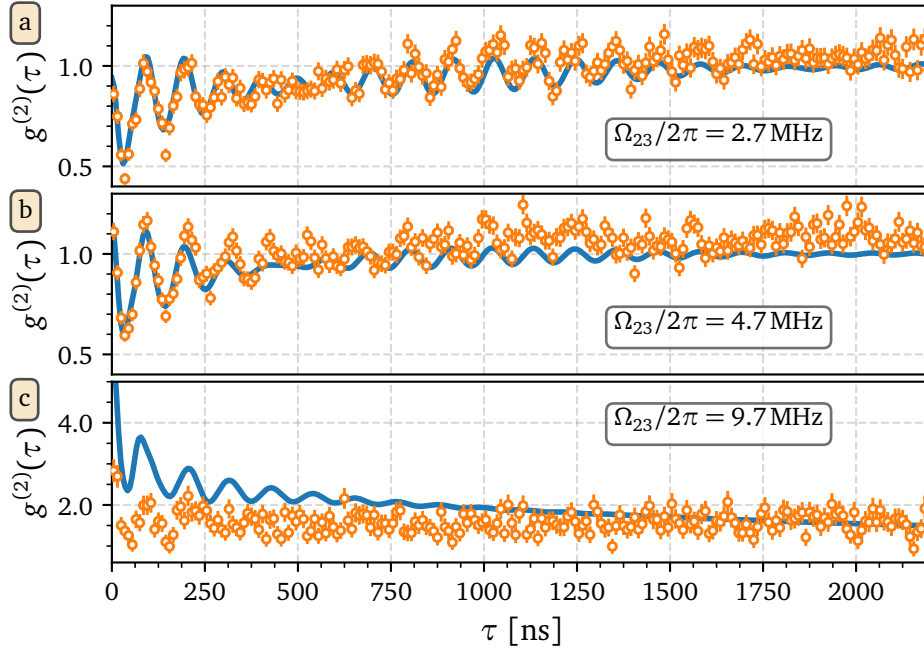
Figure 4.7: Photon correlation function for different Ω_{23} as indicated in each plot. The beat frequencies are $\approx 9.5\,\text{MHz}$ and $\approx 8.7\,\text{MHz}$. In the background in blue is a full quantum simulation of the system.

for increased Ω_{23}. It goes from sub-Poissonian in 4.7(a) to strongly super-Poissonian in 4.7(c). When Ω_{23} is increased, the energy of the bright states in the state ladder changes, as it follows $E_n = \sqrt{ng^2 + \Omega_{23}^2}$ (as introduced in Section 2.2). Keeping Δ_p the same while increasing Ω_{23} tunes the dark state ladder for a fixed driving frequency in and out of resonance to bright states of different rungs. This alters the photon statistics, because the laser addresses different manifolds of the CEIT energy ladder in multi-photon transitions, depending on Ω_{23}. The effect was predicted in [41] and first measurements were presented in [46]. The effect allows for all-optical tuning of the photon statistics of the output light field via the power of the classical beam that drives the atom. This process does not change the wave-mixing and the frequency of the generated field stays the same.

4.3. Summary

This section discussed a wave-mixing process with extremely low light levels in a three level atom. The resultant newly generated field reveals itself in a strong oscillation of the $g^{(2)}(\tau)$ photon correlation function of the output light field from the cavity. The generated field stems from an incoherently closed cycle in the atomic level scheme, that generates one cavity and one free space photon per cycle. The frequency of the new field can be tuned via the frequency of the light field that drives the atom. The generated field furthermore shows a high coherence to the input fields, as revealed by the long

coherence time of the beat in the correlation function. This is further confirmed by a direct measurement of its spectral properties via a heterodyne detection. Furthermore, by tuning the power of the classical laser driving the atom, the equal-time photon statistics of the system can be tuned all optically from sub- to super-Poissonian.

5. Closed cycle and climbing the dark state ladder

5.1. Introduction

The system from the former chapter is modified by adding another field that couples the two ground states and therefore closes the system coherently. As the system does not have additional degrees of freedom, it is fully coherent and shows no source of decoherence from atomic decay. This gives rise to the somehow expected effect of optical wave mixing, as is typical when several waves interact with a nonlinear atomic system [71–75], but here in the unique setting of a parametric but resonant process. Usually an atom, that is irradiated by a light field, which is resonant to a transition between a ground and excited state is seen as undergoing repeated absorption and subsequent emission of photons, which is accompanied by quantum jumps between different electronic states [76]. The theory and the experiments in this chapter however change the paradigm of this view by showing a continuous generation of a light field by an atom without atomic excitation. The weak ground state coupling laser does not destroy the fragile dark state ladder in cavity EIT, which was already introduced in Section 2.2, but quite the contrary effect happens. The ground state coupling field allows to drive transitions between different manifolds in this harmonic ladder. Because the dark states are entangled states between the atomic ground states (no excited state component) and a certain cavity photon number, their decay leads to photon production in the cavity without atomic excitation. An investigation of the effective driving strengths and decay rates in the dark state ladder reveals, that for weak ground state driving, the ladder exhibits a Zeno effect [77]. This suppresses transitions to higher rungs, effectively blocking the ladder and leading to single photon emission. Stronger driving then lifts the blockade and produces a coherent field. In this chapter this new system and its novel effects are investigated theoretically and experimentally.

5.2. Theory

The contents of this chapter have partially been published in:

> *Continuous generation of quantum light from a single*
> *ground-state atom in an optical cavity*
> C. J. Villas-Boas, K. N. Tolazzi, B. Wang, C. Ianzano, G. Rempe
> arXiv 1906.11449 (quant-ph), accepted in Physical Review Letters

The level scheme of the system that is considered is shown in Figure 5.1(a) and is very similar to the scheme presented in Section 2.2, but with an additional laser beam. This beam connects the atomic ground states $|1\rangle$ and $|2\rangle$ and has a frequency of $\omega_{l,12}$ and a Rabi frequency of Ω_{12}. State $|2\rangle$ is coupled to the excited state $|3\rangle$ via a laser field with frequency $\omega_{l,23}$ and Rabi frequency Ω_{23}. This excited state is coupled to ground state $|1\rangle$ via a resonant cavity mode with coupling constant g. In the following chapter, this cavity mode is not driven but the output field that leaks out of the cavity is measured.
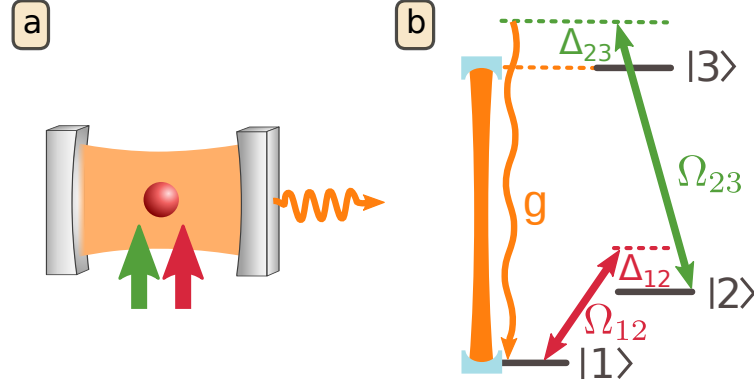
Figure 5.1: (a) shows the driving field configuration. (b) shows the level scheme in the bare atomic basis with the ground states $|1\rangle,|2\rangle$ and the excited state $|3\rangle$. Also shown are the Rabi frequencies $\Omega_{12,23}$ and detunings $\Delta_{12,23}$ of the driving fields and the atom cavity coupling constant g.

The two actively driven fields exhibit detunings between field and atomic transition of $\Delta_{12} = \omega_{a,12} - \omega_{l,12}$ and $\Delta_{23} = \omega_{a,23} - \omega_{l,32}$ with $\omega_{a,kl}$ being the respective atomic transition frequency. The Hamiltonian of the system is very similar to the one given in Section 2.2 and can be written in rotating wave approximation as:

$$H = \Delta_{12}\hat{\sigma}_{22} + (\Delta_{12} + \Delta_{23})\hat{\sigma}_{33} + (\Delta_{12} + \Delta_{23})\hat{a}^\dagger\hat{a} + g\hat{a}\hat{\sigma}_{31} + \Omega_{12}\hat{\sigma}_{21} + \Omega_{23}\hat{\sigma}_{32} + \text{h.c.}$$

(5.1)

where $\hat{\sigma}_{kl}$ denote the atomic transition operators of the form $\hat{\sigma}_{kl} = |k\rangle\langle l|$ $(k, l = 1, 2, 3)$ and $\hat{a}$ $(\hat{a}^\dagger)$ is the annihilation (creation) operator of the quantized cavity field. As the system exhibits dissipation to the environment, it is an open quantum system and it is possible to calculate ensemble averages with the density matrix formalism as described in Section 2.4. Within this chapter for all theoretical results $\kappa = 1$ applies and all other parameters are expressed in terms of κ. To deepen the understanding of the system it is helpful to view the system in two different regimes.

5.2.1. Weak ground state coupling

The regime where $\Omega_{12} \ll g$ is called weak ground state coupling regime. This means the coupling field between the ground states can be treated as a perturbation V and the eigenstates and eigenenergies of the system are the same as in the theoretical treatment in Section 2.2.

The system is now investigated by scanning the detunings of the driving fields. Figure 5.2 shows a two dimensional color plot where both detunings are scanned. The different colors correspond to the logarithmic steady state population of different observables. It can be clearly seen, that the cavity is populated with photons although it is not directly driven. Furthermore, this scan reveals the complex energy structure of the first energy manifold of this system. Emission stems primarily from the first manifold as the driving strength Ω_{12} was low in this simulation, thus higher manifolds are barely populated as later presented
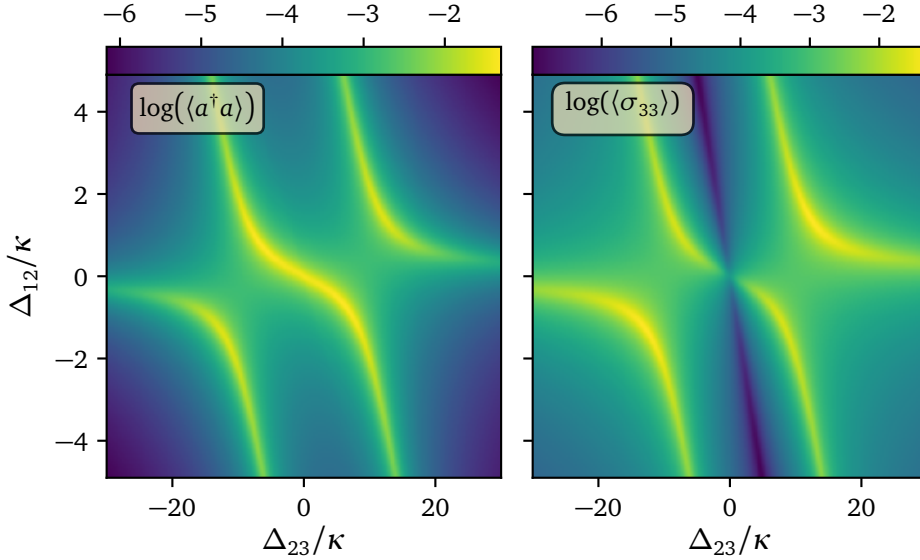
Figure 5.2: Steady state values of different observables in two dimensional scans of Δ_{12} against Δ_{23}. The left plot shows the logarithmic population of the cavity mode, the right plot shows the logarithmic population of the atomic excited state $|3\rangle$.

results will reveal. There are three distinct lines of high population visible in the left plot where the photon production rate is significant. These correspond to the three states in the first manifold of CEIT, where each exhibits a cavity component and therefore a non-vanishing population in the cavity. The right plot with the atomic population shows almost the same behavior, but in addition a dark line appears at $\Delta_{12} + \Delta_{23} = 0$ where the two photon detuning is zero and therefore the dark state of the first manifold is resonantly driven. Of special interest is the point at $\Delta_{12} = \Delta_{23} = 0$, because the cavity population has a maximum while the atomic population in the excited state remains low. Thus even though all atomic transitions are driven perfectly on resonance, the excitation of the atom remains low and the excitation of the cavity is high. On first glance this seems contradictory.

To explain this, it is convenient to reformulate the system (for $\Delta_{12} = \Delta_{23} = 0$) in the $\{|+\rangle, |-\rangle\}$ basis with $|\pm\rangle = 1/\sqrt{2}(|1\rangle \pm |2\rangle)$. In this basis the effective energy level diagram and the driving strengths look like in Figure 5.3. This can be understood as two independent Λ-system for which an interference effect is expected, as known from cavity EIT [36]. For weak ground state coupling the transitions $|+\rangle \leftrightarrow |3\rangle$ and $|-\rangle \leftrightarrow |3\rangle$ are both almost resonant and the interference between these two absorption paths avoids the excitation of the atom to $|3\rangle$ and the system remains in the subspace of dark states. For further investigation it is helpful to derive an effective Hamiltonian for that situation as is explicitly done in the appendix under Section A.1. The final driven Hamiltonian for
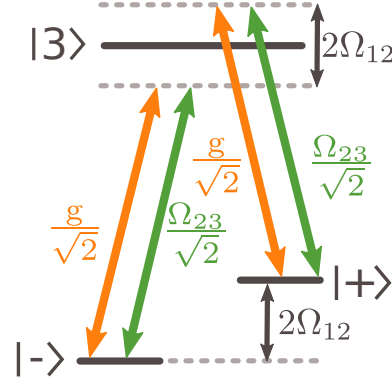
Figure 5.3: The effective level scheme and driving strengths for vanishing detunings of the driving fields $\Delta_{12,23} = 0$ in the $|+\rangle, |-\rangle$ basis.

$\Omega_{23} \ll g$ is:

$$V_{eff} \simeq -\Omega_{12} \left|\Psi_1^0\right\rangle\left\langle\Psi_0^0\right| - \Omega_{12} \sum_{n=1}^{\infty} \frac{\Omega_{23}}{g\sqrt{n}} \left|\Psi_{n+1}^0\right\rangle\left\langle\Psi_n^0\right| + \text{h.c.} \tag{5.2}$$

This Hamiltonian promotes transitions between all dark states ($n \leftrightarrow n+1$) at the same time. As the dark state ladder is linear all transitions are resonant to the same driving fields. Remarkably, this system stays solely in the subspace of dark states, in driving as well as in decay, because there is no decay from a dark state to a bright state as is shown in Section A.3. This behavior is visualized in Figure 5.4. As the dark states have a photonic component in the cavity, it is possible to continuously generate photons without exciting the atom.
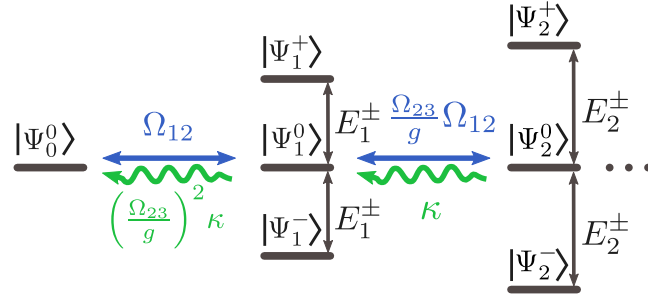
Figure 5.4: The dark state ladder of the system for the first three dark states, with effective driving strengths in blue and decay rates in green. The factors are an approximation for $(\Omega_{12}, \Omega_{23}) \ll g$.

5.2.2. Quantum Zeno effect

It is insightful to compare the effective driving strengths of different transitions in the dark state ladder. To simplify the expression, the discussion in this subsection is in the

limit $\Omega_{23} \ll g$. The full expressions can be found in Appendix Appendix A. The effective driving strength from $n-1$ to n is given by:

$$D(n) = \begin{cases} \Omega_{12} & n = 1 \\ \Omega_{12}\Omega_{23}/\left(g\sqrt{n-1}\right) & n > 1 \end{cases} \tag{5.3}$$

which shows a steep decrease in the driving strength from $n = 1$ to $n > 1$. Considering the decay rates of different dark states, which can be calculated by Fermi's golden rule (derivation in Section A.3), leads to:

$$\Gamma_{\Psi_n^0 \to \Psi_{n-1}^0} = \Gamma(n) = \begin{cases} \frac{\Omega_{23}^2}{g^2}\kappa & n = 1 \\ (n-1)\kappa & n > 1 \end{cases} \tag{5.4}$$

This shows a fast increase from $n = 1$ to $n > 1$ in the decay rate. So there is a step from $n = 1$ to $n > 1$ for both the effective driving which decreases and the decay rate which increases. A comparison between the driving strength to the n'th dark state and its decay leads to the definition of a Zeno-factor as: $Z(n) = D(n)/\Gamma(n)$. This measure is called Zeno factor because the decay from higher states $n > 1$ is much faster than the effective driving strength to these states, so the system is constantly projected into the subspace of the first two dark states $|\Psi_1^0\rangle$ and $|\Psi_0^0\rangle$ and experiences a continuous quantum Zeno effect [77].
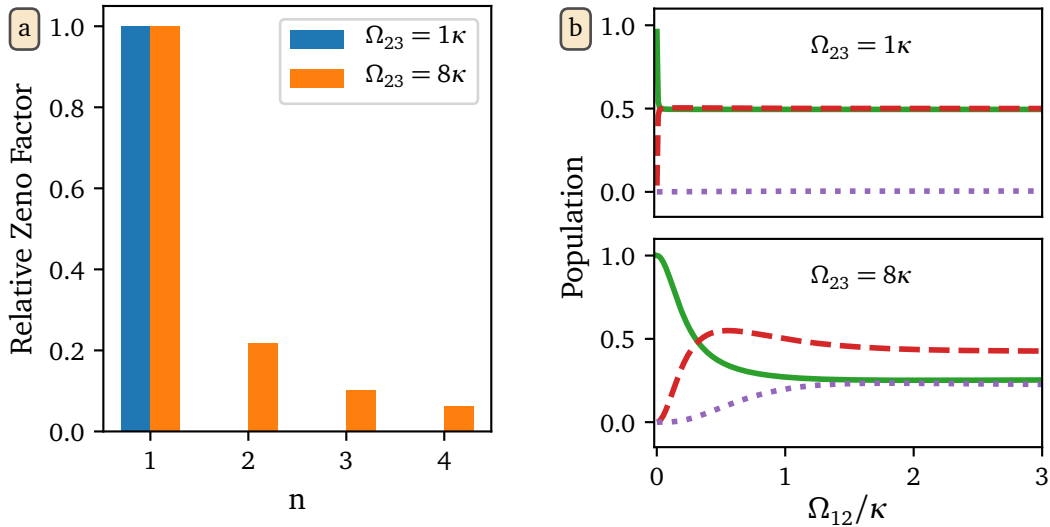
Figure 5.5: (a) shows the relative Zeno factor $\mathscr{Z}(n)$ for different n and for two different values of Ω_{23}. The blue bars for higher $n > 1$ are so small that they are not visible in the picture. (b) shows the population of the first three dark states over Ω_{12} for two different values of Ω_{23}. The colors correspond to: green solid$\to \Psi_0^0$, red dashed$\to \Psi_1^0$, purple dotted$\to \Psi_2^0$.

To compare the different dark state Zeno factors, it is helpful to normalize this measure to $Z(1)$ and define the relative Zeno-factor as $\mathscr{Z}(n) = Z(n)/Z(1)$. This measure is helpful in

determining how close the system behaves to a two level system. The calculated relative Zeno factors for different values of n and Ω_{23} are shown in Figure 5.5(a). The blue bars are calculated for $\Omega_{23} = 1\kappa$ and are so small for $n > 1$ that they are not visible. The relative Zeno factor is already $1 \cdot 10^{-3}$ for $n = 2$. This leaves the system an almost perfect two level system with transitions between the first two dark states with $n = 0$ and $n = 1$. The Zeno factor can be tuned by changing Ω_{23}. For $\Omega_{23} = 8\kappa$ the relative Zeno factor is 0.22 for $n = 2$ and therefore 220 times bigger than in the $\Omega_{23} = 1\kappa$ case. Another illustration of this effect is Figure 5.5(b), which shows the change in the population of the first three dark states for increasing Ω_{12} for two different values of Ω_{23}. In the case of $\Omega_{23} = 1\kappa$, the system behaves as a perfect two level system, between the ground state and the first dark state, as already expected from the Zeno-factor. Higher states are not populated. This two level behavior breaks down for higher values of Ω_{23} (e.g. $\Omega_{23} = 8\kappa$) and higher states also have significant population (see Figure 5.5(b)). The almost perfect two level behavior for low Ω_{23} can also be seen in Figure 5.6. Shown in that figure, is the
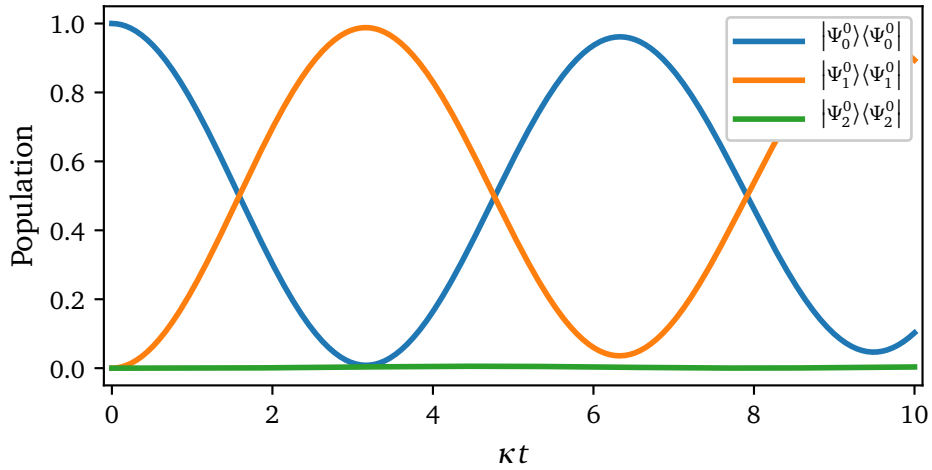
Figure 5.6: Population of the dark states and the cavity over time exhibiting Rabi oscillations between the the two dark states. The simulation parameters are $\Omega_{12} = 0.5\kappa, \Omega_{23} = 1.0\kappa, g = 10\kappa$.

population oscillation between the ground state and first dark state over time, for a fixed driving strength. The dark state population shows typical Rabi oscillations between the first two dark states as in a two level atom with decay. In contrast to a typical atom the decay here is not given by Γ_{33} or κ but by $\Gamma(1) = \kappa\Omega_{23}^2/g^2$, which is much lower than the usual decay constants in an purely atomic two-level system.

As already mentioned the Zeno-blockade behavior can be controlled by Ω_{23}. Higher values unblock formerly blocked parts of the dark state ladder. A way to investigate this blockade is by the equal-time correlation $g^2(0)$ value, because an emission of more than one photon at the same time is only possible when higher states of the dark state ladder are populated. The result of a simulation is shown in Figure 5.7(a). As can be seen in this plot, the equal-time correlation approaches one for higher values of Ω_{23}, while the cavity population goes down. This is expected from the full analytical formula of the effective
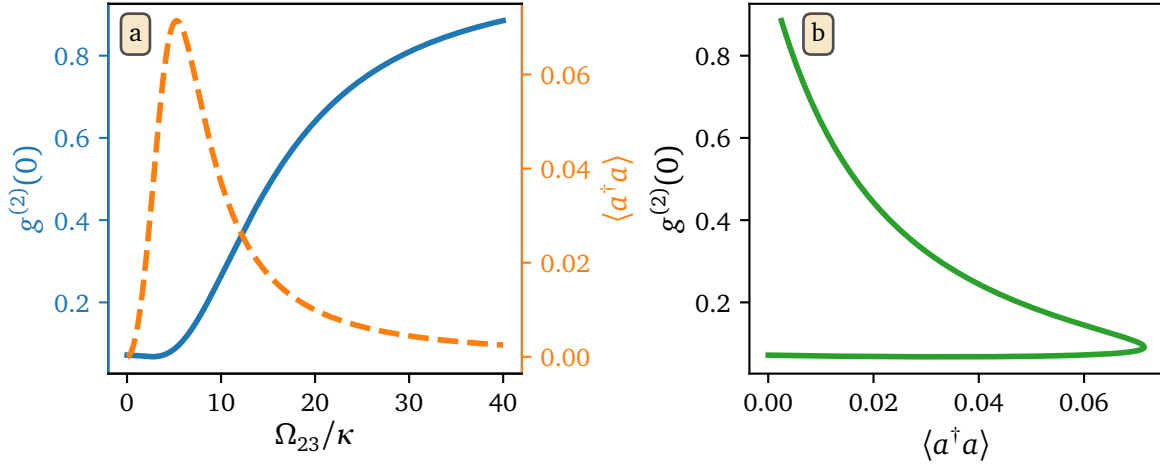
Figure 5.7: (a) shows the population in the cavity (orange dashed) and the equal-time photon correlation (blue) against the driving strength Ω_{23}. (b) shows the same data as graph (a) but in a plot where the $g^{(2)}(0)$ is plotted against the cavity population. The simulation parameters are $\Omega_{12} = 0.1\kappa$, $g = 10\kappa$.

driving in the ladder and is treated in Section A.1.

The change in photon statistics is because the Zeno-blockade is lifted and the ladder of dark states can be climbed for increased Ω_{23}, which leads to the generation of a light field that reflects the population of higher states by approaching a correlation value of one. This is not a mere filling of the cavity but a true lifting of the Zeno-blockade as can be seen in Figure 5.7(b), which shows, that the same cavity population leads to different values for the equal-time photon correlation depending on Ω_{23}.

5.2.3. Spectral properties of the generated light field

The power spectrum of a quantized light field can be determined via the Fourier-transform of the un-normalized first-order correlation function $G^{(1)}(\tau) = \left\langle a^\dagger(\tau)a(0)\right\rangle$ [78]:

$$S(\omega) = \int_{-\infty}^{+\infty} \left\langle a^\dagger(\tau)a(0)\right\rangle e^{-i\omega t}d\tau \tag{5.5}$$

Several simulated spectra of the cavity field for different parameters are shown in Figure 5.8. The driving fields were resonant for this simulation. There are several things that are remarkable in all the spectra: The emitted field exhibits a Dirac delta function-like behavior at zero detuning that has no measurable width. This peak emerges from another peak at zero detuning, but with a non-vanishing width. Furthermore each spectrum shows two additional peaks at roughly $\pm 2\Omega_{12}$. The width of these additional peaks depends on Ω_{23} and on the coupling constant g as can be seen from the spectra for different parameters. This structure can be explained as a Mollow triplet [78], in analogy to the spectrum of a two-level system, as the presented system can be viewed as such in certain
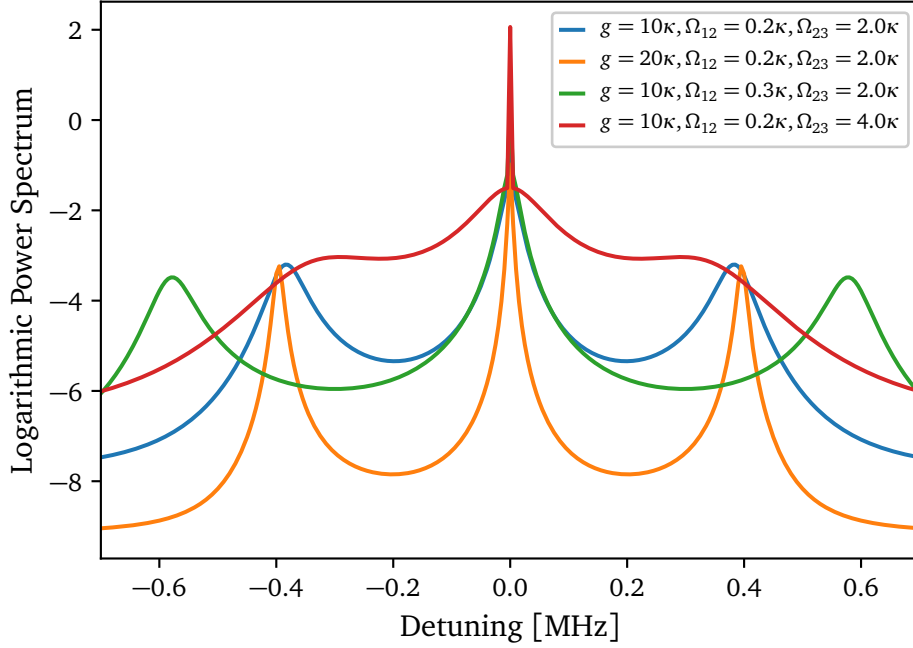
Figure 5.8: Logarithmic power spectra of the generated light field for different parameters. The shown spectra are for the zero-detuning case $\Delta_{12} = \Delta_{23} = 0$.

regimes (which has been shown in the previous sections). Mollow derived that the emission power spectrum of a driven two-level atom consists of a coherent part from elastic scattering, that exhibits the same spectral properties as the driving laser beam, namely a delta function in the ideal case (experimentally validated in [79]) and an incoherent part, that is emitted at different frequencies and is distributed in three peaks. In the Mollow theory, the position of the peaks is given by $0, \pm\Omega$, where Ω is the Rabi frequency of the drive. As already discussed the system in this chapter can be viewed (in the regime $\Omega_{23} \ll g$) as a two-level system due to the Zeno-blockade with the ground state $|\Psi_0^0\rangle$ and the excited state $|\Psi_1^0\rangle$. The effective Rabi frequency between these states is then $\Omega = 2\Omega_{12}$. This agrees very well with the positions of the peaks in the simulation. The width of the peaks is proportional to the spontaneous decay rate according to Mollow. The decay rate of the first dark state is given by $\kappa\Omega_{23}^2/g^2$ for $\Omega_{23} \ll g$. This is also confirmed by the simulation, as the peak width changes strongly with g and Ω_{23}. The height of the side peaks is convoluted with the cavity linewidth and therefore is getting smaller for higher effective Rabi-frequencies, because field-components outside of the cavity frequency window cannot build up. In summary, the spectrum behaves very much as expected for a two-level system with the two states $|\Psi_0^0\rangle$ and $|\Psi_1^0\rangle$, therefore supporting the results obtained in the previous chapters about the Zeno-blockade effect. Deviation from the two-level behavior is observed in the difference between the blue curve in Figure 5.8 and the red, where only Ω_{23} is varied. The side peaks move towards the inside, which is expected from the general expression (not for small Ω_{23}) for the Rabi-frequency (see Section A.1).

5.2.4. Strong ground state coupling

In the regime $\Omega_{12} \gg (g, \Omega_{23}) > \kappa$ it is clear from Figure 5.1(b) that the splitting between $|+\rangle$ and $|-\rangle$ is large. This splits the system into two independent two-level systems which are off-resonantly driven by the laser and cavity field. Even though the cavity mode and the laser field addressing $|2\rangle \leftrightarrow |3\rangle$ have a very distinct frequency, they couple the same transition in this regime. The effective Hamiltonian (derivation in the appendix under Section A.1) in this situation is given by:

$$
H_{eff} \simeq \frac{1}{2\Omega_{12}} \{ -\left[g^2 a^\dagger a + \Omega_{23}^2 + (g\Omega_{23} a + h.c.) \right] \sigma_{++}
$$
$$
+ \left[g^2 a^\dagger a + \Omega_{23}^2 - (g\Omega_{23} a + h.c.) \right] \sigma_{--} \}
$$

To gain further insights, it is interesting to view the situation in three different regimes:

Regime 1: $\kappa = 0$

Starting from the initial state $|1, 0\rangle = \frac{1}{\sqrt{2}} (|+\rangle + |-\rangle) |0\rangle$ the evolved state at time t will be (for a derivation see Section A.2):

$$
|\Psi(t)\rangle = \frac{1}{2} \left[|1\rangle \left(e^{i\theta t} |\alpha_+\rangle + e^{-i\theta t} |\alpha_-\rangle \right) + |2\rangle \left(e^{i\theta t} |\alpha_+\rangle - e^{-i\theta t} |\alpha_-\rangle \right) \right] \qquad (5.6)
$$

with $\theta = \frac{\Omega_{23}^2}{2\Omega_{12}}$ and $\alpha_\pm = \pm \frac{\Omega_{23}}{g} \left(e^{\mp i g^2 t / 2\Omega_{12}} - 1 \right)$. Performing an atomic ground state detection, projects the system into one of two Schrödinger cat states. Interesting to note is, that the phase and the amplitude of the coherent states in the cat state are both time dependent. So by choosing an appropriate time of projection, the properties of the cat state can be tuned. Figure 5.9 shows the Wigner-function [80] for different times t in the upper row, where it is clear that the cat state changes periodically over time. The lower plot shows the *size of the cat* ($\langle n \rangle = |\alpha|^2$) in blue and the phase θ in orange.

Regime 2: $g^2 \gg 2\Omega_{12}\kappa$

In this regime with a small cavity decay κ in comparison to g there will be a steady state which is a complete mixture between $|+\rangle$ and $|-\rangle$. Tracing over the atomic state leads to a steady state in the cavity field of [81]:

$$
\rho_{ss} = \frac{1}{2} (|\alpha_+\rangle\langle\alpha_+| + |\alpha_-\rangle\langle\alpha_-|) \qquad (5.7)
$$

with $\alpha_\pm = -i \frac{g\Omega_{23}}{\pm i g^2 - 2\Omega_{12}\kappa}$. For a small κ, like in this regime, this can be approximated as $\alpha_+ \simeq -\alpha_- \simeq -\Omega_{23}/g$. This is a mixture of two coherent states that are completely out of phase.
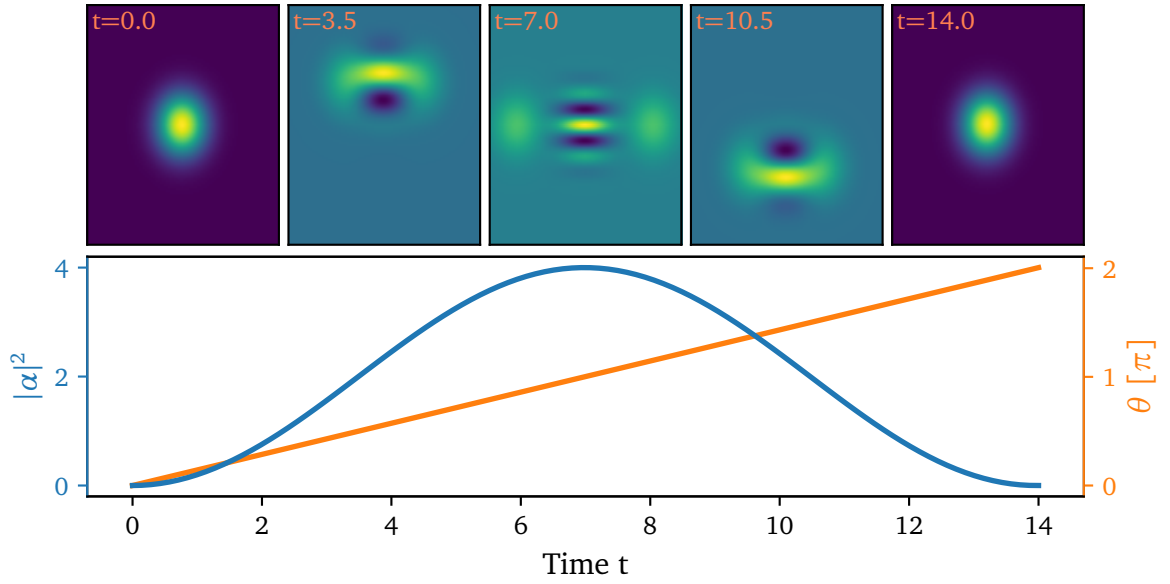
Figure 5.9: The upper row shows the Wigner function of the cavity field for different points in time. The lower plot shows the coherent state photon number $\langle n \rangle = |\alpha|^2$ (blue line, left axis) and the phase θ (orange line, right axis) over time.

Regime 3: $g^2 \ll 2\Omega_{12}\kappa$

In this regime α can be expressed as $\alpha \simeq \alpha_+ \simeq \alpha_- \simeq i\frac{g\Omega_{23}}{2\Omega_{12}\kappa}$. This simplifies Equation 5.7 to $\rho_{ss} = |\alpha\rangle\langle\alpha|$, which is a perfect coherent state in the cavity mode. These theoretical results concerning the field properties in the weak and strong ground state coupling regime and the transition between these two, can be seen clearly when evaluating the $g^2(0)$ value over Ω_{12}. Figure 5.10(a) shows this simulation, where the analytically predicted transition from single photon emission from a two-level system to a coherent state in the cavity for increased ground state coupling is clearly reflected in the $g^2(0)$ as it goes from a value of close to zero (single photon emission) to a value of one (coherent state) for higher ground state couplings. Figure 5.10(b) shows the $g^2(\tau)$ correlation function for one specific ground state coupling in each regime. The blue curve for low coupling, shows strong antibunching and an oscillation with the Rabi frequency between the ground state and the first dark state as expected for a two-level system. For long τ it settles to one. The orange curve for a high ground state coupling starts at one and shows minor residual oscillations for short timescales, stemming from transient internal dynamics, but shows no substantial deviation from a perfect coherent state.

5.2.5. Excitation-less generation of photons

As already mentioned, the emission of photons from the cavity stems from transitions between dark states, that do not have a component of the excited atomic state $|3\rangle$, but a photonic cavity component. A steady state photon number forms inside of the cavity, as
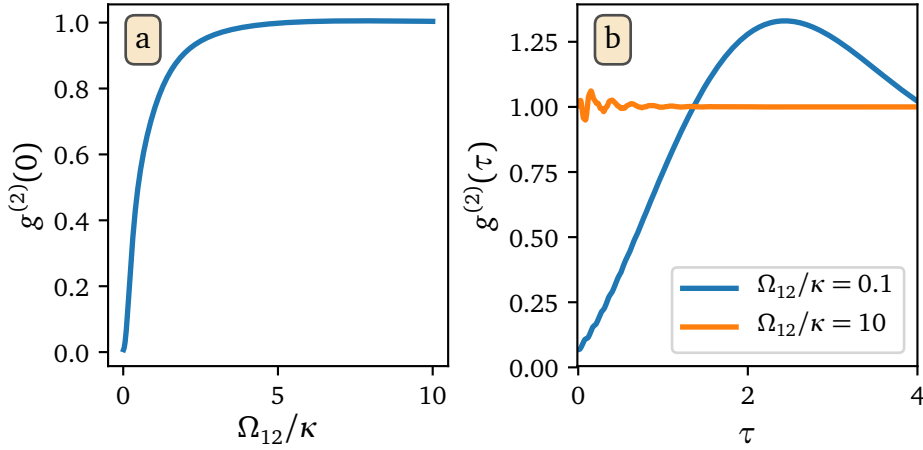
Figure 5.10: (a) shows the value of the two photon correlation function for time 0 against the ground state coupling strength. (b) shows the full correlation function for different ground state coupling strengths in different regimes. The other parameters are $\Omega_{23} = 3.0\kappa, g = 10\kappa$.

each dark state can decay via emission of a photon out of the cavity. The avoidance of state $|3\rangle$, despite resonant driving, is due to destructive interference of different absorption path in the weak ground state coupling regime as explained before. This destructive interference is not perfect for realistic close-to-experiment parameters, which means there is residual population in $|3\rangle$. This is likely due to the finite detuning of the driving beam, that addresses the dark state ladder with states $|\Psi_n^0\rangle$, to the bright states $|\Psi_n^\pm\rangle$. When these bright states are off-resonantly excited, they introduce population in $|3\rangle$. The figure of merit is defined as the cavity population divided by the excited state population $\langle a^\dagger a \rangle / \langle \sigma_{33} \rangle$, which is proportional to the number of photons that can be generated in the system without having a spontaneous decay from state $|3\rangle$. From now on this ratio is called photons per excitation (PPE) value.

The factor changes significantly with Ω_{12}, where it shows a steep decrease from around 400 to 200 when increasing Ω_{12} as can be seen in Figure 5.11(a). After the initial steep decrease the PPE value stays almost constant. This reflects very well the aforementioned existence of two distinct regimes in the ground state coupling, which is also strongly reflected in the $g^2(0)$ value in Figure 5.10. Figure 5.11(b) shows the same scan for a low coupling constant g. Noteworthy is that the PPE factor is always below one, which means that there is more atomic population in state $|3\rangle$, than there is population in the cavity. This stems from the fact, that for a low coupling constant the dark states become non-orthogonal. Furthermore outside of the strong coupling regime, the field, that couples the two ground atomic states is able to induce transitions between dark-bright and bright-bright pairs, thus increasing the population of the atomic excited state. Figure 5.12 shows how the PPE factor changes, when different properties of the system are changed including the before mentioned dependence on the coupling constant. It seems that the PPE value exhibits a proportionality to three parameters of the system, namely g^2, $1/\kappa$ and $1/\gamma_{deph}$, where γ_{deph} is a so far not mentioned dephasing between
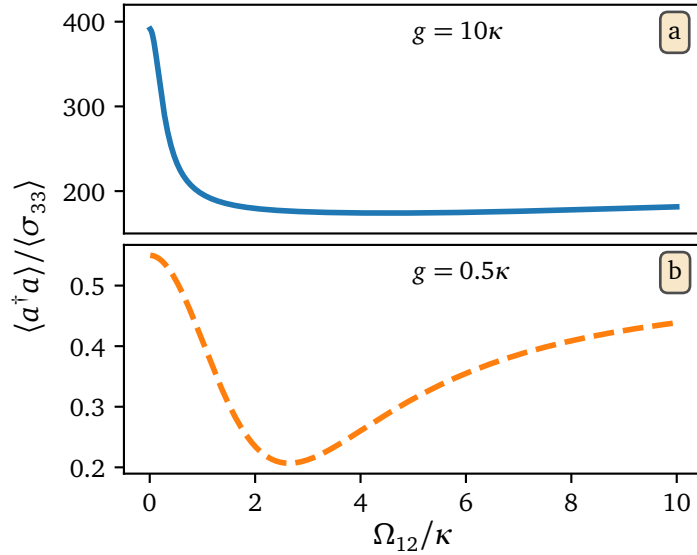
Figure 5.11: Shown is the value of $\langle a^\dagger a \rangle / \langle \sigma_{33} \rangle$ over a wide range of Ω_{12} for two different values of the coupling constant g.

the two ground states in the system, which is very relevant when it comes to limitations in a real system. Real experiments always exhibit a certain dephasing between the ground states. For high values of Ω_{23} and therefore a short lifetime of the dark states, the PPE factor is slowly decreasing, because the overlap with the bright states increases. It is also interesting how the system behaves when the excited atomic state is neither resonant to the cavity nor to the $|2\rangle$ to $|3\rangle$ laser. This is especially interesting, as a standard technique to avoid excited state population is, by working in a detuned regime of some excited atomic state as e.g. in far detuned Raman-transitions.

Figure 5.13 shows a simulation, in which the frequency of the excited atomic state is detuned from the cavity and the $|2\rangle$ to $|3\rangle$ laser, which stay at the same frequency. Part (a) shows the cavity population, which is proportional to the photon production rate for a fixed κ. This clearly illustrates that the efficiency, with which the system runs for a constant drive is strongly dependent on the detuning of the excited state. The highest efficiency is reached exactly on atomic resonance. Even though the atom is resonantly driven there, the PPE factor is barely affected with a relative change of below 5%.
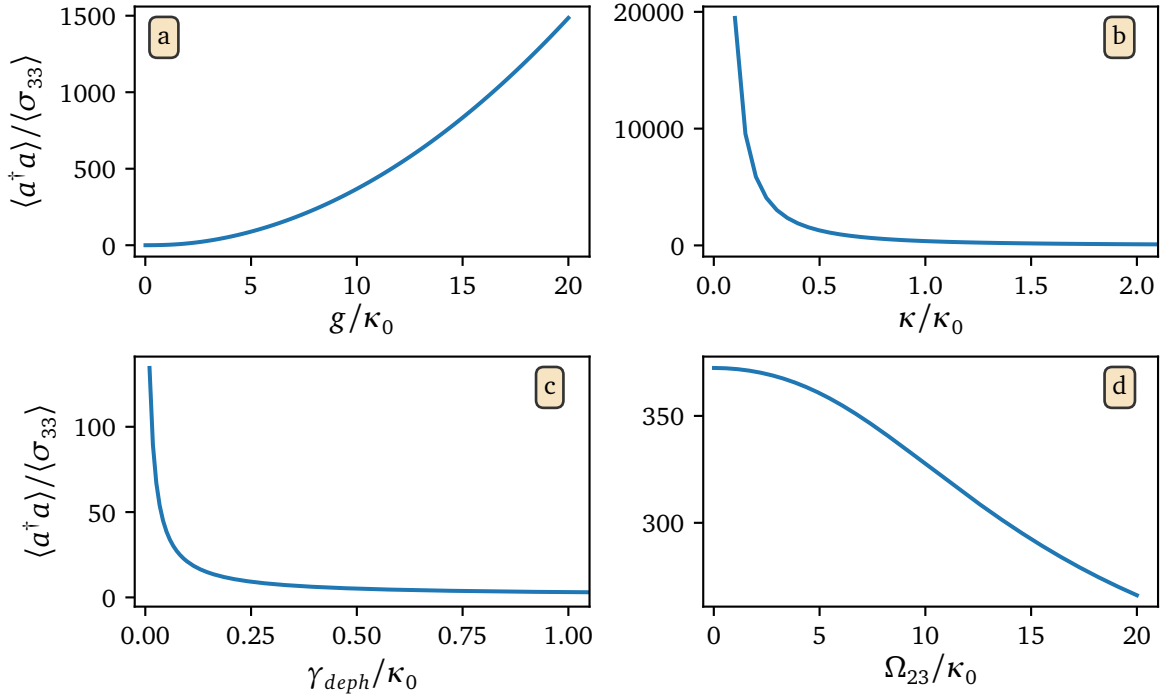
Figure 5.12: Shown is the value of $\langle a^\dagger a \rangle / \langle \sigma_{33} \rangle$ when tuning several different parameters of the simulation. When scanning one parameter all others are fixed to $\kappa_0 = 1, \Omega_{12} = 0.1\kappa_0, \Omega_{23} = 3.0\kappa_0, g = 10\kappa_0, \gamma_{33} = 1.0\kappa_0, \gamma_{deph} = 0.0\kappa_0$.
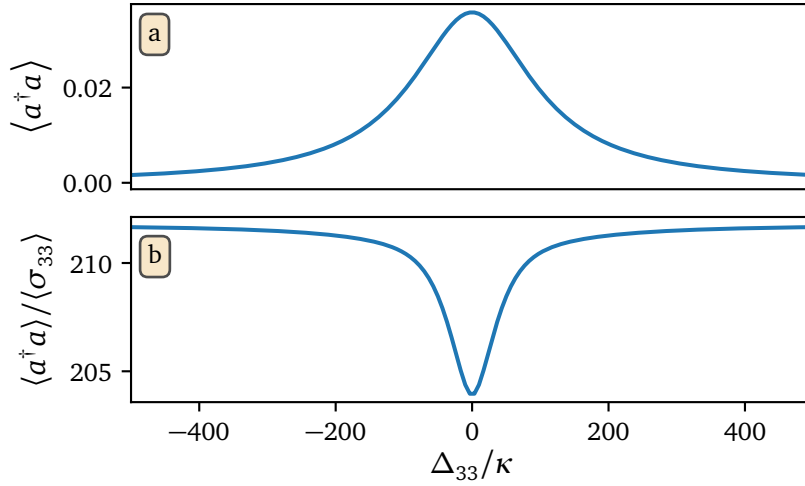
Figure 5.13: Different observables against the detuning of the excited atomic state Δ_{33}. (a) shows the cavity population, (b) shows the PPE factor. The other simulation parameters are $\Omega_{12} = 1.0\kappa, \Omega_{23} = 2.0\kappa, g = 10\kappa$

5.3. Experimental results

The last chapter focused on the theoretical framework and findings in a coherently closed atomic cycle with a cavity. This chapter will now focus on the experimental implementation in a strongly coupled atom-cavity system in the lab. The presented level scheme from the last chapter is implemented on the D2 line of the ^{87}Rb atom. The states $|1\rangle, |2\rangle, |3\rangle$ are implemented as:

$$
\begin{aligned}
|1\rangle &= |5S_{1/2}, F = 1, m_F = +1\rangle \\
|2\rangle &= |5S_{1/2}, F = 2, m_F = +2\rangle \\
|3\rangle &= |5P_{3/2}, F'' = 2, m_{F''} = +2\rangle
\end{aligned}
\tag{5.8}
$$

The experimentally achieved parameters are $(\kappa, g)/2\pi = (1.5, 10.2)\,\text{MHz}$, where κ is the field decay rate and g the atom cavity coupling constant on the $|1\rangle \leftrightarrow |3\rangle$ transition. A
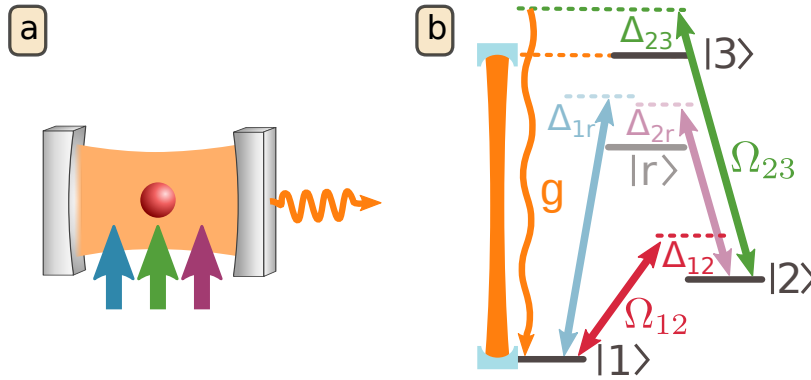
Figure 5.14: (a) shows a sketch of the driving configuration with three lasers irradiating the atom transversely, out of which two form a Raman pair. (b) shows the experimental level scheme, that differs from the theoretical one in Figure 5.1 by using a Raman transition to couple the two ground states with single photon detunings Δ_{1r} and Δ_{2r}.

sketch of the driving configuration and the experimental level scheme used are depicted in Figure 5.14.

5.3.1. Raman as ground state coupling

Now that the mapping of the states $|1\rangle$, $|2\rangle$ and $|3\rangle$ to real states of the ^{87}Rb atom is fixed, the next step for the realization of the theoretically investigated system is to implement the drives between these levels. The drive between level $|2\rangle$ and $|3\rangle$ can easily be implemented by using a conventional diode laser as the transition frequency is around 384 THz and therefore right at the transition between optical and near infrared where off-the-shelve lasers are available. The transition between $|1\rangle$ and $|2\rangle$ has a transition frequency of 6.8 GHz and is therefore in the microwave (MW) regime. Direct driving of this transition via a microwave has proven disadvantageous in the setup. A suitable

alternative are Raman transitions as discussed in Section 3.8. The Raman method couples two atomic states via a resonant two-photon process with optical light fields exhibiting a finite detuning to an excited atomic state $|r\rangle$. The interaction with the excited state is off-resonant, preventing excitation of this state. This is important because excitation leads to spontaneous decay into potentially uncoupled states and leads to dephasing in the system. Figure 5.15 shows the experimentally used Raman lasers. The two photon process from $|5S_{1/2}, F = 1, m_F = +1\rangle$ to $|5S_{1/2}, F = 2, m_F = +2\rangle$ couples via the detuned excited state $|r\rangle = |5P_{1/2}, F' = 2, m_{F'} = +2\rangle$ with a detuning of $\approx 4.5\,\text{GHz}$.
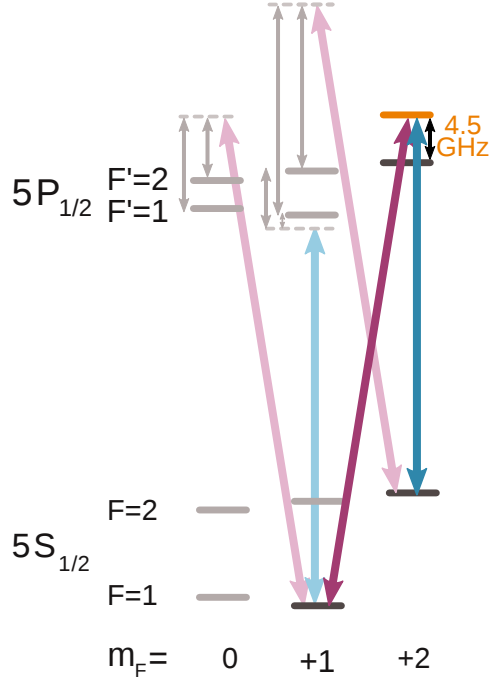
Figure 5.15: The Raman beams with their respective energy (length of arrow) and polarization (direction of arrow) are shown with the relevant part of the level diagram of the atom.

From the detunings and power levels it is possible to calculate the off-resonant scattering rate. According to [55] the scattering rate is given by:

$$\Gamma_{sc} = \frac{3\pi c^2 \Gamma_{D1}^2}{2\hbar \omega_{D1}^3 \Delta^2} I \tag{5.9}$$

where Γ_{sc} is the scattering rate, Γ_{D1} the decay rate of the excited state, ω_{D1} the transition frequency, Δ the detuning of the driving laser to the transition frequency, $I = \frac{1}{2}\epsilon_0 c E^2$ the intensity at the atom and E the electric field. According to Equation 3.8 this can be rewritten to:

$$\Gamma_{sc} = \frac{3c^2 \Gamma_{D1}^2 P}{\hbar \omega_{D1}^3 \Delta^2 w_0^2} \tag{5.10}$$

where P is the beam power which is easily measurable and w_0^2 is the beam waist at the atom's position which is determined in Section 3.8. To calculate the scattering rate in a multi level atom it is necessary to sum up all scattering rates of the lasers to different transitions they can couple to. This leads to the following formula if both Raman lasers have the same power $P_1 = P_2 = P$ [55]:

$$\Gamma_{sc} = \frac{3c^2\Gamma_{D1}^2 P}{\hbar\omega_{D1}^3 w_0^2} \left(p_1 \sum_{|1\rangle\to i} \left(\frac{CG_i^2}{\Delta_i}\right)^2 + (1-p_1) \sum_{|2\rangle\to i} \left(\frac{CG_i^2}{\Delta_i}\right)^2 \right) \tag{5.11}$$

where p_1 is the fraction of the atomic population that is in state $|1\rangle$, whereas the rest is in $|2\rangle$ and CG_i is the respective Clebsch-Gordon coefficient of the i'th transition. All relevant transitions for the Raman ground state coupling are summarized in Table 2.

GS	ES	$\Delta[GHz]$	CG$\cdot\sqrt{12}$
F1 $m_\mathrm{F}1$	F'1 $m_\mathrm{F}1$	-1.9	$+1$
F1 $m_\mathrm{F}1$	F'2 $m_\mathrm{F}1$	-2.7	$-\sqrt{3}$
F1 $m_\mathrm{F}1$	F'1 $m_\mathrm{F}0$	5.3	$+1$
F1 $m_\mathrm{F}1$	F'2 $m_\mathrm{F}0$	4.5	-1
F1 $m_\mathrm{F}1$	F'2 $m_\mathrm{F}2$	4.5	$-\sqrt{6}$
F2 $m_\mathrm{F}2$	F'2 $m_\mathrm{F}2$	4.5	$-\sqrt{4}$
F2 $m_\mathrm{F}2$	F'1 $m_\mathrm{F}1$	12.1	$\sqrt{6}$
F2 $m_\mathrm{F}2$	F'2 $m_\mathrm{F}1$	11.3	$-\sqrt{2}$

Table 2: Summary of all relevant atomic transitions with their detuning in the experiment and the respective Clebsch-Gordon coefficients. GS stands for ground states, ES for excited state.

Evaluating the scattering rate for the highest laser powers used in the experiment leads to rates of up to 8.8 kHz, if the whole atomic population is in state $|1\rangle$. This value is already substantial. This has two effects on the physical system presented here. First, it leads to decoherence, because whenever a scattering event happens the system is projected out of the dark states. Second, a scattering event means a spontaneous decay of the atom to some random state (with a branching ratio given by the effective coupling strengths). A second effect of driving the system with off-resonant but strong laser beams is that the transitions experience a Stark shift due to the interaction of the atom with the light. The Stark shift for the transition between $|1\rangle$ and $|2\rangle$ is now given by [55]:

$$\Delta E = \Delta E_{|2\rangle} - \Delta E_{|1\rangle} = \frac{3c^2\Gamma_{D1} P}{\omega_{D1}^3 w_0^2} \left(\sum_{|2\rangle\to i} \frac{CG_i^2}{\Delta_i} - \sum_{|1\rangle\to i} \frac{CG_i^2}{\Delta_i} \right) \tag{5.12}$$

A calculation with all coupling transitions from Table 2 results in a Stark shift of:

$$\Delta E_{theo} = 1.2 \frac{\text{MHz}}{\text{mW}} \tag{5.13}$$

The measured Stark shift of the transition for different Raman driving powers is shown in Figure 5.16. A linear fit reveals a Stark shift slope of:

$$\Delta E_{exp} = 1.1(1) \frac{\text{MHz}}{\text{mW}} \tag{5.14}$$

This is in very good agreement with the theoretically expected value, showing that the system is well understood and that the calculation of the beam waist at the atom position as done in Section 3.8 is accurate.
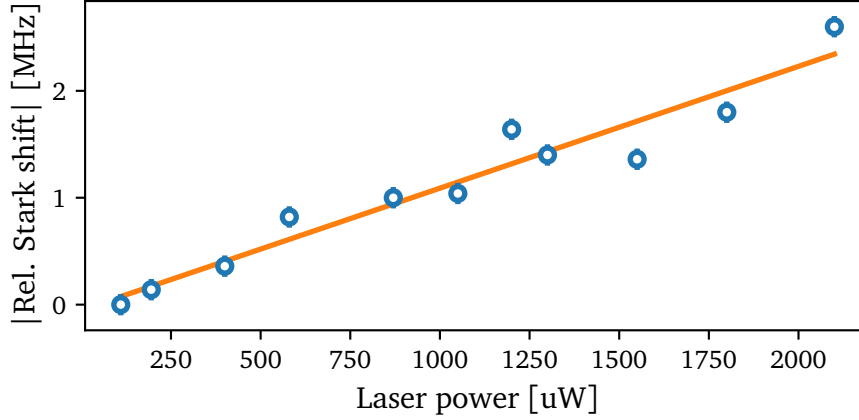

Figure 5.16: Shown is the absolute value of the relative Stark shift over the power of both lasers (that had the same power), as determined from the peak position in multiple spectra as in Figure 5.18.

5.3.2. State preparation

The experimental sequence starts in state $|1\rangle = |5S_{1/2}, F = 1, m_F = +1\rangle$, which needs to be prepared beforehand. Preparing this state is unfortunately not straight forward by optical pumping, as it cannot act as an uncoupled state for any configuration of lasers in the current setup. The used sequence to maximize the population in the desired state is shown in Figure 5.17.

The ground state manifold $|F = 2\rangle$ is depopulated by a 221 (coding is explained in caption of Figure 5.17) and a 222 beam in π-polarization and an additional 221 beam in lin$\perp$lin configuration (see Section 3.4 for laser directions and an explanation of the polarization). These together do not exhibit an uncoupled state in $|F = 2\rangle$ and therefore everything ends in $|F = 1\rangle$. But the population of Zeeman-substates within this manifold is random. To counteract this, an additional 212 beam in σ^+-polarization is used, which drives transitions with $\Delta_{m_F} = +1$ to the excited manifold $|F'' = 2\rangle$. From there it can either decay to the $|F = 1\rangle$ or to the $|F = 2\rangle$ manifold, but on average it decays to a higher Zeeman-substate ($\bar{m}_{F,after} > \bar{m}_{F,before}$). Because there are no uncoupled states in the system, this method of state preparation slowly approaches an equilibrium with a high, although not complete population in $|1\rangle = |5S_{1/2}, F = 1, m_F = +1\rangle$. This residual imperfection is
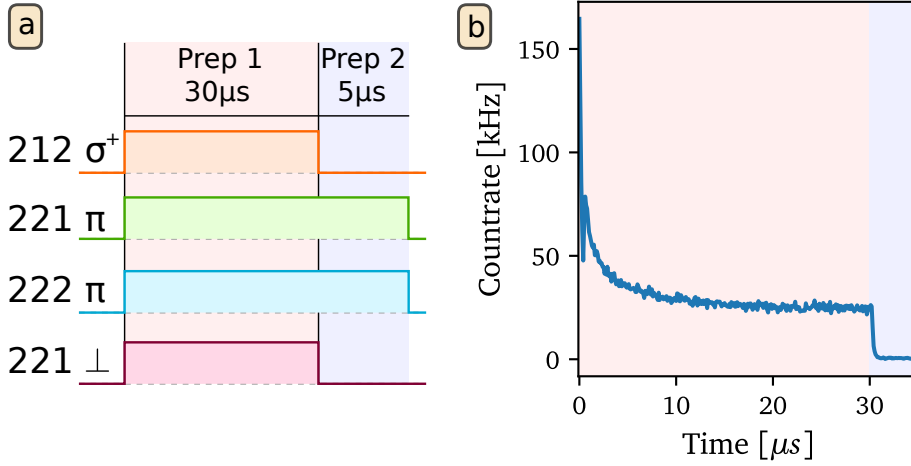
Figure 5.17: (a) shows the sequence that was used to prepare state $|1\rangle$ with the different lasers and their respective polarization. The laser names are encoded as n1n2n3, where n1 stands for either D1(1) or D2(2) line of ^{87}Rb, n2 is the ground state F-manifold and n3 the excited state F-manifold. 212 e.g. drives the transition from $|5S_{1/2}, F = 1\rangle$ to $|5P_{3/2}, F'' = 2\rangle$. (b) shows the countrate during the state preparation sequence versus time. The colorful shades correspond in both pictures to the same pulse.

caused by depumping by the 212 laser. One problem is that, if the 212 beam and the 222 beam exhibit a two photon detuning that is resonant to a transition from $|F = 1, m_F = 1\rangle$ to $|F = 2, m_F = 2\rangle$, a superposition state as in cavity EIT will form between them. To prepare all population in this state into the $|F = 1, m_F = 1\rangle$ a second state preparation pulse is applied, where the 212 laser is turned off, leaving the system in the desired state. The quality of the state preparation can be measured by a spectrum of the ground state coupling. The cavity produces photons when the Raman transition between the two ground states, $|F = 1\rangle$ and $|F = 2\rangle$, exhibits a two-photon detuning that is resonant to the transition between a pair of Zeeman substates, with one substate in each ground state. The Zeeman substates exhibit a frequency splitting due to the applied magnetic field. The transitions that are allowed are given by the interplay between laser polarizations and magnetic field direction and are the same as in Section 3.8. The second step with the laser from $|2\rangle$ to $|3\rangle$ couples all Zeeman substates in the $|F = 2\rangle$ ground state manifold, as the transition including the cavity is broader than the Zeeman splitting. When this three-photon detuning is appropriate, a light field builds up inside of the cavity that decays from the cavity with rate κ and is then measured. The spectral response of the system, when tuning the Raman driving frequency is depicted in Figure 5.18. As can be seen, there are multiple peaks visible with the rightmost peak dominating. The rightmost peak belongs to the transition from $|F = 1, m_F = 1\rangle$ to $|F = 2, m_F = 2\rangle$, as indicated in the plot. This is the transition that is actually desired. All other depicted transition are parasitic and their respective peak would vanish for a perfect state preparation. Unfortunately a perfect state preparation is not possible in the current configuration of the experiment,
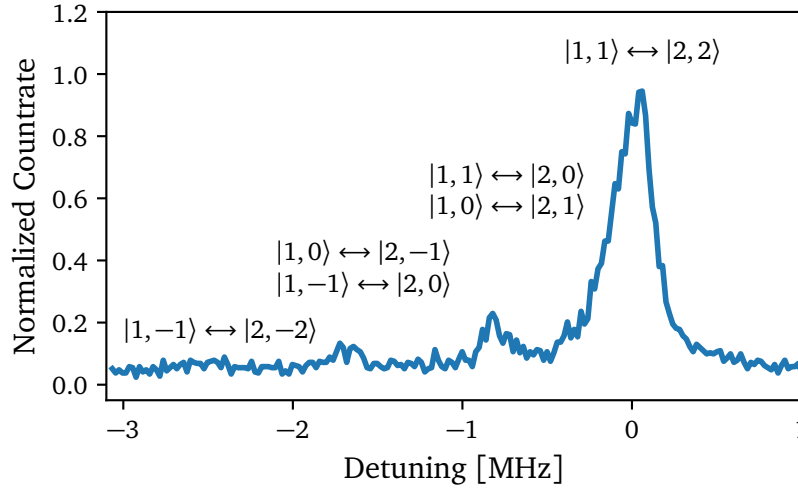
Figure 5.18: Normalized countrate when the two-photon detuning of the Raman transition is scanned. The text above the peaks indicates the respective transition. Some transitions are degenerate.

therefore a loss of around 20% of the population that is initially in undesired states has to be accepted. This effect expresses itself as a diminished signal in the subsequent experiments but does not lead to biased results when only the rightmost peak is driven.

5.3.3. Energy spectrum of the system

It is now interesting to investigate the system spectrally to understand its energy level structure. This can be done by scanning the ground state coupling frequency with detuning Δ_{12} against the detuning Δ_{23} of the excited state coupling. Because Δ_{12} is essentially the two-photon Raman detuning, scanning one of the two Raman lasers is equivalent to scanning Δ_{12}. This measurement reflects the eigenstates of the system's first energy manifold as introduced in the theory section in Section 5.2.1. Whenever one of the excited states in the first manifold is resonant to the configuration of driving frequencies, light is generated in the cavity. The system is restricted to mainly the first energy manifold because the driving strength remains low. The result of the experiment is shown in Figure 5.19. This experimental result agrees qualitatively very well with the simulation of the same observable as shown in Figure 5.2. The orange lines in the plot stem from the theoretically calculated energies of the first manifold for the ideal system without ground state coupling. The fact that these replicate the measurement indicates that treating the ground state coupling as a small perturbation is indeed valid. The highest photon production rate is reached at $\Delta_{12} = \Delta_{23} = 0$ with a rate on the order of $100\,\text{kHz}$.

5.3.4. Four wave mixing and spectrum

The output light field is produced in a process that looks similar to four wave mixing as it uses a typical double-lambda system [26]. The output light field should, in such a case,
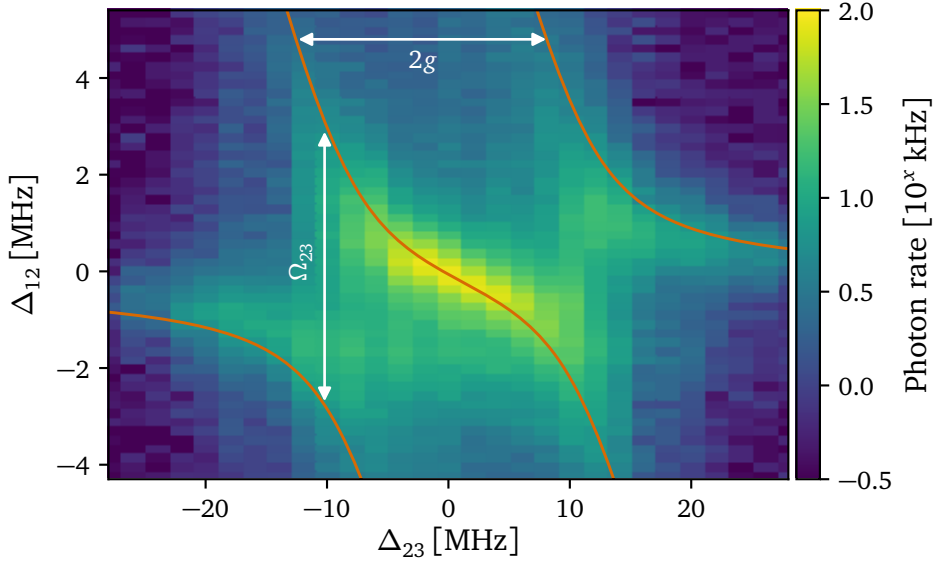
Figure 5.19: Logarithmic plot of the cavity output rate for a two-dimensional scan of the excited state coupling Δ_{23} and the ground state coupling Δ_{12}. The orange lines show the solution of an analytical theory.

obey certain wave mixing conditions. The output light should have the same frequency as the sum of the input light fields, which can be expressed as:

$$\omega_{\text{fwm}} = \omega_{1r} + \omega_{23} - \omega_{2r} \tag{5.15}$$

where ω_{fwm} is the frequency of the output light field from the cavity. To investigate the system's behavior under change of the input light frequencies, it is necessary to measure the output field in a spectral measurement with very high precision. This is done with a heterodyne setup as described in Section 3.5. The result is shown in Figure 5.20. Several things are noteworthy. First of all, the output frequency of the light field follows the inputs, as in classical four wave mixing. This already proofs that it is indeed a four wave mixing process happening in the system. Furthermore the peaks exhibit an extremely small spectral width of around 20 kHz. This width is likely Fourier-limited, because the light field was only generated and measured in a pulse of 55 μs, suggesting the width would be even smaller for a longer measurement duration. This means the generated light field is fully coherent with the input light fields. The heterodyne local oscillator beam, with which the generated field is interfered, is derived from a separate laser, which is not involved in driving of the system. This means the generated light is even fully phase coherent with the frequency comb used in the laboratory, to which all lasers are stabilized. This very small spectral linewidth, likely even Fourier-limited, is indeed in qualitative agreement with simulations, where the system's spectrum is a delta function without experimental imperfections. This is due to the Zeno-blockade, due to which the system exhibits two-level system behavior with coherent elastic scattering (for details see Section 5.2.3). The incoherent peaks of the Mollow triplet are several order of magnitude weaker, leading to an insufficient signal-to-noise ratio to detect them in this measurement.
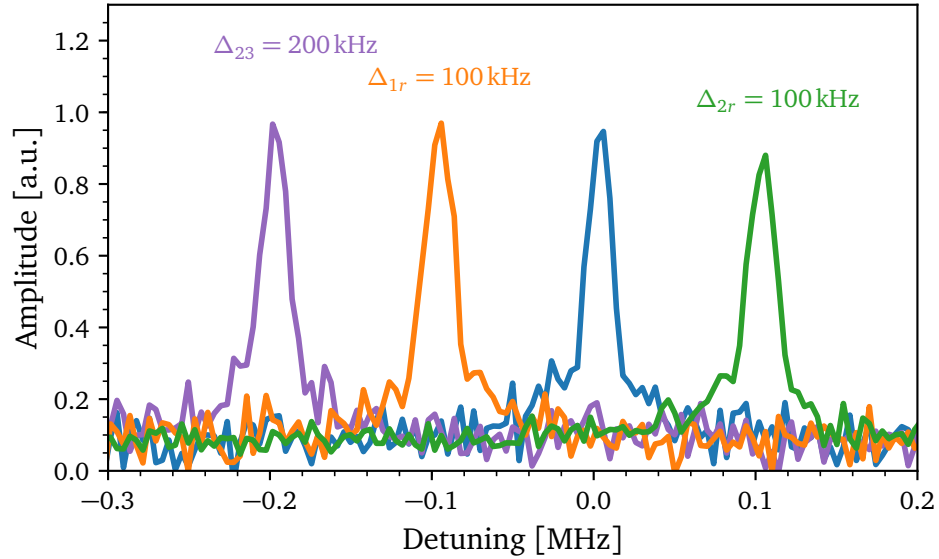
Figure 5.20: Heterodyne spectrum showing four wave mixing for different detunings of
the input fields. The blue curve shows the spectrum for vanishing detunings
($\Delta_{1r} = \Delta_{2r} = \Delta_{23} = 0$), the orange curve for $\Delta_{1r} = 100\,\text{kHz}$, the the green
curve for $\Delta_{2r} = 100\,\text{kHz}$ and the purple curve for $\Delta_{23} = 200\,\text{kHz}$. The
amplitude is normalized to the largest amplitude.

5.3.5. Excitation-less photon generation

This and the later chapters focus on the dark-state ladder as introduced in the theory
section under Section 5.2.1 and are measured for resonant driving ($\Delta_{12} = \Delta_{23} = 0$)
unless otherwise noted. The emission from the cavity when driving dark states stems
from the decay of the states with $n \geq 1$, which all contain a cavity component. Exemplary
for $n = 1$, the dark state is $\left|\Psi_1^0\right\rangle \propto \Omega_{23}\left|1,1\right\rangle - g\left|2,0\right\rangle$, where the state $\left|1,1\right\rangle$ can decay
via the cavity. As already mentioned in the corresponding theory chapter in Section 5.2.5,
driving the dark states still leads to residual population in the excited atomic state as the
detuning of the bright states is finite. So the signal that a dark state transition is driven
is a reduction of the excited state population in comparison to a free-space atom with
the same resonant light fields applied. Experimentally, it is not easy to probe the excited
state population because this would require a state detection sensitive to population in
this state. This is hard, because the excited state has a very short lifetime and a detection
technique would need to probe the state faster than $1/\gamma_3 = 26\,\text{ns}$ [54]. However, there is
an indirect method to serve the same purpose, based on the natural decay of the excited
state. Whenever the atom is in the excited state manifold, it does decay with a certain
branching ratio to different ground states. A level scheme with the relevant states for
^{87}Rb is shown in Figure 5.21(a). If state $\left|3\right\rangle$ is populated it decays with the following
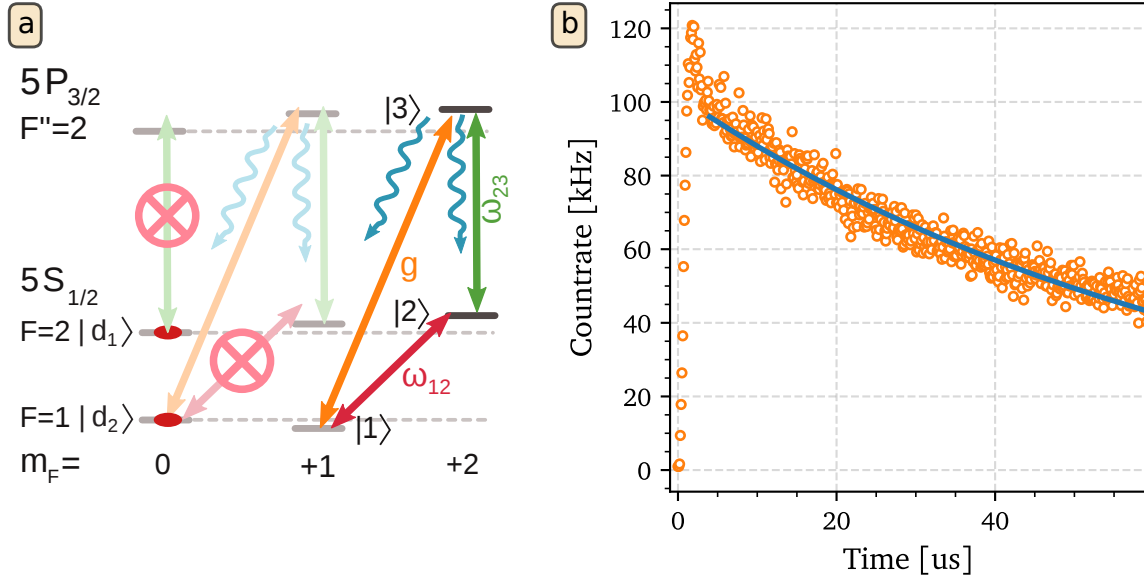
Figure 5.21: (a) shows the full atomic level scheme that is relevant to the experiment with the allowed and forbidden transitions and the uncoupled states in which the atomic population accumulates for long interrogation times. (b) shows the measured countrate of the cavity output over time (orange) and a fit of this exponential decay (blue).

branching ratios (that can be deduced from the Clebsch-Gordon coefficients):

$$|3\rangle \rightarrow |F = 1, m_F = +1\rangle = 6/12$$
$$|3\rangle \rightarrow |F = 2, m_F = +1\rangle = 2/12 \tag{5.16}$$
$$|3\rangle \rightarrow |F = 2, m_F = +2\rangle = 4/12$$

This means the atom decays in $2/12 = 16\%$ of the cases to state $|F = 2, m_F = +1\rangle$ and therefore out of the closed system. As the transition from there to the excited state $|F'' = 2, m_{F''} = +1\rangle$ is spectrally broad, the same laser of the $|2\rangle \leftrightarrow |3\rangle$ transition also drives this transition. This either leads again into the closed system $|1\rangle \leftrightarrow |2\rangle \leftrightarrow |3\rangle$, back to $|F = 2, m_F = +1\rangle$ or ends up in one of the states denoted by $|d_{1,2}\rangle$. These two states are uncoupled by the driving lasers and the population remains trapped there. In the $|d_2\rangle$-case, this is based on the detuning of the driving laser, as the width of this ground state transition is smaller than the frequency splitting of the Zeeman-substates due to the applied magnetic guiding field along the cavity. In the case of $|d_1\rangle$, this is due to the selection rules that prevent a coupling via π-polarized light to the excited state manifold $|F'' = 2\rangle$. These two uncoupled states are no longer able to produce photons. This leads to a characteristic number of photons that such a system can scatter before it is depumped into one of these uncoupled states. This characteristic photon number is inversely proportional to the average atomic excited state population. Figure 5.21(b) shows the measured photon rate for the system over time. After the initial dynamics with a fast increase in the countrate, the photon rate decreases exponentially due residual excitation of state

$|3\rangle$ and subsequent decay into the uncoupled states. The orange bars in Figure 5.22(a) show the photon number distribution in this 60 µs long measurement interval for a large number of measurements. The average number of photons per experiment is then 4.0. Because of the exponential character of such a decay it is straightforward to extrapolate this value for infinite measurement times via:

$$\langle \bar{n} \rangle = \int\limits_{0}^{\infty} A \cdot e^{-t/\tau} dt = A \cdot \tau \tag{5.17}$$

with A the amplitude of the exponential decay and τ the decay constant.
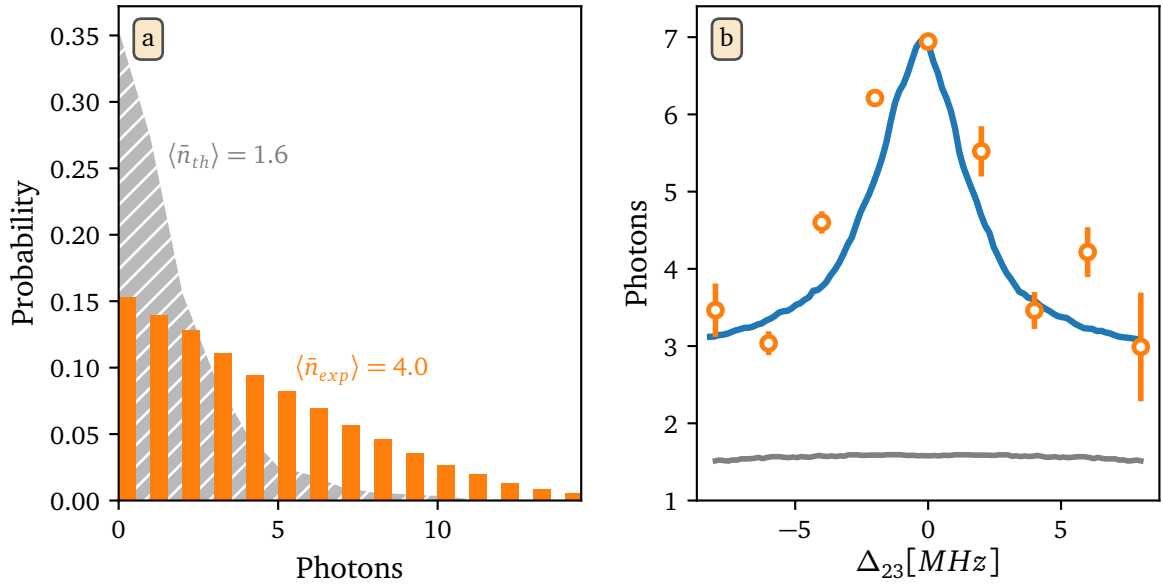
Figure 5.22: (a) shows the theoretic photon number distribution without a cavity for infinite measurement time (gray) and the experimentally measured photon number distribution (orange) for 60 µs measurement time. Both are for $\Delta_{12} = \Delta_{23} = 0$. (b) shows the total average photon number against the detuning Δ_{23}. The gray curve shows the simulation without a cavity and the orange data points show the measurement as extrapolated for infinite measurement times from the exponential decay. The blue curve is a quantum simulation for the system that is scaled and shifted to accommodate the data. All simulations are performed in a full quantum simulation with all participating atomic levels and decays between them.

For the measurement in Figure 5.22(a) this results in a total of 6.9(1) photons before the system is fully decayed. Noteworthy is that the experimental detection efficiency of the photons in the cavity to actually detected photons is only 26% (which means a perfect detection system would measure 26.5 photons). To show that these photons indeed stem from a transition between dark states it is necessary to compare the measured value to the identical system without a cavity. As there is no dark state-ladder in the free space

equivalent of the experiment, the only way to produce a photon is by decaying from the excited state and not via a dark state transition. In this situation the atom would scatter in the full solid angle of 4π. Assuming a detector collecting all photons of the right frequency and the same photon detection efficiency as in the experiment, this would lead to an average photon number of only 1.6 before the system is fully depumped into uncoupled states. This number is based on a full quantum Monte-Carlo simulation of the system for infinitely long measurement time including all relevant atomic states and decay channels. The number of photons in the experiment is a 4.3-fold increase compared to that and clearly shows, that the produced photons indeed result from a transition between dark states. This experimental value is mainly limited by the finite coupling strength g, the non-negligible dephasing rate between the ground states of $\gamma_{\mathrm{deph}}/2\pi = 64(1)\,\mathrm{kHz}$ [82], the position distribution of atoms within the cavity and the scattering rate of the Raman-transition between $|1\rangle$ and $|2\rangle$. As already shown in the excited state population in the theory figure in Figure 5.2, the avoidance of the excited state is only good for vanishing three photon detuning $\Delta_{12} + \Delta_{23} = 0$. Therefore it is interesting to see that the average number of photons also reproduces this result. Without a loss of generality only a one-dimensional scan in Δ_{23} was performed. The results are depicted as orange dots in Figure 5.22(b). These clearly show a resonance with a peak at vanishing detuning with 6.9 photons for infinite measurement time. Shown in blue is a theoretical calculation of the photon number from a Monte-Carlo simulation of the system. The mainly flat gray line at around 1.6 photons is a simulation for the free-space atom case for exactly the same scan. The emergence of a resonance, and also the far larger total photon number again proofs that the photons indeed stem from a dark state transition.

5.3.6. Photon statistics

The dynamics of the system within the dark state ladder can be analyzed via the second order correlation function $g^{(2)}(\tau)$. Multiple measured correlation functions are shown in Figure 5.23. Figure part (a) shows the correlation function for different values of Ω_{23}. The data shows strong photon antibunching and sub-Poissonian statistics due to the Zeno-blockade effect as higher rungs in the dark-state ladder are suppressed and the dynamics are limited to the first two dark states $|\Psi_0^0\rangle$ and $|\Psi_1^0\rangle$ (see also Section 5.2.2). The correlation function is mainly shaped by two parameters. First the effective Rabi frequency that determines the coherent evolution of the system with Rabi-oscillations between these two states and second the decay rate of the first dark state. The green curve is a fit of a damped sinusoidal function that results in a frequency of 327(14) kHz, which is in decent agreement with $\Omega_{12}/2\pi = 400\,\mathrm{kHz}$, which is the calculated value from the laser powers and the known beam waist. As already introduced in the theory chapter (Section 5.2.2), the decay rate of the first dark state can be calculated via Fermi's golden rule. Together with the known dephasing rate of our ground-state superposition of $\gamma_{\mathrm{deph}}/2\pi = 64(1)\,\mathrm{kHz}$ [82] the dephasing time is 2.0 µs for $\Omega_{23}/2\pi = 2.0\,\mathrm{MHz}$ (orange dots in Fig. 5.23(a)), which agrees well with the experimentally measured value of 1.7(2) µs. Also visible in Figure part (a) is, that the correlation function does not change
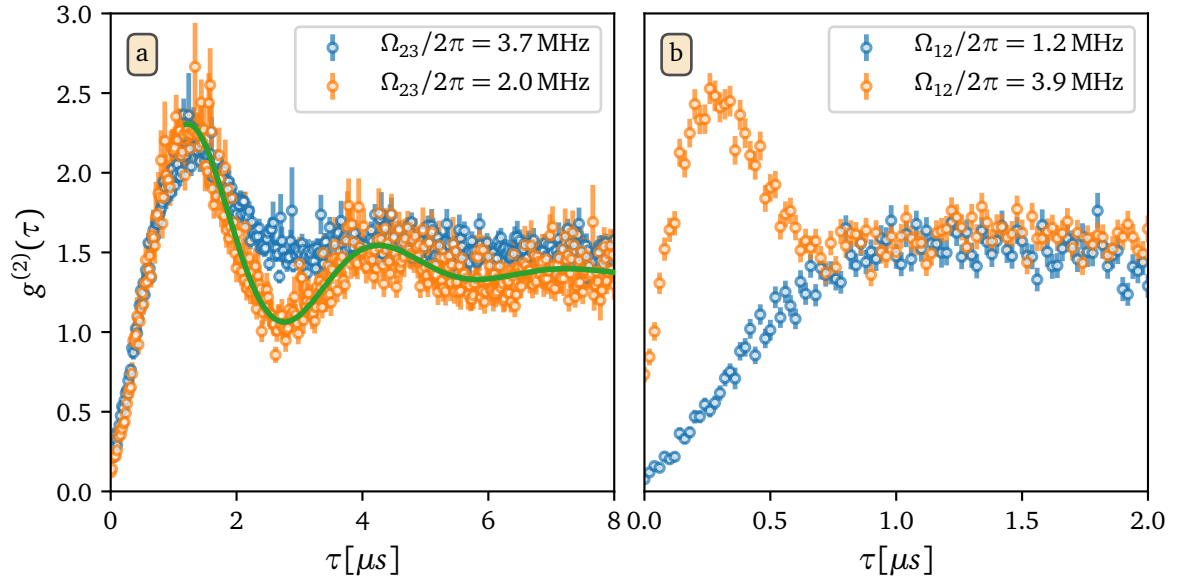
Figure 5.23: Both graphs show the second order correlation function $g^{(2)}(\tau)$ for $\Delta_{12} = \Delta_{23} = 0$. (a) shows this function for different values of Ω_{23} for a fixed value of $\Omega_{12}/2\pi = 400\,\text{kHz}$. The orange data points are fitted by an exponentially decaying sine wave as shown in green. (b) shows the correlation function for different values of Ω_{12} for a fixed value of $\Omega_{23}/2\pi = 5.0\,\text{MHz}$. The binning for the correlation function in this measurement was $20\,\text{ns}$ and the error bars are statistical.

its frequency for different values of Ω_{23}, as this does not have an effect on the effective driving strength (in the regime $g \gg \Omega_{23}$), but indeed it has a strong effect on the lifetime of the first dark state and therefore on the oscillation decay rate. The $g^{(2)}(0)$ value also changes, which is the topic of the Section 5.3.7. Figure 5.23(b) shows the correlation function for different values of Ω_{12}. The blue curve exhibits no visible oscillation because the system operates in the overdamped regime, where the decay is faster than the driving. When the effective Rabi frequency is increased, an oscillation emerges, completely similar to the result in a two-level atom. So it is indeed Ω_{12} that primarily determines the oscillation frequency in the discussed parameter regime. Also the $g^{(2)}(0)$ value changes dramatically, which is discussed in Section 5.3.8. In summary, the correlation functions accurately depict the dynamics between the first two states in the dark state ladder and agree very well with theoretical expectations for a two-level system implemented in the dark states.

Intuitively it might seem contradictory that the heterodyne measurement in Figure 5.20 shows a linewidth of the emitted field of only $20\,\text{kHz}$, implying a coherence time of around $50\,\mu\text{s}$, whereas the correlation measurement in Figure 5.23 only shows a coherence time of around $2\,\mu\text{s}$. As was already shown and discussed in [79, 83], this is no contradiction at all, because first order coherence, as measured via the heterodyne detection, does not imply second order coherence, as measured via photon correlation. A heterodyne

detection is based on interference between light fields and emphasizes the wave properties of light. On the other hand the photon detection measures the particle-like properties of the generated light emphasizing the quantum properties.

5.3.7. Zeno blockade

Section 5.2.2 already discussed the existence of a quantum Zeno effect in the dark state ladder that leads to a blockade of higher dark state rungs. This blockade can be tuned by the value of Ω_{23}. As already discussed in previous chapters, the $g^{(2)}(\tau)$
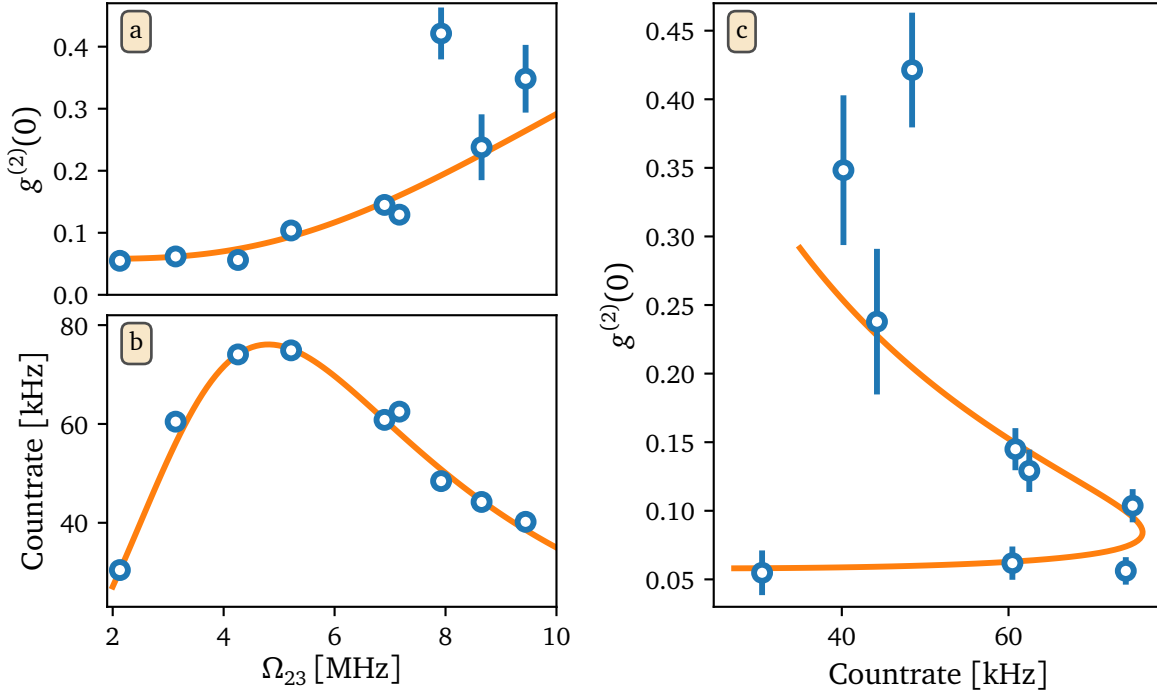
Figure 5.24: (a) shows the equal-time correlation value $g^{(2)}(0)$ for different driving Rabi frequencies Ω_{23}. The other driving was fixed at around $\Omega_{12}/2\pi = 300\,\text{kHz}$. (b) shows the measured photon countrate from the cavity output for the same measurement. (c) shows the equal-time correlation value against the countrate for the same data set as in (a) and (b). The orange curves are theoretic expectations from a quantum simulation of the system. The theory curve is calculated with only independently determined parameters, except for the countrate, that is shifted by 6% (higher detection efficiency than expected).

correlation function is a suitable tool to investigate the dynamics in the dark state ladder. Especially the value for $\tau = 0$ is interesting as this is an indicator of the population of higher rungs in the dark state ladder, because the equal-time detection of two photons is only possible if the system was in a higher dark state, that has components of two or more photons. The experimental results of a scan in Ω_{23} are shown in Figure 5.24(a).

The equal-time correlation starts with a low value, which shows that the suppression of these higher rungs indeed causes the system to behave very much like a two-level system. When the Ω_{23} value is increased, higher rungs are unblocked and the equal-time correlation function increases. For very high values of Ω_{23}, it approaches the $g^{(2)}(0)$ value of a coherent state, which is one. Unfortunately, a measurement with such a high Rabi frequency was not possible due to limited laser power and excess stray light on the camera. Figure 5.24(b) shows the measured output photon countrate from the cavity. When the driving strength is increased, the photon production rate also increases but peaks at around $\Omega_{23}/2\pi \approx 4.5\,\text{MHz}$ and goes down again for higher driving rate. This behavior is expected from the full analytical formula for the effective driving strengths within the ladder as given in Section A.1. Figure 5.24(c) shows the $g^{(2)}(0)$ value against the measured photon countrate. It can be clearly seen, that the same countrate can lead to very different photon statistics. This shows that indeed the Zeno-blockade is lifted and it is not just an effect based on a potential filling of the cavity. All in all, the quantum theory of the system and the experimental result show a remarkable agreement. This is especially interesting because, aside from a 6% higher photon detection efficiency than expected, there are no free parameters for the theory, but only independently measured parameters, such as laser powers. This shows that the experimental system is well understood and accurately modeled. As a summary, it is possible to observe and tune the Zeno-blockade effect.

5.3.8. Strong coupling regime

As already described in Section 5.2.4, there is a second regime emerging in the presented system, when Ω_{12} becomes significant in comparison to g, Ω_{23} and κ. In this regime, the presented dark state ladder with the triplet of states in each manifold is no longer a valid view on the system. On the contrary, the system is split into two distinct, off-resonantly driven subsystems $|+\rangle$ and $|-\rangle$, as can be seen in Figure 5.1(b). The theory chapter about the strong ground-state coupling regime distinguished between three different regimes, with different results in the steady state cavity field when the system is driven. Experimentally only one of the regimes is accessible, namely $g^2 \gg 2\Omega_{12}\kappa$. The expectation in that regime is the formation of an incoherent mixture of two out-of-phase coherent states. Figure 5.25 shows a measurement where the ground-state coupling is varied in a range that spans the weak ground-state coupling regime to the strong ground-state coupling regime. This means the whole crossover between both regimes is shown. For small values of Ω_{12} the outgoing light field exhibits strong single-photon character from the Zeno-blockade effect, with $g^{(2)}(0)$ as low as 0.01(1). When the ground-state coupling is increased, the equal-time correlation value increases as well, approaching a coherent-state value of one. The orange curve in the background is a quantum simulation of the regime transition for a closed system without decay into uncoupled states. This simulation shows qualitative agreement but poor quantitative agreement. This is because strong ground-state couplings lead to very high photon production rates, that let the system decay into uncoupled states very fast. Furthermore this high scattering rate heats the atom in the trap and leads to short storage times and unsteady atomic position due
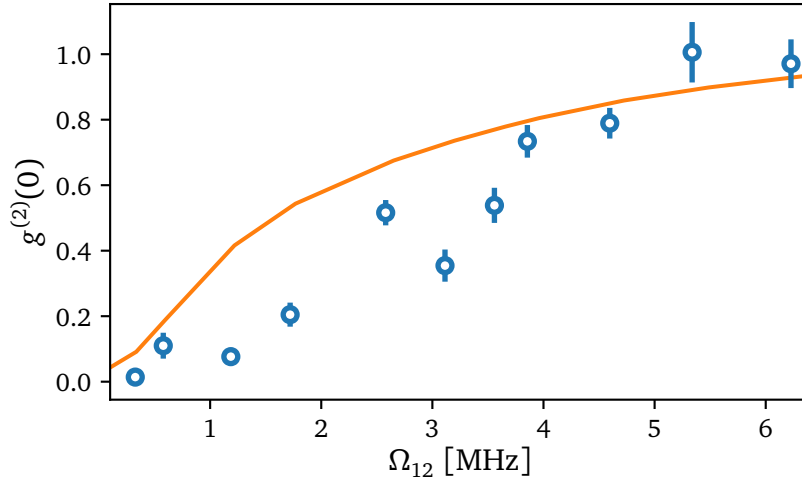
Figure 5.25: Shown is the equal-time correlation value $g^{(2)}(0)$ for different ground state coupling Rabi frequencies Ω_{12}. The values range from 0.01(1) up to values of around one. The other driving strength was $\Omega_{23}/2\pi = 4.7\,\mathrm{MHz}$. The orange curve in the background is a quantum simulation of the system without decay into uncoupled states.

to hopping between lattice sites. This hopping in return leads to time variations in the effective driving field strengths.

All in all, this measurement clearly shows the expected transition from weak to strong ground state coupling via the accompanying change in photon statistics, from the statistics of single photons to that of a coherent state. This nicely validates the theoretically shown existence of two regimes in this physical system. Remarkably, a driven single atom is able to produce a coherent field, in stark contrast to a free space atom, which is limited to the emission of single photons.

5.4. Summary

This chapter introduced a coherently closed cycle in the atomic level structure. The theory behind the formation of the dark states was explained and the ability to climb the ladder of dark states was introduced. Furthermore it was shown theoretically and experimentally, that it is possible to continuously produce a new field in the cavity, with a frequency that was not applied as an external drive. This light is produced without atomic excitation as it stems from transitions between dark states, that do not contain a component of the excited atomic state, although resonantly driven. The possibility to generate light without exciting the atom prevents the atom from decay into uncoupled states via spontaneous emission. Because this technique is not bound to a specific system, but broadly applicable, as long as strong coupling can be achieved in the respective system, it has broad applications in e.g. the fluorescence detection of molecules. These decay to uncoupled rovibrational states, limiting the amount of light that can be detected. In addition to that, this new field also has interesting properties that were investigated in

this chapter. First, the field was investigated via a heterodyne setup, which revealed that the field is spectrally very narrow-band and fully phase coherent to the driving lasers and can be tuned in frequency. Secondly, the field was also investigated via the $g^{(2)}$ photon correlation function, which showed Rabi-oscillations between the first two dark states in the weak driving regime. This also revealed a pronounced single-photon character, originating from a continuous Zeno-effect, blocking higher excitation rungs of the dark state ladder. Increasing the driving in the $|2\rangle \leftrightarrow |3\rangle$ arm of the Λ-system lifts the blockade and makes higher rungs accessible which is expressed in an increased equal-time photon correlation value for higher drivings. This is not an effect of filling up the cavity because the actual photon generation rate decreases. Furthermore also the strong ground state coupling regime was investigated and it was theoretically shown that this results in a Schrödinger-cat like state in the cavity for vanishing cavity decay, which evolves into a coherent state when the cavity decay increases. The transition between the weak and strong driving regime was also experimentally observed, showing the corresponding transition in the photon statistics from single photons to a coherent field.

6. Towards multi-mode cycle and giant Kerr effect

6.1. Introduction

This chapter adds another cavity mode to the cavity EIT system and is a first step towards the realization of a coherently closed atomic cycle with two cavity modes. It is not closed yet, as it does not include a link between the second, newly introduced excited state, and the first ground state. It additionally lacks coupling between the two ground states. But even without closing this system, it already shows such rich physics that it is well worth to be investigated on its own. The main effect of adding another strongly-coupled cavity mode is that the combined system is able to mediate interactions between photons of completely different fields with different wavelengths. In a previous version with a similar setup, strong coupling between photons of different fields was already demonstrated [82]. Bringing this interaction to the dispersive regime, where atomic excitation is negligible, gives rise to a so called cross Kerr nonlinearity. This form of the Kerr effect between two light fields is often discussed in the context of quantum non-demolition measurements with first (theoretical) applications appearing as early as the 1980s and 1990s [84, 85]. This interest is still unbroken [86, 87]. The investigation of cross Kerr nonlinearities is especially interesting in the context of cavity QED, as this enhances the nonlinearity to levels where a significant effect can be observed on the level of individual photons. In this regime, this giant cross Kerr nonlinearity can be used to non-destructively detect the presence of extremely low light levels with another light field, as was already demonstrated in the microwave regime [88, 89]. An extension of this effect to the strong dispersive regime (still with microwaves) allowed for counting of individual photons, and live observation of photons being created and destroyed [1, 2, 90]. Bringing these effects to the optical domain would be useful - especially in the context of quantum information processing - as the optical and near-infrared domains allow for good transmission lines [91] and long coherence times [92].

On a different note, cross Kerr nonlinearities are also known to mediate phase shifts between light fields, which sparked considerable research activity in that field in recent years [93–95] and is especially spread widely in the context of N-type level schemes [26, 96–98]. Bringing the cross Kerr effect to a level where a single gating photon could cause a phase shifts of π to another field, would allow for the realization of universal quantum gates between different light modes [99]. It should be mentioned that a study by *Shapiro* [100] contradicts the usability of this scheme for quantum gates because the non-instantaneous reaction of any realistic Kerr-medium to a real single photon pulse introduces additional phase noise that prevents a high-fidelity gate operation. This problem could be avoided while at the same time loosening the constraints for the strength of the nonlinearity (no phase-shift of π per photon needed) by using coherent states instead of single photon pulses [101]. The argument given by *Shapiro* [100] does not apply to the results in this thesis as everything presented here was done in a continuous wave measurement with coherent states (measurement time much larger than all dynamics in the system) and a continuous drive leading to an average cavity population of around one single photon, but not a true single photon state.

6.2. Theory
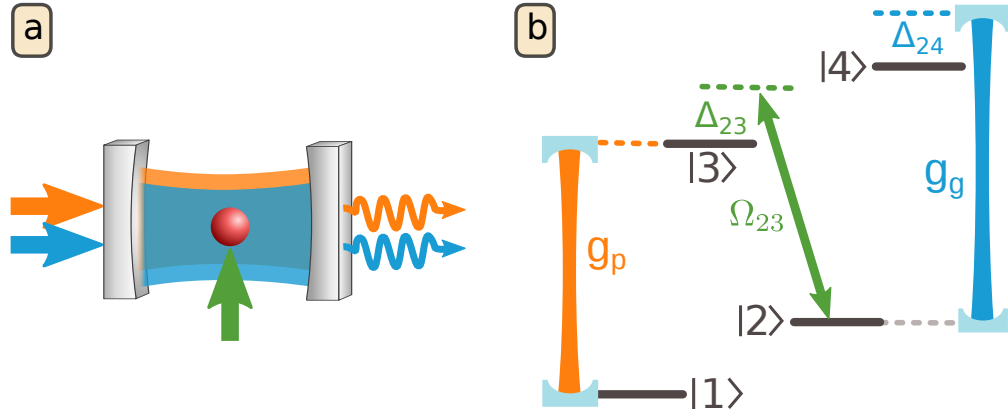
Figure 6.1: (a) shows the driving geometry with two driven cavity fields and an additional laser addressing the atom. (b) shows the effective level scheme with two strongly coupled cavity modes. The orange mode is called probe mode, exhibits a coupling constant of g_p and is resonant to the atomic transition $|1\rangle \leftrightarrow |3\rangle$. The blue mode is called gating mode, has a coupling constant of g_g and has a detuning of Δ_{24} to the atomic $|2\rangle \leftrightarrow |4\rangle$ transition. The two subsystems are coherently coupled by a classical beam with Rabi frequency Ω_{23} and detuning Δ_{23} to the atomic transition $|2\rangle \leftrightarrow |3\rangle$.

The principal level scheme for the experiments in this chapter is shown in Figure 6.1. It is intuitive to break down the derivation of the interaction of both cavity modes in this chapter into two parts. First, the CEIT system on the left of the figure, consisting of atomic states $|1\rangle, |2\rangle, |3\rangle$, the probing cavity mode with coupling constant g_p (shown in orange) and a laser addressing the atom connecting $|2\rangle$ and $|3\rangle$ (shown in green). This system was already discussed in Section 4.

The second part of the system consists of a two level system dispersively coupled to the gating mode. The next section (Section 6.2.1) first considers the theory of a dispersive interaction in a single atom CQED system in general, to give an intuition of the resulting interaction between both systems, that is discussed in the chapter thereafter (Section 6.2.2).

6.2.1. Dispersive interaction in CQED

The subsystem considered here consists of a two-level atom with ground state $|2\rangle$ and excited state $|4\rangle$ which is strongly coupled to the gating cavity mode with coupling constant g_g and detuning to the atomic transition of Δ_{24}. In the dispersive regime, the detuning between atom and cavity is bigger than the coupling constant $\Delta_{24} \gg g_g$. This changes the situation in comparison to a resonant interaction and prevents atomic excitation, as will be discussed later. Starting point for the treatment is the Jaynes-Cummings Hamiltonian as described in Section 2.1. It is helpful to apply the following unitary transformation to

the Hamiltonian:

$$U = exp\left[\frac{g_g}{\Delta_{24}}(\hat{b}\hat{\sigma}_{24}^\dagger - \hat{b}^\dagger\hat{\sigma}_{24})\right] \tag{6.1}$$

with the creation (annihilation) operator of the gating cavity mode $\hat{b}^\dagger(\hat{b})$ and the atomic transition operator σ_{24}. Applying this transformation to the Hamiltonian and an expansion up to the second order in g_g leads to [102]:

$$\begin{aligned}
H' &\approx \left(\omega_{c,g} + \frac{g_g^2}{\Delta_{24}}\hat{\sigma}_{24}^\dagger\hat{\sigma}_{24}\right)\hat{b}^\dagger\hat{b} + \left(\omega_{a,24} + \frac{g_g^2}{\Delta_{24}}\right)\hat{\sigma}_{24}^\dagger\hat{\sigma}_{24} \\
&= \omega_{c,g}\hat{b}^\dagger\hat{b} + \left(\omega_{a,24} + \frac{g_g^2}{\Delta_{24}} + \frac{g_g^2}{\Delta_{24}}\hat{b}^\dagger\hat{b}\right)\hat{\sigma}_{24}^\dagger\hat{\sigma}_{24}
\end{aligned} \tag{6.2}$$

where $\omega_{c,g}$ is the frequency of the gating cavity mode and $\omega_{a,24}$ is the atomic transition frequency between $|2\rangle$ and $|4\rangle$. Two interesting effects can be seen from the form of that Hamiltonian: the cavity frequency experiences an atomic state dependent energy shift by $\hat{\sigma}_{24}^\dagger\hat{\sigma}_{24}g_g^2/\Delta_{24}$ (first line of Equation 6.2). This so-called cavity-pull is not significant here as it stays below the cavity linewidth for experimentally achieved values. Visible in the rewritten Hamiltonian in the second line of Equation 6.2 is that the atomic transition frequency experiences an AC Stark shift of $g_g^2\hat{b}^\dagger\hat{b}/\Delta_{24}$, with the photon number $\hat{b}^\dagger\hat{b} = \hat{n}_g$ in the gating cavity mode. There is one additional term in the Hamiltonian that does not scale with the photon number and therefore poses a constant offset that is not considered for the further treatment. In this dispersive regime, the dressed states are also modified in comparison to the resonant case, here explanatory given for the first manifold:

$$|-,1\rangle \propto |2,1\rangle - \frac{g_g}{\Delta_{24}}|4,0\rangle \tag{6.3}$$

$$|+,1\rangle \propto \frac{g_g}{\Delta_{24}}|2,1\rangle + |4,0\rangle \tag{6.4}$$

This means that for $g_g \ll \Delta_{24}$, one state is more cavity-like and one is more atom-like. As the cavity is driven in this experiment only the state $|-,1\rangle$ is addressed. The decay rate of that state is:

$$\Gamma_{|-,1\rangle} = \left(\frac{g_g}{\Delta_{24}}\right)^2\gamma_4 + \kappa_g \tag{6.5}$$

with the decay rate of the gating cavity of κ_g and the atomic decay rate γ_4. For a large detuning, this is almost identical to the decay rate of the empty cavity.

6.2.2. Effective Hamiltonian

The full Hamiltonian of the system in a rotating frame can be written as [82]:

$$\begin{aligned}
H =& (\Delta_p - \Delta_{23})\hat{\sigma}_{22} + \Delta_p\hat{\sigma}_{33} + (\Delta_p - \Delta_{23} + \Delta_{24})\hat{\sigma}_{44} + \Delta_p\hat{a}^\dagger\hat{a} \\
&+ g_p\hat{\sigma}_{13}\hat{a}^\dagger + g_g\hat{\sigma}_{24}\hat{b}^\dagger + \Omega_{23}\hat{\sigma}_{23}^\dagger + \text{h.c.}
\end{aligned} \tag{6.6}$$

with the photon creation (annihilation) operator $\hat{a}^\dagger(\hat{a})$ of the probing cavity mode (with frequency $\omega_{c,p}$) and the detuning of the driving laser (with frequency $\omega_{l,13}$) to that mode $\Delta_p = \omega_{l,13} - \omega_{c,p}$. Furthermore introduced are the coupling constants of both cavity modes g_p, g_g, the atom cavity detuning of the gating mode Δ_{24}, and the detuning and Rabi frequency of the transverse drive, Δ_{23} and Ω_{23} respectively. The gating cavity is driven resonantly leading to a vanishing detuning and therefore a vanishing cavity energy term in a rotating frame Hamiltonian. The interaction between the transition $|2\rangle \leftrightarrow |4\rangle$ and the gating mode is dispersive, meaning a similar transformation as in the last chapter can be applied to the full Hamiltonian. In the weak driving regime of the probing beam, where $g_p^2 \bar{n}_p \ll \Omega_{23}^2$ applies (with the average intra-cavity photon number in the probing cavity $\bar{n}_p$), the effective interaction Hamiltonian can be written as [103, 104]:

$$H_{eff} \propto \frac{g_p^2 g_g^2}{\Omega_{23}^2 \Delta_{24}} \hat{a}^\dagger \hat{a} \hat{b}^\dagger \hat{b} \tag{6.7}$$

with the creation (annihilation) operator $\hat{b}^\dagger(\hat{b})$ of the gating cavity mode. This quantum version of the classical Kerr Hamiltonian mediates an interaction between the photons in the two cavity fields.

Intuitively this can be explained as stemming from the fact that light in the gating cavity induces a photon number dependent AC Stark shift on the atomic transition frequency between $|2\rangle \leftrightarrow |4\rangle$, which shifts the atomic ground state $|2\rangle$ in energy. The energy shift of this can be read out via the narrow dark state transitions of CEIT, because the two-photon detuning also shifts according to the gating photon number. The shift of the CEIT peak can be seen in the full quantum simulation shown in Figure 6.2(a). Different photon numbers in the gating cavity lead to different shifts of the peak. The width also changes, which will be discussed in Section 6.3.2. The shift of $|2\rangle$ due to photons in the gating mode is dispersive, which means the atomic excitation to state $|4\rangle$ remains low. This makes the measurement non-destructive for the gating photons, except for residual losses due to finite detuning and experimental imperfections such as mirror losses. The gating cavity population for a simulation with and without probing photons is depicted in Figure 6.2(b). The green dashed line is a simulation where the whole atomic population is in $|1\rangle$, as the probe beam is off. This is equal to the fully unperturbed gating cavity population without an atom. With a probe, this slightly changes and is reduced to around 96% of its unperturbed value at the probing frequency of strongest interaction. This can be improved by increasing the detuning Δ_{24} at the cost of a lower shift per gating photon. The simulation shows, that this is indeed a non-destructive measurement for the gating photons. This also expresses itself in the fact that the effective interaction term commutes with the photonic and atomic terms, allowing for a quantum non-demolition measurement (QND) [105].

An important distinction to be made is that of a strong and weak dispersive interaction. In the weak dispersive regime the effective coupling strength of the dispersive interaction is smaller than the biggest relevant decay rate of the system. In the here presented situation, due to the narrow and long-lived dark state of CEIT, the lifetime of photons in the gating
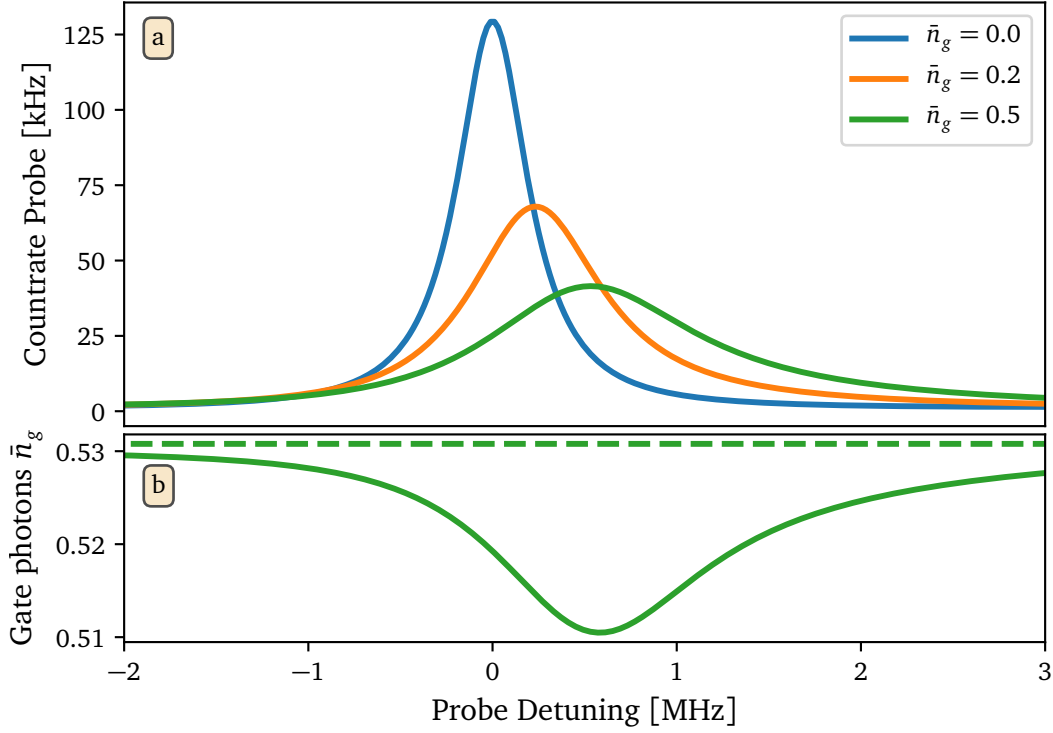
Figure 6.2: (a) shows the simulated countrate of the single photon detectors (SPCMs) as in the real experiment against the detuning of the probe beam for three different values of the gating photon number $\bar{n}_g$. (b) shows the photon number in the gating cavity for the green plot in (a) (indicated by $\bar{n}_g = 0.5$) for the two situation with probing beam (green solid) and without probing beam (green dashed). The simulation incorporates a full quantum model of the system with the parameters: $g_p/2\pi = 10.0\,\text{MHz}, g_g/2\pi = 10.0\,\text{MHz}, \Omega_{23}/2\pi = 3.0\,\text{MHz}, \Delta_{24}/2\pi = 50.0\,\text{MHz}$.

cavity, that decay with κ_g, rather than atomic constraints, set the limit. This means that the photon number in the gating cavity, to be measured via the shift of the EIT resonance, has already changed before the system could even build up the corresponding shift. More accurately, this means the Kerr interaction does not project the system fast enough to collapse the coherent state, that is within the gating cavity, to a photon number state before it decays. Therefore, only the average photon number $\bar{n}_g$ is measurable in the experiment, and therefore, only that is relevant to all further discussions in this chapter. To ensure a constant average gating cavity photon number that mode is continuously driven by a laser in the experiment.

In the strong dispersive regime the projection to a photon number state is faster than all decay constants, and therefore, an initially coherent state in the cavity collapses to a photon number state as beautifully shown in [2]. Spectrally this allows for the observation of well separated peaks corresponding to different photon numbers in a coherent driving field [90]. There is no experiment (at least to the author's best knowledge) that can yet

reach the strong dispersive coupling regime in the optical domain, but an estimate of the feasibility is made in the supplement of [87].

6.2.3. Cross Kerr nonlinearity

Even though it is usually used as a macroscopic quantity in a many body system it is also possible to derive the linear susceptibility of a single atom within a cavity via a semi-classical approach [37, 46, 106] to:

$$\chi^{(1)} = \frac{g_p^2\big(\Delta_p + \Delta_{23} + i\gamma_{deph}\big)}{-(\Delta_p + i\gamma_3)(\Delta_p + \Delta_{23} + i\gamma_{deph}) + \Omega_{23}^2} \tag{6.8}$$

with the two decay constants γ_3 for the excited state decay and γ_{deph} for the dephasing between the ground states. For vanishing probe detuning Δ_p and no dephasing, the linear susceptibility vanishes, as in vacuum, which is a consequence of the CEIT which renders the medium fully transparent. As already mentioned in the previous section, the transition $|2\rangle \leftrightarrow |4\rangle$ is strongly coupled to the second cavity mode (gating cavity) in the dispersive regime, which effectively leads to a photon number dependent AC Stark shift of the energy of state $|2\rangle$. This then changes the detuning Δ_{23} to $\Delta_{23}' = \Delta_{23} + \Delta_{Stark}$. To simplify the equations, but without limiting the generality, it is assumed that $\gamma_{deph} = 0$ and that the initial detuning is $\Delta_{23,0} = 0$. This leads to the new effective susceptibility:

$$\chi_{eff} = \frac{g_p^2(\Delta_p + \Delta_{Stark})}{-(\Delta_p + i\gamma_3)(\Delta_p + \Delta_{Stark}) + \Omega_{23}^2} \tag{6.9}$$

For small Δ_{Stark} (Taylor expansion), and with the expression for the AC Stark shift of state $|2\rangle$ from Section 6.2.1 this results in:

$$\chi_{eff}(\bar{n}_g) = \underbrace{\frac{g_p^2\Delta_p}{-(\Delta_p + i\gamma_3)\Delta_p + \Omega_{23}^2}}_{\chi^{(1)}} + \underbrace{\frac{g_p^2 g_g^2 \Omega_{23}^2}{\Delta_{24}\big(\Omega_{23}^2 - (\Delta_p + i\gamma_3)\Delta_p\big)^2}\bar{n}_g}_{\chi_{cross}} \tag{6.10}$$

where $\bar{n}_g$ is the mean photon number in the gating cavity mode. The second term can readily be identified as an effective $\chi^{(3)}$ nonlinearity, as the system exhibits the well known structure $\chi_{eff} = \chi^{(1)} + \chi^{(3)}|E_g|^2$, where E_g is the electric field of the gate cavity [107] (because $|E_g|^2 \propto \bar{n}_g$). For zero detuning in the probing beam this simplifies to:

$$\chi_{cross}(\bar{n}_g) = \frac{g_p^2 g_g^2 \bar{n}_g}{\Delta_{24}\Omega_{23}^2} \tag{6.11}$$

which is in agreement with the independently derived results in [103, 104, 108], and also confirms the effective Hamiltonian from the previous chapter. In the case of large values of the AC Stark shift ($\Delta_{Stark} \gg \Omega_{23}$) Equation 6.9 becomes:

$$\chi_{cross} = \frac{g_p^2}{-i\gamma_3} \tag{6.12}$$

This means the induced Kerr susceptibility becomes completely imaginary in the limit of high photon numbers, which corresponds to absorption only. A simulation of the χ_{cross} nonlinearity in Equation 6.9 for different gating photon numbers (at $\Delta_p = 0$) is shown in Figure 6.3. It is now possible to relate the index of refraction to the susceptibility
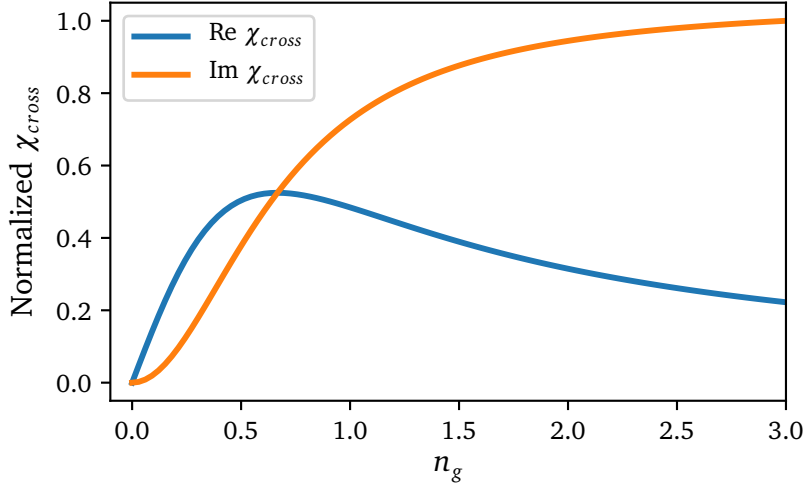
Figure 6.3: Simulation of the cross Kerr coefficient χ_{cross} for different photon number in the gating cavity, normalized to the biggest value within the plotting range. The other parameters are $g_p/2\pi = 10\,\text{MHz}, g_g/2\pi = 10\,\text{MHz}, \Delta_p/2\pi = 0\,\text{MHz}, \Delta_{24}/2\pi = 100\,\text{MHz}, \gamma_4/2\pi = 6\,\text{MHz}, \Omega_{23}/2\pi = 2\,\text{MHz}.$

via the relation $n_{ir}^2 = 1 + \text{Re}\,\chi$ [107], where n_{ir} is the index of refraction and $\text{Re}\,\chi$ the real part of the susceptibility. The optical path length of the probing light, and therefore, the phase shift during passage through the medium, depends on the index of refraction and in consequence on the average number of photons in the gating cavity. This can be understood as a cross Kerr nonlinearity. In the classical self Kerr effect, the intensity of a light beam changes the index of refraction of a medium, and therefore, the phase of that same beam. Here it is a different effect, because the phase of the weak probe beam is modulated by the intensity of the gating beam (here in terms of the photon number $\bar{n}_g$).

6.3. Experimental results

6.3.1. Implementation in a real atom
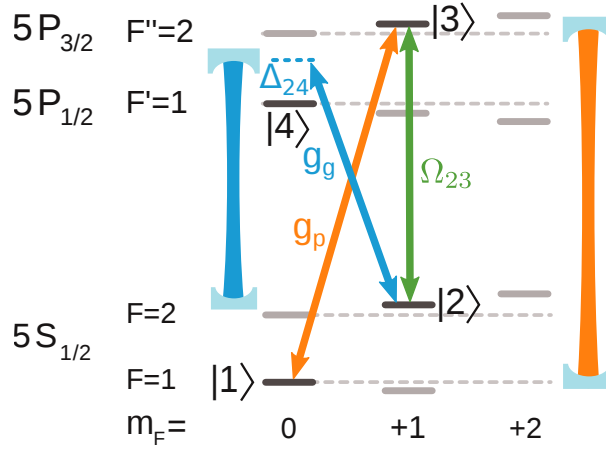
Figure 6.4: Level scheme for the experiments in the dispersive CQED regime. There are two longitudinal cavity modes depicted (orange, blue), that are resonant or close to resonant to two different transitions of the atom. Initially the population is prepared in $|F = 1, m_F = 0\rangle$.

The level scheme used within this chapter is shown in Figure 6.4. Two different longitudinal TEM_{00}-modes of the same physical cavity, one of which is resonant to the D2 line (780 nm) and the other close to resonant to the D1 line (795 nm) of ^{87}Rb. The atomic transitions are strongly coupled to these cavity modes with resonant coupling constants of $g_p/2\pi = 9.4\,\text{MHz}$ and $g_g/2\pi = 7.3\,\text{MHz}$. The mode resonant to the transition from $|5S_{1/2}, F = 1, m_F = 0\rangle$ to $|5P_{3/2}, F'' = 1, m_{F''} = +1\rangle$ is called the probe cavity mode while the mode resonant to the transition from $|5S_{1/2}, F = 2, m_F = +1\rangle$ to $|5P_{1/2}, F' = 1, m_{F'} = 0\rangle$ is called the gate cavity mode.

State preparation

The starting point of the measurement is the ground state $|5S_{1/2}, F = 1, m_F = 0\rangle$. Addressing the atom with two laser fields resonant to the $|F = 2\rangle \leftrightarrow |F'' = 1\rangle$ and $|F = 2\rangle \leftrightarrow |F'' = 2\rangle$ transition in $\sigma^+ + \sigma^-$ polarization depopulates the $|F = 2\rangle$ manifold. In addition a laser resonant to the $|F = 1\rangle \leftrightarrow |F' = 1\rangle$ transition in π-polarization is used, depopulating all states in $|F = 1\rangle$ except $|F = 1, m_F = 0\rangle$, because this state does not couple to that laser, as that transition is dipole forbidden. In effect all population accumulates in the state $|F = 1, m_F = 0\rangle$ with high fidelity. A measurement of the state preparation over time is shown in Figure 6.5. As can be seen, at the beginning the probe and gating cavity modes still emit photons. This is because the $|F = 1\rangle \leftrightarrow |F' = 1\rangle$ laser addresses the excited state of the gating mode and the $|F = 2\rangle \leftrightarrow |F'' = 1\rangle$ laser the excited state of the probing mode. The atom then decays via the cavity mode from the respective excited state, and therefore, scatters photons into that respective mode. This makes emission into these
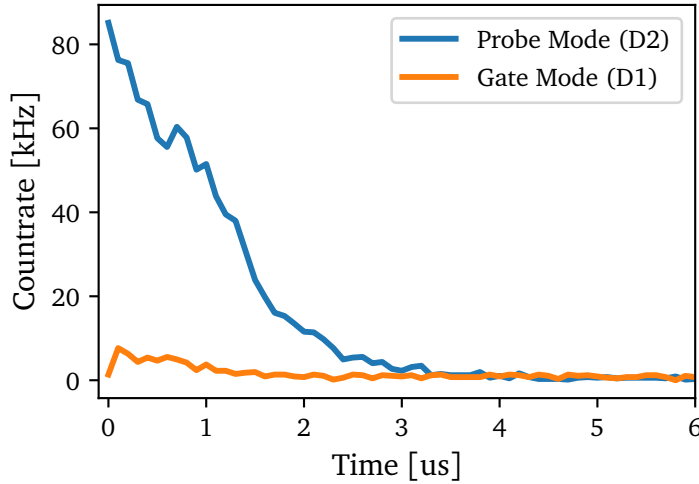
Figure 6.5: Output countrate of different cavity modes over time during state preparation.

modes a good indicator of the state preparation. As can be seen in the measurement, the state preparation is completed after around $4\,\mu s$ with negligibly low countrate afterwards, attesting to a high-fidelity state preparation.

Measure detuning

Starting from the all-resonant situation, where both cavity modes are perfectly resonant to their respective atomic transition, it is possible to tune the atomic transition frequencies via Stark shifts. The energy shift due to the Stark effect scales as I/Δ, with the intensity I of the light field and the detuning to all coupling transitions Δ. As already introduced in the work of [53], the near resonant red detuned dipole trap in the experiment induces a differential Stark shift between the D1 and D2 line transitions, because the frequency of that trap is closer to the D1 line transition ($|5S_1/2\rangle$ to $|5P_1/2\rangle$) than to the D2 line transition ($|5S_1/2\rangle$ to $|5P_3/2\rangle$). This means that the transition frequency of the D1 line is shifted more than that of the D2 line by that laser. When the power of this trap changes, both transition frequencies change. Varying the cavity length until the probe cavity mode is resonant again to the D2 line leaves a certain detuning of the gate mode to the D1 line. With this technique it is possible to tune the gate mode detuning. Reducing the trapping power unfortunately also reduces the ground state trapping potential, leading to a shorter trapping time and reduced trapping probability. To circumvent this, the trap is only ramped down to a lower level during the experiment and ramped back up to a higher value between measurements. To measure the detuning between gating mode and D1 line, a laser interrogates the system transversely and a frequency scan is performed. Photons from the resulting fluorescence spectrum are scattered into the cavity mode. The output of the cavity mode then shows the normal mode spectrum of a strongly coupled system. Tuning the cavity in frequency (via the length), until the normal modes are symmetric, then results in the detuning introduced by the Stark shift.

6.3.2. Sensing of photons
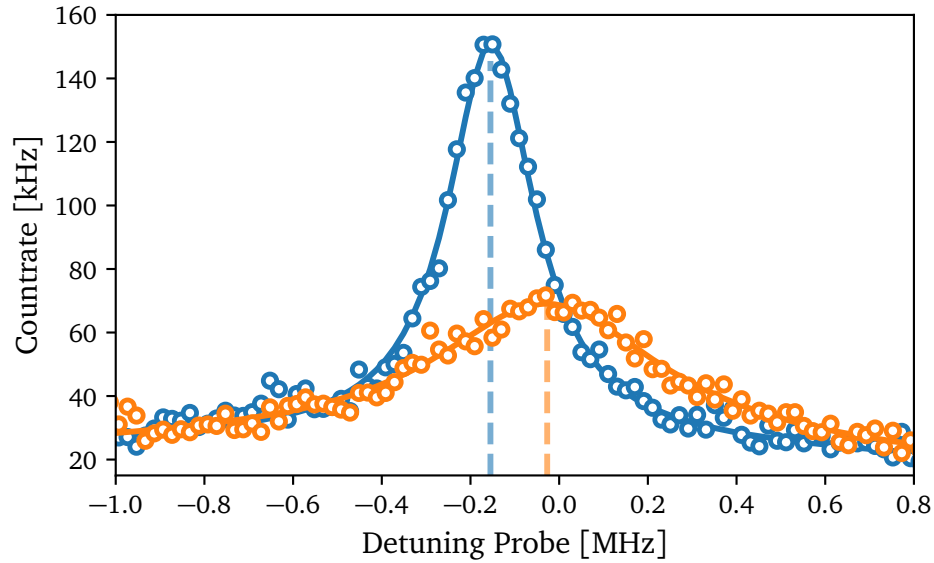
Figure 6.6: The blue curve shows a measurement of the transmitted countrate for different input frequencies, which forms a CEIT spectrum. Shown in the background is a Lorentzian fit to determine the center. The orange curve shows the same scan for an average gate photon number of $\bar{n}_g = 0.5$ in the cavity. The detuning of the gating cavity to the atomic transition was $\Delta_{24} = 23\,\text{MHz}$.

Different methods that try to sense the photon number have become recently available and the research is ongoing [38, 87, 109]. As the theory section already explained, photons in the gating cavity lead to a shift of state $|2\rangle$. As a result, the narrow EIT two-photon resonance shifts in frequency dependent on the photon number in the gating cavity. Figure 6.6 shows the unperturbed EIT spectrum in blue and the spectrum for an average gating photon number of $\bar{n}_g = 0.5$ in orange. Two effects are striking: the center frequency of the Lorentzian resonance peak shifts by 127(5) kHz and the width increases from 108(2) kHz to 313(8) kHz (HWHM). The theory predicts a linear shift of the center frequency of the CEIT peak for different average gating photon numbers $\bar{n}_g$. This is indeed validated by the measurement in Figure 6.7(a), where the peak position is depicted for different gating photon numbers. The blue curve in the background is a linear fit, revealing a shift of $\Delta S_0 = 270(10)\,\text{kHz/ph}$, where /ph means per gating photon. Also the peak width increases with increased gating photon number, which can be see in Figure 6.7(b). This also shows a linear behavior with a slope of $\Delta W_0 = 570(50)\,\text{kHz/ph}$ (HWHM). The width of the peak changes due to quantum fluctuations δn of the photon number of the gating cavity around its average value of $\bar{n}_g$. These in turn lead to fluctuations of the Stark shift and therefore fluctuations in the energy of state $|2\rangle$. This has an influence on the phase between the ground states in the superposition state that constitutes CEIT $\left(\text{e.g. } |\Psi_1^0\rangle \propto |1,1\rangle - |2,0\rangle\right)$. In the weak dispersive regime, in which this experiment
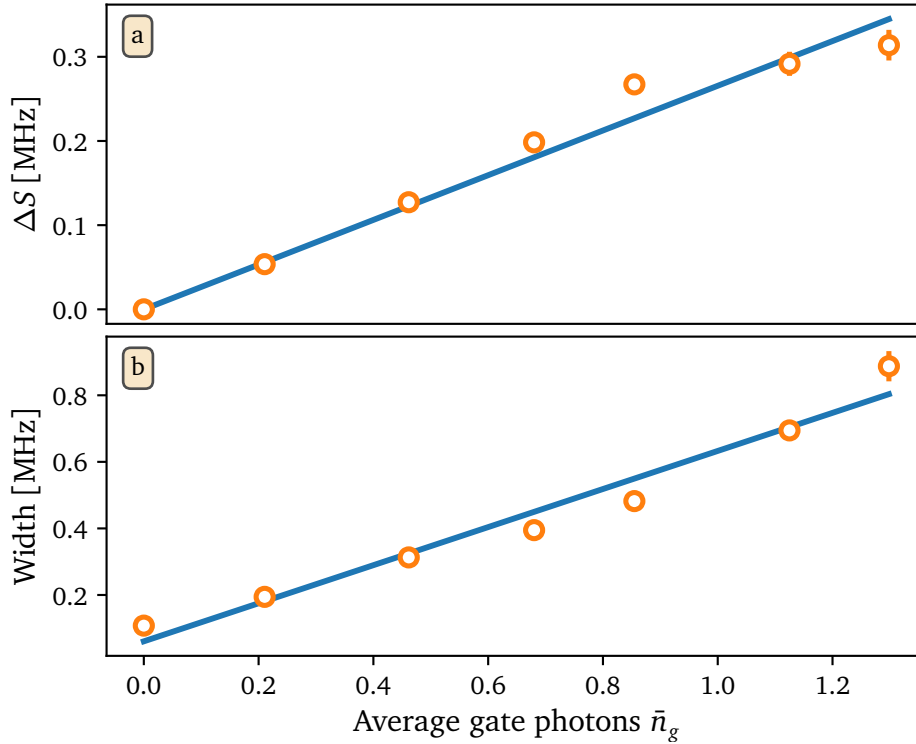
Figure 6.7: Shift (a) and width (b) of the CEIT peak for different gating photon numbers. The detuning of the gating cavity to the atomic transition was $\Delta_{24} = 23\,\text{MHz}$.

operates, the projection onto a photon number state due to the Stark shift is slower than the timescale of these fluctuations in the gating photon number. The system therefore stays in a coherent state and is not projected, as it cannot follow the instantaneous photon number fast enough. As was shown in several theoretical treatments of similar systems [102, 110], for a low gating photon number, this effectively leads to a randomization of the phase between the ground states (dephasing) that is proportional to the number of transmitted photons through the gating cavity. This can be viewed as a measurement induced dephasing per transmitted photon. In the presented experiment, the gating cavity is constantly driven to keep $\bar{n}_g$ constant although the cavity population decays with a rate of κ_g. This leads to a photon transmission rate proportional to $\kappa_g \cdot \bar{n}_g$ and with it a corresponding dephasing rate. Spectrally, this results in a broadening of the CEIT peak due to ground state dephasing, that is linear in the average gating photon number $\bar{n}_g$. The linear scaling for low gating photon numbers has been also experimentally shown in similar experiments in the microwave regime [89].

Tuning the sensitivity

Experimentally, the coupling strength g varies with the position of the atom within the cavity. Figure 6.8 shows a sketch explaining this behavior. Atoms can only be trapped at the
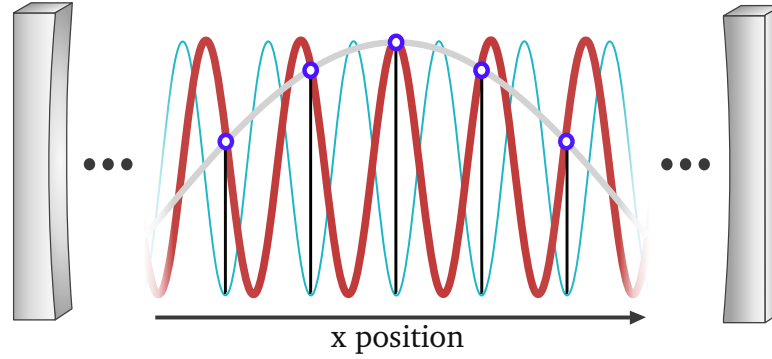
Figure 6.8: A sketch of the cavity and the relevant cavity fields. Shown in bright blue is the intra-cavity field intensity. Atoms are only trapped at the field minima. The red line depicts the field that is resonant to the atomic transition. The blue dots show the field strength of the resonant field at the trapping positions that are given by the minimum of the intra-cavity field. The gray line connecting the blue dots is a guide to the eye, to allow for easy visualizing of the change of the coupling constant over position.

minima of the field intensity of the blue detuned intra-cavity trap (around 772 nm). There are two different longitudinal modes of the cavity as already mentioned, each strongly coupled to a different D-line of ^{87}Rb (around 780 nm for the D2 line and 795 nm for the D1-line). The standing wave trapping light field and the light fields of the two strongly coupled modes dephase with position along the cavity axis due to their wavelength mismatch. This leads to different values of the coupling strength $g_{D1} \simeq g_g$ and $g_{D2} \simeq g_p$ at different trapping positions within the cavity. Due to the exact determination of the position with the imaging system, it is possible to postselect on atoms at a specific position and determine the coupling constant there by normal mode spectroscopy as already shown in [53]. An exemplary normal mode spectrum for the gating cavity (in the resonant case for $\Delta_{24} \approx 0$) is shown in Figure 6.9(a) for one specific postselection. The normal modes are slightly asymmetric due to residual detuning of Δ_{24}. In the background (blue) is a semi-classical theory [17, 111] that can be derived via the Heisenberg equations of motion of the system, modified by accounting for the atomic motion within the trap [112]. Scanning the atom postselection along the cavity direction and determining the corresponding coupling strength leads to Figure 6.9(b). The orange data points show a good agreement with the underlying theoretical curve (from a simple theory considering the coupling constant at each trapping site). The step-like behavior of the theory curve is due to the fact, that there are only discrete points at which an atom can be trapped. The coupling constant on the D1-line g_{D1} can be tuned from 10.3 MHz (the used transition was $|5S_{1/2}, F = 2, m_F = +2\rangle$ to $|5P_{1/2}, F' = 1, m_{F'} = +1\rangle$) to around 2 MHz. Over the same position range, the D2-line coupling constant g_{D2}, that is shown as a theoretical curve in the background of the figure (gray), stays above 90% of its peak value. This difference in the dephasing position range is due to the lower frequency difference of the D2-line to the intra-cavity trap. This allows for postselection on different coupling strengths with

respect to each other. The ability to tune the coupling strength of the gating cavity (D1) is
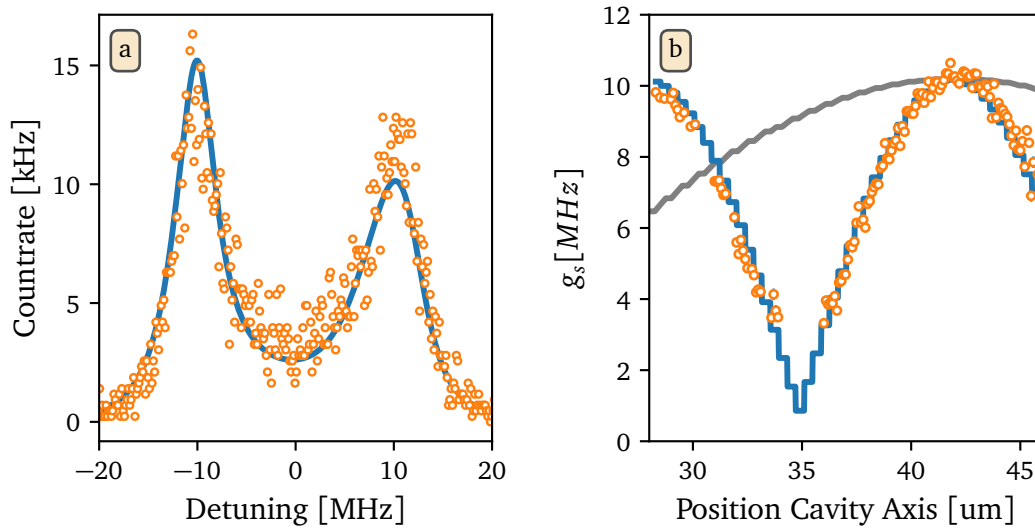
Figure 6.9: (a) shows the countrate of the cavity output (orange) for the atom driven spectrum with a postselection of $x \in [42.25, 42.75]$. The coupling constant deduced from the semi-classical fit (blue) is $g_g/2\pi = 10.3\,\text{MHz}$. (b) shows the deduced coupling constants for different positions within the cavity (orange) with the theoretical behavior in the background (blue) as calculated from a classical theory considering the discrete trapping positions and the dephasing between both. For comparison, the theoretical D2 coupling constant (maximum constant chosen to be the same as D1) is depicted in gray. The theory curve is adjusted in position and amplitude to fit the data. This measurement was done on a transition with a higher coupling constant than in the final experiment, namely on the $|5S_{1/2}, F = 2, m_F = +2\rangle$ to $|5P_{1/2}, F' = 1, m_{F'} = +1\rangle$ transition.

crucial for tuning the sensitivity of the photon sensing mechanism. As already mentioned in the theory part, the shift of the ground state $|2\rangle$ depends quadratically on the coupling strength. Figure 6.10(a) shows a measurement for the shift for $\bar{n}_g = 0.6$ at different positions of the atom within the cavity. The shift varies between almost no shift to close to 200 kHz. Combining this with the known coupling constant at different positions from the measurement in Figure 6.9(b) (corrected for the different Clebsch-Gordon coefficient in the dispersive measurement), it is possible to measure the dependence of the shift on the coupling strength. The result is depicted in Figure 6.10(b) and shows the expected quadratic behavior, therefore confirming the theory.

In summary, the strength, and therefore, the sensitivity can be chosen via postselection of the position, which allows for a high dynamic range of photon sensing.
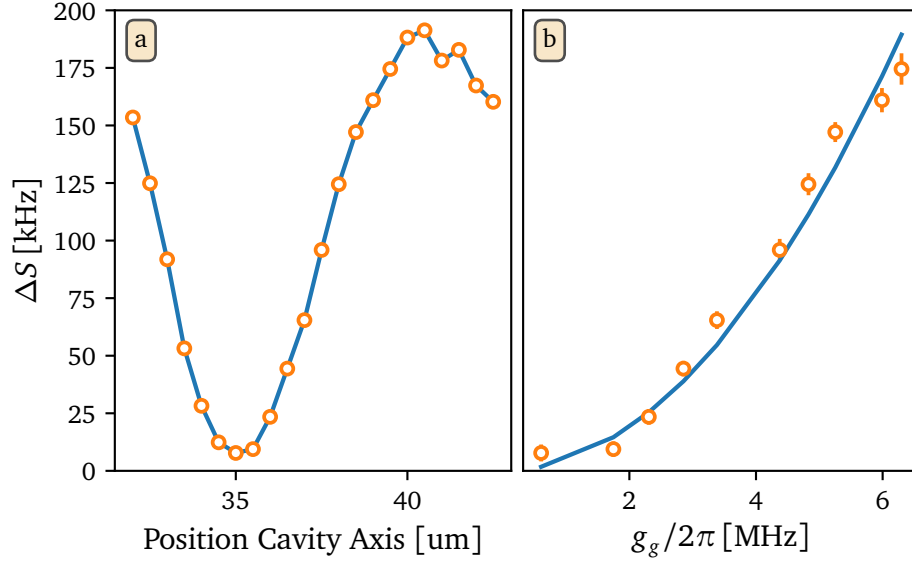
Figure 6.10: Shows the shift of the CEIT peak against the postselection position along the cavity axis (a) and against the coupling strength (b) that varies with the position. In (a) the blue line is just a guide to the eye, in (b) it is a fit of a quadratic function. The gating photon number was $\bar{n}_g = 0.6$ for this measurement.

6.3.3. Cross Kerr effect and determination of $\chi^{(3)}$

It is possible to reconstruct the complex susceptibility χ of a system from a transmission spectrum, like in Figure 6.6, by identifying the imaginary part $\text{Im}(\chi)$ as proportional to the absorption in a medium[1]. The real part $Re(\chi)$ is related to the index of refraction [37, 107]. Quantitatively, this can be expressed as:

$$A(\Delta_p) = 1 - T(\Delta_p) = \text{Im}\,\chi(\Delta_p) \tag{6.13}$$

where A denotes the absorption and T the transmission. The real part of the susceptibility can be calculated via a Kramers-Kronig relation. These mathematical relations state that the imaginary part of any complex function that is analytic in the upper half of the complex plane, can be calculated from the real part and vice versa. The analyticity condition is fulfilled in many physical systems, as it usually follows from causal response for a stable system to an external impulse force, in this case, the driving field. The real part is then given by:

$$\text{Re}\,\chi(\Delta_p) = \frac{1}{\pi} \int\limits_{-\infty}^{\infty} \frac{\text{Im}\,\chi(\omega)}{\omega - \Delta_p} d\omega \tag{6.14}$$

---

[1] in general only true for the linear susceptibility, but it is also valid here, as the $\chi^{(3)}$-term in the polarizability is still only linear in $E_p(\omega)$

Solving this integral requires special care at the pole where $\omega = \Delta_p$ but can be solved with standard numerical methods [113]. The index of refraction can then be calculated via:

$$n_{ir}(\Delta_p) = \sqrt{1 + \text{Re}\,\chi(\Delta_p)} \qquad (6.15)$$

Figure 6.11(a) shows reconstructed dispersion relations for measurements with different gating photon numbers. The curves are reconstructed from real measurements of
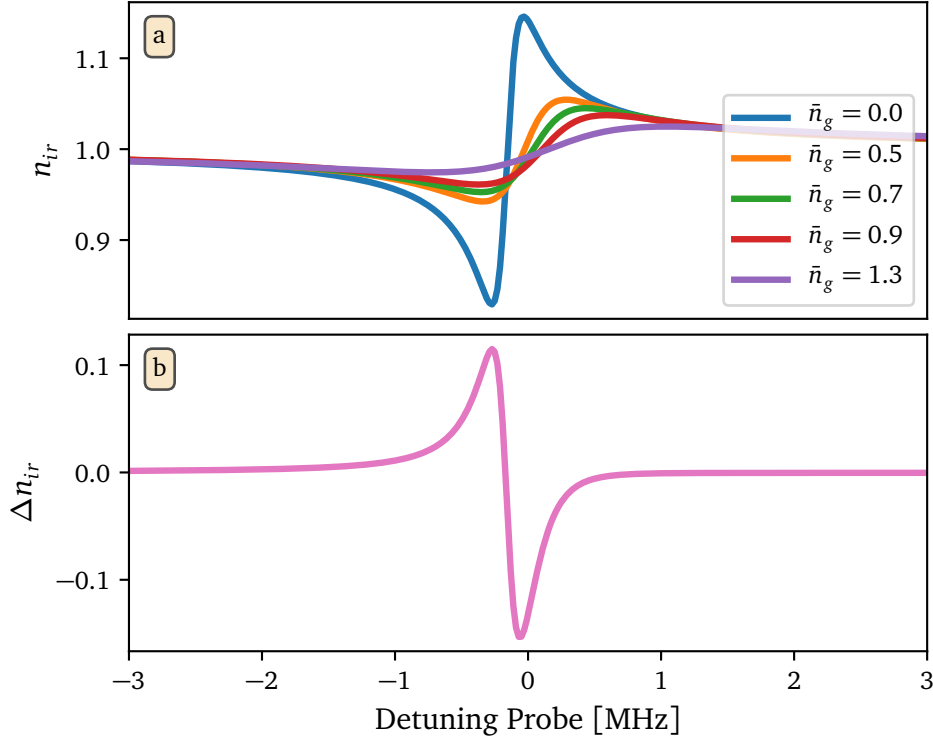
Figure 6.11: (a) shows the index of refraction that is reconstructed from the data against the detuning for different gating photon numbers. (b) shows the difference in the refractive index $\Delta n_{ir} = n_{ir}(\bar{n}_g = 0.5) - n_{ir}(\bar{n}_g = 0)$ as a function of the detuning.

transmission spectra with the aforementioned method. The change in the refractive index is especially steep without any gating photons, where the linewidth of the EIT resonance is only limited by the ground state dephasing γ_{deph} and the Rabi frequency Ω_{23}. Figure 6.11(b) shows the shift in the refractive index for different probing frequencies for $\bar{n}_g = 0.5$ gating photons on average. The difference is as large as $\Delta n_{ir} = 0.15$, leading to a nonlinear refractive index change of $\Delta n_{cross,ph} = 0.3/\text{ph}$. According to [107] the total refractive index is given by:

$$n = n_0 + 2n_{cross}|E_g|^2 \qquad (6.16)$$

with the gating field amplitude E_g. The electric field per photon within the cavity can be calculated via the coupling constant g_g to:

$$E_g(\bar{n}_g) = \frac{\hbar 2 g_g \sqrt{\bar{n}_g}}{d} \tag{6.17}$$

with the dipole moment d of the $|F = 2, m_F = 1\rangle$ to $|F' = 1, m_{F'} = 0\rangle$ transition which equals $d = 1.27 \cdot 10^{-29}$ Cm [54]. Inserting this into Equation 6.16 leads to:

$$n = n_0 + 2 n_{cross} \left(\frac{\hbar 2 g_g}{d} \right)^2 \bar{n}_g \tag{6.18}$$

Comparing the slope of this linear relation to the experimentally determined slope of $\Delta n_{cross,ph} = 0.3/\text{ph}$, the nonlinear refractive index can be deduced to $n_{cross} = 2.6 \cdot 10^{-7} \frac{\text{m}^2}{\text{V}^2}$. From this the χ_{cross} value can be deduced via [114]:

$$\chi^{(3)} \stackrel{\wedge}{=} \chi_{cross} = n_{cross} n_0 / 3 = 8.6 \cdot 10^{-8} \frac{\text{m}^2}{\text{V}^2} \tag{6.19}$$

This is a remarkably large value for a third order susceptibility, which is around 10 orders of magnitude bigger than in nonlinear crystals [107] and comparable with values achieved in ultracold atomic clouds [27]. In contrast to the atomic cloud experiments, this value is achieved here with only one single atom.

6.3.4. Cross phase modulation

The change in the effective refractive index of the medium leads to a different optical path length for the transmission of the probe beam depending on the photon number in the gating cavity mode. To measure this effect directly, it is necessary to implement a detection method that is capable of phase determination. For that purpose, a heterodyne detection setup was build and implemented, the specifics of which are discussed in Section 3.5. This allowed for determination of the phase and the amplitude of the transmitted probe field. These two quadratures are shown in Figure 6.12 over a scan of the probe detuning. The bright states of CEIT are visible in the amplitude at $\Delta_p \approx E_n^\pm \approx \pm 9.4\,\text{MHz}$ and the EIT peak is visible at vanishing two-photon detuning $\Delta_p = \Delta_{23} = 0$. The corresponding phase measurement reveals that each of the three resonances comes with a certain phase shift, as expected from a classical theory of a driven harmonic oscillator. However only all three resonances together lead to the expected phase shift from $-\pi/2$ to $\pi/2$. Remarkable is the steep phase increase in the center corresponding to the EIT transmission window. This is flanked by descending phase on both sides, which resemble anti-resonances as discussed in [115]. This behavior was already expected from the refractive index measurement in Figure 6.11 because the refractive index, and therefore, the optical path length changes rapidly over the EIT window. As already shown, the EIT window for the probing beam can be controlled via the gating photon number, which in turn also tunes the refractive index, and therefore, the phase of the probe. Figure 6.13 shows the amplitude (a) and phase (b)
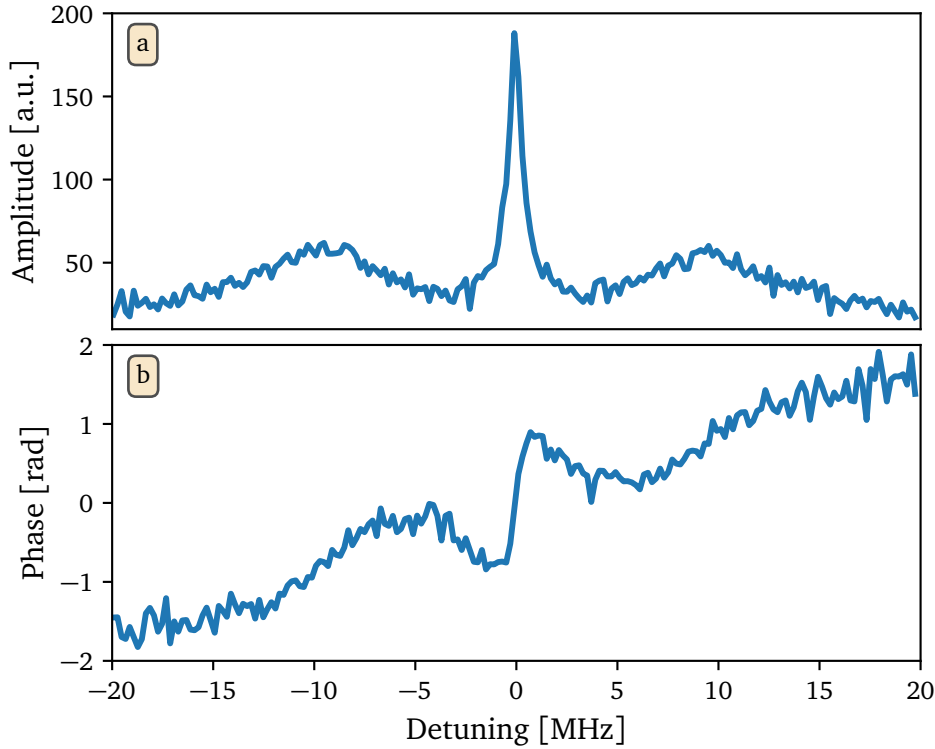
Figure 6.12: Shown are the amplitude (a) and phase (b) of the output probe light over the frequency of the input probe field as measured via the heterodyne setup.

of the EIT window for $\bar{n}_g = 0.0$ (blue dots) and $\bar{n}_g = 0.85$ (orange) photons in the gating cavity. As can be seen, the peak position of the EIT window changes, as does its width, which is in agreement with the intensity measurements in a previous chapter. This also leads to a shift in the phase of the probing beam as predicted from the index of refraction measurements. Figure part (c) shows the actual figure of merit in this chapter, the change in the phase introduced by the gating photons. The difference is measured to be as big as $|\Delta\Phi| = 0.61(8)$ rad at $\Delta_p = -0.35$. However, if the highest transmission of 32(2)% of the empty cavity transmission is aimed for, $\Delta_p = 0.15$ MHz is a more suitable point, with a phase-shift of $|\Delta\Phi| = 0.37(7)$ rad. This point is indicated in the plot by a gray line and is also interesting because the amplitude does not change there, with or without gating photons. Returning to the dispersion curves in Figure 6.11(a), another interesting feature is striking. The dispersion relation flattens and shifts for increased gate photon number, reflecting the already discussed shifting and broadening of the EIT resonance condition. This also directly shows that χ_{cross} is only linear for small gating photon numbers $\bar{n}_g$, and reaches a peak for higher photon numbers, as discussed in the theory section (see also Figure 6.3). This can also be observed in a direct measurement, which is shown in Figure 6.14. The figure shows the shift of the probe phase for one specific probe detuning $\Delta_p = 0.2$ MHz, for different gate photon numbers $\bar{n}_g$. For low gate photon numbers this indeed shows a linear behavior (up to $\bar{n}_g \approx 0.4$) but saturates for higher average gating
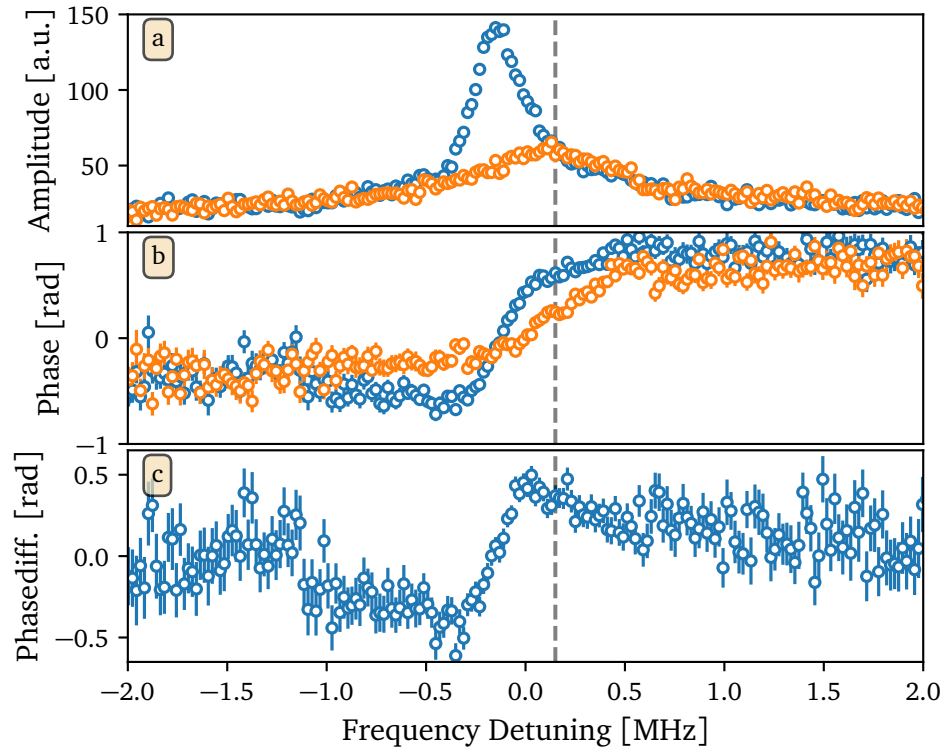
Figure 6.13: Amplitude (a), phase (b) and phase difference (c) of the probing field over frequency for $\bar{n}_g = 0.0$ (blue) and $\bar{n}_g = 0.85$ gate photons in the cavity (orange).
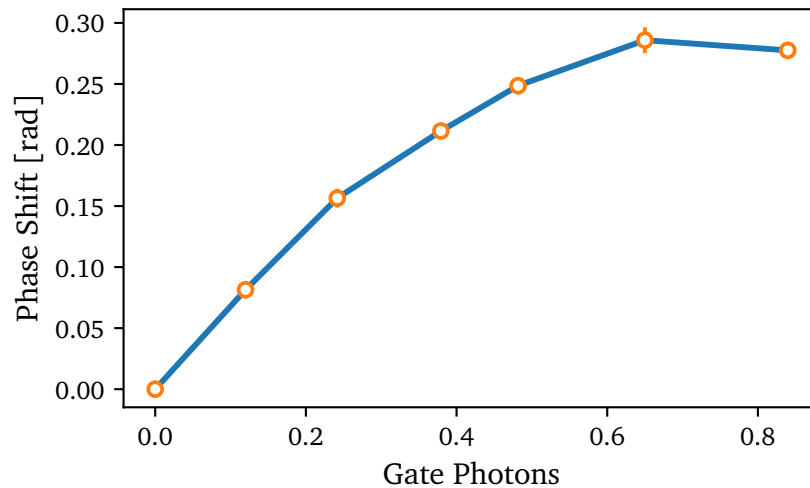
Figure 6.14: Phase shift between the situation with and without the respective gate photon number for one specific detuning of the probe beam of $\Delta_p = 0.2\,\text{MHz}$. The line connecting the dots is a guide to the eye, and does not reflect the theory. The detuning of the D1 line to the cavity was $\Delta_{24} = 26\,\text{MHz}$.

photon numbers, because the susceptibility becomes mostly imaginary and the phase shift would eventually even goes down, when the probe frequency is not within the increasingly shifted EIT window anymore.

6.4. Summary

This chapter of the thesis has shown that the CEIT system, extended by another strongly coupled transition to a different cavity mode (gating mode), can provide a huge $\chi^{(3)}_{cross}$ nonlinearity, very much in the spirit of experiments imagined long ago [84, 96]. The imaginary part of this substantial nonlinear susceptibility is proportional to the transmission of the probe beam, an effect that was used to sense the average number of photons within the gating cavity mode. This measurement showed a remarkable AC Stark shift per single photon. The sensitivity of this method can be tuned via postselection on different coupling constants of the atoms within the cavity, allowing for a high dynamic range in which photons could be sensed. Furthermore, the real part of the nonlinear susceptibility is related to the index of refraction of the medium, and therefore, the optical path length. A variation in the path length leads to a phase shift in the probe beam by photons in the gating cavity, a so called cross-phase modulation. The effect shown here was as big as 41(5)° per gate photon (for a low gate photon number). This surpasses e.g. recent experiments also aiming towards a continuous dispersive Kerr nonlinearity by using resonant Rydberg EIT by around three orders of magnitude [116] and is on par with experiments in atomic clouds [95, 117]. On a different note, the presented system can be easily extended to a completely closed two-cavity-mode atomic cycle with many interesting applications, which are discussed in Section 7.

7. Outlook

The experiment with two cavity modes as described in Section 6 operates in the weak dispersive regime, where the measurement of the photon number is slower than the decay, limiting the possibilities to use this system for analysis of photon statistics or sensing of a specific photon number. This can be overcome by prolonging the dwell time of photons in the gating cavity, which can be achieved by increasing the finesse of the cavity and therefore reduce κ_g, while maintaining a small mode volume. Figure 7.1 shows a simulation of a cavity with similar parameters as used in the current experiment but a κ_g that is 100 times smaller. Part (a) shows that a coherent drive in the gating
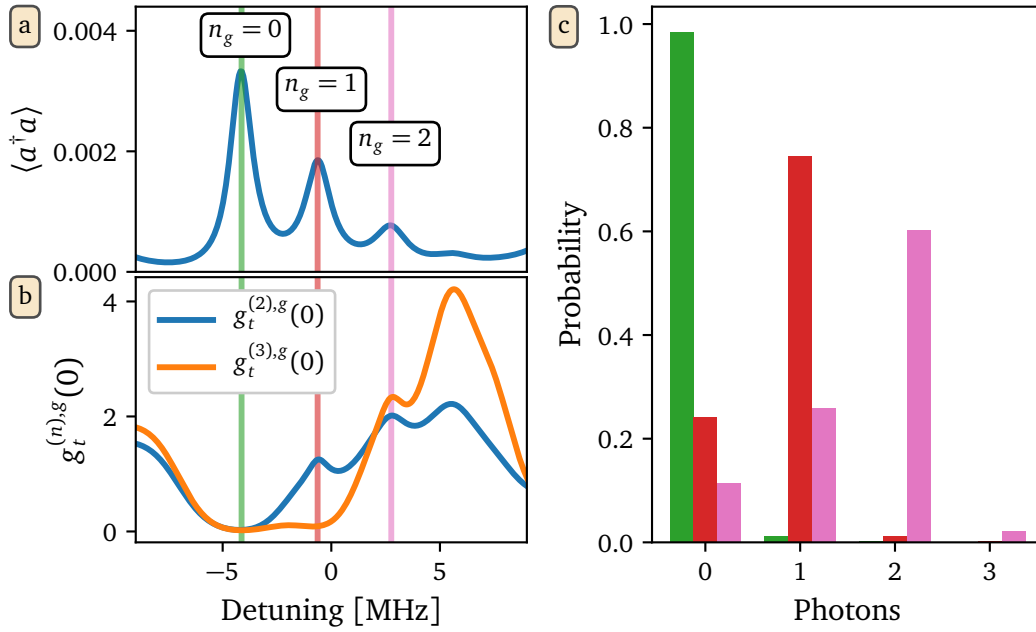
Figure 7.1: (a) shows the probing cavity population against detuning of the probe beam. (b) shows different orders of the triggered (triggered on a probe photon) equal time-correlation function of the gating field. (c) shows the photon distribution of the gating field after a click in the probe field was detected for different probe frequencies, marked in according colors in part (a) and (b). The simulation parameters for the probing cavity are similar to the experimental ones and only the parameters for the gating cavity are changed considerably to $g_g/2\pi = 20\,\text{MHz}, \Delta_{24}/2\pi = 80\,\text{MHz}, \kappa_g/2\pi = 20\,\text{kHz}$. The gating cavity is driven with a coherent drive leading to an average photon number of around one.

cavity indeed is projected into a photon number state, that can then be clearly resolved in a spectrum of the probing beam. Part (b) shows the triggered (heralded) equal-time n-photon correlation function of the gating field $g_t^{(n),g}(0)$. This function is proportional to the probability to have n photons in the gating cavity after one probe photon was detected at the same time. When the probe frequency is tuned to one of the peaks corresponding

to a specific photon number, a detected probe photon then heralds the presence of n_g gating photons. This can also be seen in part (c), where the photon distribution in the gating cavity is shown for different probing frequencies (color corresponding to part (a) and (b)) and detection of a probe photon. The pureness degrades for higher values of n_g but can be improved for better parameters. This technique allows for building a heralded N-photon source, a goal long envisioned in quantum information processing. As it is challenging to support two, close to atomic resonance, longitudinal modes in a cavity, a crossed cavity setup with independent cavities, where only the gating cavity has this extremely low κ would be beneficial. Constructing such a cavity seems realistic, considering that there are cavities in usage that are only a factor of 10 larger in κ than the simulation, while still having a coupling constant of almost $g/2\pi = 20\,\mathrm{MHz}$ [118]. As a summary, with the presented technique, resolving photon number states and constructing heralded N-photon sources in the optical domain seems within reach.

From that point onward, it is interesting to go further into the direction of a completely closed atomic cycle with multiple cavity coupled light fields as already mentioned in the introduction. In general, nontrivial cycles in atoms are a very promising and engaging topic, that is well worth pursuing. Extending the already introduced system with two cavity modes from Section 6 by adding an additional laser as shown in Figure 7.2 (only the left or right half), closes this system.
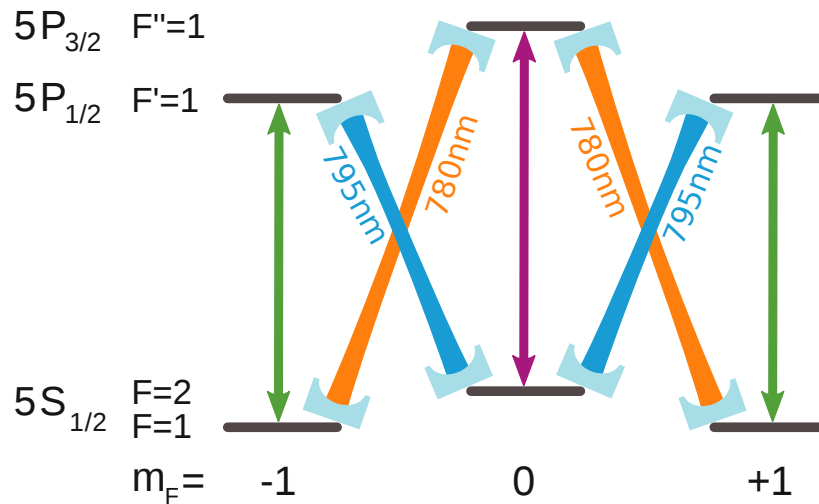
Figure 7.2: Simplified level scheme for the closed cycles system with four different cavity modes and two classical external driving fields.

This leads to two interconnected Λ-systems, a so called double Λ-system, where two external driving fields continuously produce photons in two-cavity modes. These photons will have a strong temporal (and polarization) correlation. Furthermore, this system could also exhibit a dark state ladder as introduced in Section 5, that prevents atomic excitation, enabling the system to continuously produce photons. First experiments were performed that strongly indicate these two effects and are discussed briefly in Appendix Appendix C. Additionally if the transitions are driven equally strongly and the cavity modes exhibit equal coupling strengths, this system does not have a preferred cycling

direction. As a consequence, it could run in both directions, and potentially even in superposition states of these.

Using the other polarization modes that the cavity supports as well, would turn the system into a continuous and bright source of polarization entangled photon pairs of different wavelength. This situation is depicted in Figure 7.2 if one considers now the full scheme shown. First simulations on this system were already performed and the results are promising. A state tomography setup is already under construction which allows for characterization of the entangled photon pairs experimentally.

One line of investigation is real-time observation of the internal degrees of freedom of one atom in a cavity [119, 120]. This becomes especially interesting in the context of closed atomic cycles, where one or more arms of the cycle are driven by cavity modes [121]. A closed cycle in the electronic degrees of freedom of an atom in such a system can show similar physics to atomic currents in quantum many-body systems in optical lattices. These systems then potentially allow for the simulation of Hubbard-type-Hamiltonians or investigations of synthetic gauge fields.

In another line of future research, closed atomic cycles could be promising for the realization of new types of heat engines [122–124]. In contrast to the classical cycle running in a macroscopic heat engine, here the cycle is realized in the internal degrees of freedom of one atom. The quantized nature of the transitions therein, then bring this system to the regime of quantum heat engines, which are especially interesting when one or more atomic transitions are coupled to cavity modes. The cavity modes can then act as non-classical heat reservoirs, as they allow for precise engineering of the light field.

Furthermore research with two independent particles in one cavity, whose internal and external (position) degrees of freedom are well controlled, shows great prospects. Recently, first experiments in that field were presented [112, 118, 125] that show collective effects of both particles that depend on the exact distance and position of each of the particles. In the field of CEIT two-particle effects are also very interesting to investigate. One atom could e.g. be used to precisely engineer the light field for the second atom, when both atoms are separated enough to be individually addressable with laser beams. This is especially interesting in the context of multiple strongly coupled cavity modes as presented in Section 6 of this thesis. There, precise control of the position of each atom would allow for tuning of the coupling constants individually. Additionally, first theoretical considerations have revealed that a second atom could potentially extend the Zeno-blockade mentioned in Section 5 to the second rung of the dark state ladder. This would e.g. allow the system to act as a two-photon source, because higher rungs are very efficiently suppressed. All these examples would benefit greatly from active position control of the particles. This is possible with optical tweezers, a technique where an intense laser beam traps a single particle in its focus and moves that particle to the desired location, even with single site resolution in an optical lattice [126, 127].

Appendices

A. Closed cycle

A.1. Derivation of the effective Hamiltonians

The level scheme of Figure 5.1 is the basis for the following derivation. For this derivations it assumed that $g, \Omega_{12}, \Omega_{23} \in \mathbb{R}$. The derivation follows [81]. The Hamiltonian of this system in the interaction picture is ($\hbar = 1$):

$$H = \underbrace{g\hat{a}\hat{\sigma}_{31} + \Omega_{23}\hat{\sigma}_{32}}_{H_0} + \underbrace{\Omega_{12}\hat{\sigma}_{21}}_{V} + \text{h.c.} \tag{A.1}$$

where $\hat{a}$ is the annihilation operator of the cavity mode and $\hat{\sigma}_{kl} = |k\rangle\langle l|$ ($k, l = 1, 2, 3$) are the atomic transition operators.

Expressing the Hamiltonian in the basis $\{|+\rangle, |-\rangle\}$, with $|\pm\rangle = 1/\sqrt{2}(|1\rangle \pm |2\rangle)$, leads to:

$$H = \frac{1}{\sqrt{2}}\left[(g\hat{a} + \Omega_{23})\hat{\sigma}_{3+} + (g\hat{a} - \Omega_{23})\hat{\sigma}_{3-} + \text{h.c.}\right] + \Omega_{12}(\hat{\sigma}_{++} - \hat{\sigma}_{--}). \tag{A.2}$$

From that point it is possible to derive the effective Hamiltonian for two different regimes of our system:

Weak ground state coupling

For $\Omega_{12} \ll g$ we can treat the coupling field as a perturbation V. The eigenstates of the unperturbed Hamiltonian H_0 [41] are:

$$\left|\Psi_n^0\right\rangle = N_n^0\left[|1, n\rangle - \frac{g\sqrt{n}}{\Omega_{23}}|2, n-1\rangle\right] \tag{A.3}$$

$$\left|\Psi_n^\pm\right\rangle = N_n^\pm\left[|1, n\rangle + \frac{\Omega_{23}}{g\sqrt{n}}|2, n-1\rangle \pm \frac{E_n}{g\sqrt{n}}|3, n-1\rangle\right] \tag{A.4}$$

with the normalization factors $N_n^{(0)} = \Omega_{23}\left(\Omega_{23}^2 + g^2 n\right)^{-1/2}$ and $N_n^\pm = g\sqrt{n}\left(2g^2 n + 2\Omega_{23}^2\right)^{-1/2}$ and the energies $E_n = \sqrt{ng^2 + \Omega_{23}^2}$. Rewriting V in terms of these eigenstates and applying a unitary transformation of the form $U_0 = \exp(-iH_0 t)$, the resulting transformed Hamiltonian contains non-oscillating and fast oscillating terms:

$$V(t) = U_0^\dagger V \mathbb{1} U_0 = U_0^\dagger V\left(\sum_{n=0}^\infty |n\rangle\langle n|\right)U_0$$

$$= \left(\Omega_{12}\sum_{n=0}^\infty \frac{g\sqrt{n+1}}{E_{n+1}}\frac{\Omega_{23}}{E_n}\left|\Psi_{n+1}^0\right\rangle\left\langle\Psi_n^0\right| + \text{h.c}\right) + H_{\text{oscillating}}(t) \tag{A.5}$$

The terms summarized in $H_{\text{oscillating}}(t)$ describe transitions between bright and dark states or between different bright states. Therefore these terms oscillate fast in the limit of strong atom-field coupling ($g \gg \Omega_{12}$) and can be neglected in a rotating wave approximation (RWA). The new effective Hamiltonian is then:

$$V_{eff} \overset{RWA}{\simeq} \Omega_{12} \sum_{n=0}^{\infty} \frac{g\sqrt{n+1}}{E_{n+1}} \frac{\Omega_{23}}{E_n} \left|\Psi_{n+1}^0\right\rangle\left\langle\Psi_n^0\right| + h.c. \tag{A.6}$$

That means the effective driving strength from rung n to rung $n+1$ is given by:

$$\Omega_{n+1} = \frac{\Omega_{12}\Omega_{23}g\sqrt{n+1}}{\sqrt{g^2(n+1)+\Omega_{23}^2}\sqrt{g^2n+\Omega_{23}^2}}. \tag{A.7}$$

This effective driving strength shows the interesting phenomena, that the effective driving first increases with Ω_{23} but goes down for higher values. This is because the ground state coupling beam effectively only drives the transition between atomic ground states with the same cavity photon number ($|1,n\rangle \leftrightarrow |2,n\rangle$), which is a part of the dark state transition $|\Psi_n^0\rangle \leftrightarrow |\Psi_{n+1}^0\rangle$). This transition exhibits the highest transition probability if the population is evenly distributed between both ground states. The population in atomic state $|1\rangle$ scales linear with Ω_{23}, whereas the population in atomic state $|2\rangle$ scales with g. The highest effective driving strength is therefore reached when Ω_{23} and g are of comparable size.

In the regime $g \gg \Omega_{23}$ Equation A.6 can be further simplified to:

$$V_{eff} \simeq -\Omega_{12}\left|\Psi_1^0\right\rangle\left\langle\Psi_0^0\right| - \Omega_{12}\sum_{n=1}^{\infty} \frac{\Omega_{23}}{g\sqrt{n}}\left|\Psi_{n+1}^0\right\rangle\left\langle\Psi_n^0\right| + h.c., \tag{A.8}$$

Strong ground state coupling

First a unitary transformation of the form $U_1 = \exp\left[-i\Omega_{12}t\left(\hat{\sigma}_{++} - \hat{\sigma}_{--}\right)\right]$ is applied to the Hamiltonian of Equation A.2, which leads to:

$$H_1(t) = U_1^\dagger H U_1 - V = \frac{1}{\sqrt{2}}\left[(g\hat{a} + \Omega_{23})\hat{\sigma}_{3+}e^{-i\Omega_{12}t} + (g\hat{a} - \Omega_{23})\hat{\sigma}_{3-}e^{i\Omega_{12}t}\right] + \text{h.c.} \tag{A.9}$$

For $\Omega_{12} \gg g$ and $\Omega_{23} > \kappa$ the terms in the Hamiltonian oscillate very fast. This allows to derive the effective Hamiltonian according to the technique in [128]:

$$H_{eff} \overset{RWA}{\simeq} \frac{1}{2\Omega_{12}}\{-\left[g^2\hat{a}^\dagger\hat{a} + \Omega_{23}^2 + (g\Omega_{23}\hat{a} + \text{h.c.})\right]\hat{\sigma}_{++} \tag{A.10}$$

$$+ \left[g^2\hat{a}^\dagger\hat{a} + \Omega_{23}^2 - (g\Omega_{23}\hat{a} + \text{h.c.})\right]\hat{\sigma}_{--}\}$$

A.2. Generation of Schrödinger-cat state

Defining

$$\delta = \frac{g^2}{2\Omega_{12}}$$

$$\theta = \frac{\Omega_{23}^2}{2\Omega_{12}}$$

$$\lambda = \frac{g\Omega_{23}}{2\Omega_{12}}$$

(A.11)

and inserting this into the effective Hamiltonian for the strong ground state coupling leads to:

$$H_{\text{eff}} \simeq -\left[\delta\hat{a}^\dagger\hat{a} + \theta + (\lambda\hat{a} + \text{h.c.})\right]\hat{\sigma}_{++} - \left[-\delta\hat{a}^\dagger\hat{a} - \theta + (\lambda\hat{a} + \text{h.c.})\right]\hat{\sigma}_{--}$$

(A.12)

Using a unitary transformation of the form

$$U_T = \exp\left(i\delta t\hat{a}^\dagger\hat{a}\hat{\sigma}_{++} - i\delta t\hat{a}^\dagger\hat{a}\hat{\sigma}_{--}\right)$$

(A.13)

the Hamiltonian results to:

$$H_T \simeq -\theta\left(\hat{\sigma}_{++} - \hat{\sigma}_{--}\right) - \left(\lambda\hat{a}e^{i\delta t} + \text{h.c.}\right)\hat{\sigma}_{++} - \left(\lambda\hat{a}e^{-i\delta t} + \text{h.c.}\right)\hat{\sigma}_{--}.$$

(A.14)

The time evolution operator is then given by:

$$U(t) = exp\left(-i\int_0^t H_T(t')dt'\right)$$

(A.15)

$$= exp\left[i\theta t(\hat{\sigma}_{++} - \hat{\sigma}_{--})\right]exp\left\{\left(\alpha_+^*\hat{a} + \text{h.c.}\right)\hat{\sigma}_{++} + \left(\alpha_-^*\hat{a} + \text{h.c.}\right)\hat{\sigma}_{--}\right\}$$

(A.16)

with

$$\alpha_\pm = \pm\frac{\lambda}{\delta}\left(e^{\mp i\delta t} - 1\right) = \pm\frac{\Omega_{23}}{g}\left(e^{\mp\frac{ig^2 t}{2\Omega_{12}}} - 1\right)$$

(A.17)

Starting from the initial atom-cavity state $|1,0\rangle = \frac{1}{\sqrt{2}}\left(|+\rangle + |-\rangle\right)|0\rangle$ the evolved state at time t will be:

$$|\Psi(t)\rangle = U(t)|1,0\rangle = \frac{1}{\sqrt{2}}U(t)\left(|+\rangle + |-\rangle\right)|0\rangle$$

$$|\Psi(t)\rangle = \frac{1}{\sqrt{2}}\left(e^{i\theta t}|+\rangle|\alpha_+\rangle + e^{-i\theta t}|-\rangle|\alpha_-\rangle\right)$$

(A.18)

$$|\Psi(t)\rangle = \frac{1}{2}\left[|1\rangle\left(e^{i\theta t}|\alpha_+\rangle + e^{-i\theta t}|\alpha_-\rangle\right) + |2\rangle\left(e^{i\theta t}|\alpha_+\rangle - e^{-i\theta t}|\alpha_-\rangle\right)\right]$$

An atomic state detection in the bare atom basis projects the system now into one of two Schrödinger cat states.

A.3. Decay rates

The decay rates can be determined via Fermi's golden rule. $\left|\Psi_n^0\right\rangle$ denotes the n'th dark state and $\left|\Psi_n^{(\pm)}\right\rangle$ the n'th bright state as defined in Equation A.3 and Equation A.4. Because the dark states don't contain a component of an excited atomic state only the cavity field component can decay:

$$
\begin{aligned}
\Gamma_{\left|\Psi_n^0\right\rangle \to \left|\Psi_{n-1}^0\right\rangle} &= \left|\left\langle \Psi_{n-1}^0 \right| \sqrt{\kappa} a \left| \Psi_n^0 \right\rangle\right|^2 \\
&= \frac{\kappa n \left[g^2 (n-1) + \Omega_{23}^2 \right]}{\left(g^2 n + \Omega_{23}^2 \right)}
\end{aligned}
\tag{A.19}
$$

The same calculation for the decay from dark states to bright states results in:

$$
\begin{aligned}
\Gamma_{\left|\Psi_n^0\right\rangle \to \left|\Psi_{n-1}^\pm\right\rangle} &= \left|\left\langle \Psi_{n-1}^\pm \right| \sqrt{\kappa} a \left| \Psi_n^0 \right\rangle\right|^2 \\
&= \kappa N_n^2 N_{n-1,\pm}^2 \left| \left[g \Omega_{23} \sqrt{n} \sqrt{n-1} - g \Omega_{23} \sqrt{n} \sqrt{n-1} \right]\right|^2 = 0
\end{aligned}
\tag{A.20}
$$

Therefore, there is no decay from the dark states to bright states.

B. Clock state EIT
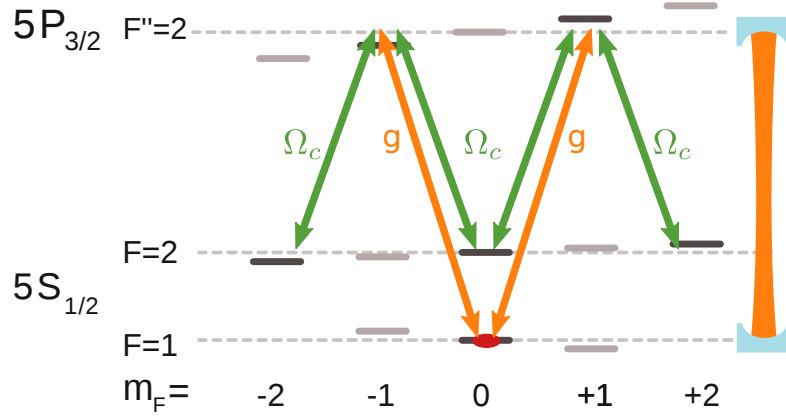
Figure B.1: Level scheme for clock state CEIT. Initially the population is prepared in state $|F = 1, m_F = 0\rangle$. The laser polarizations are horizontal for the probe laser and vertical for the control laser.

The width of the central EIT feature in CEIT is for low driving dominated by the decay rate of the first dark state, which can be described by:

$$\Gamma_{\Psi_1^0} = \frac{\Omega_c^2}{g^2 + \Omega_c^2}\kappa + \gamma_{\text{deph}} \tag{B.1}$$

where γ_{deph} is the dephasing rate between the two ground states and Ω_c the Rabi frequency of the classical laser driving the atom. This means for low Ω_c, the width of the EIT converges towards the dephasing rate, because the first term vanishes asymptotically. This dephasing rate is mainly given by magnetic field fluctuations, that *jitter* the energy of the Zeeman substates and therefore the energy of the ground states randomly. For the transitions used in Section 5.2.1, this lead to a measured dephasing rate of $\gamma_{\text{deph}}/2\pi = 64(1)\,\text{kHz}$ [53]. The ground states used for that experiment exhibited a difference in the magnetic quantum number of one. The experiments in this chapter now present CEIT, where the two ground states both have the magnetic quantum number zero and therefore do not shift in magnetic fields to first order. The magnetic-field insensitive pairs of states are often referred to as clock states. The level scheme is shown in Figure B.1. In contrast to the other experiments within this thesis, the probe laser drives both polarization eigenmodes of the cavity because its polarization is linear horizontal. Also the classical laser beam irradiating the atom is in linear vertical polarization. This leads to two outer Λ-systems with a difference of two in the magnetic quantum number and one inner Λ-system with the ground states $|F = 1, m_F = 0\rangle$ and $|F = 2, m_F = 0\rangle$. When the frequency of the probing beam is scanned, this leads to the spectrum in Figure B.2.
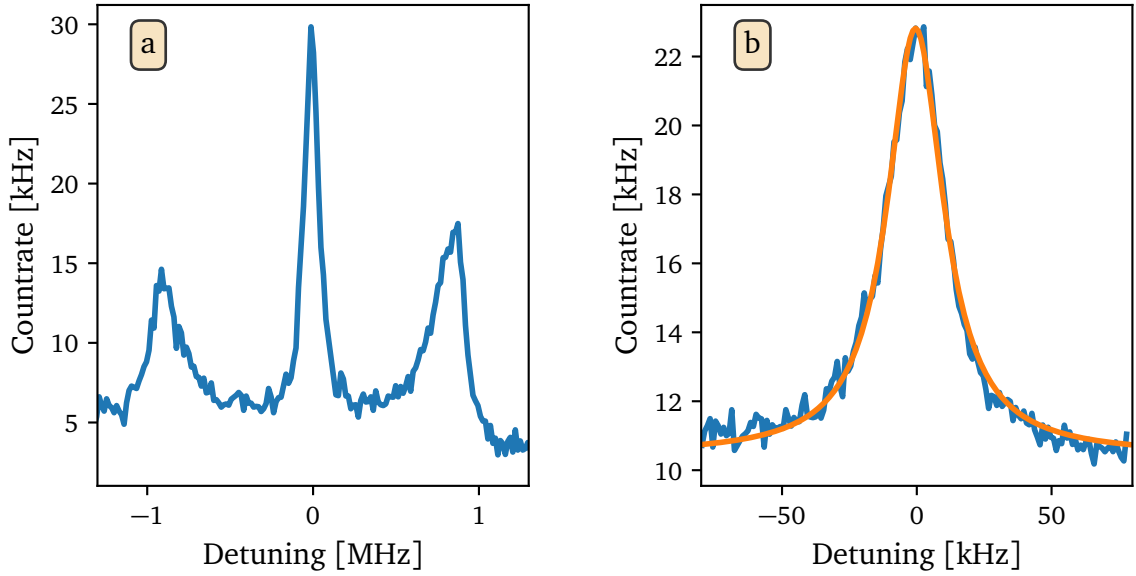
Figure B.2: (a) shows the spectrum of the three central EIT peaks corresponding to transitions from $|F = 1, m_F = 0\rangle$ to $|F = 2, m_F = -2\rangle$, $|F = 2, m_F = 0\rangle$, $|F = 2, m_F = 2\rangle$ (left to right). (b) shows the central peak for a very low control field strength. A Lorentzian fit reveals a half width of $\sigma = 12.7(2)\,$kHz.
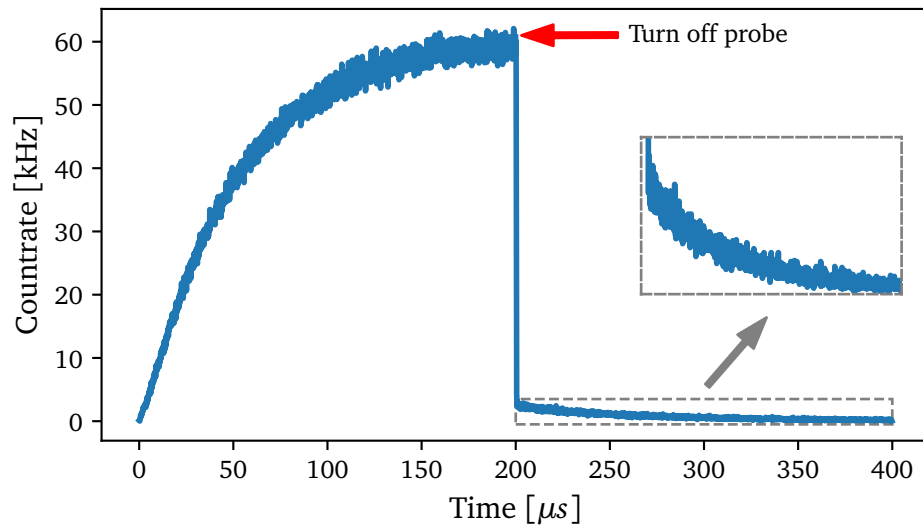
Figure B.3: Countrate of photons over time. The probe was enable at time $t = 0$ and disabled at $t = 200\,\mu$s. The inset shows a zoom to the decay of the field, as indicated by the gray box.

Part (a) shows three peaks, corresponding to the three Λ-systems mentioned. The width in this figure was still limited by Ω_c. Part (b) shows a spectrum of only the inner peak for a measurement with very low Ω_c. The peak is as narrow as $\sigma = 12.7(2)\,$kHz. Driving now on this narrow CEIT feature leads to an interesting behavior in the time domain, which

can be seen in Figure B.3. The probe is enabled at time $t = 0$ and it takes an extremely long time until it reaches full transmission. This can be explained by the narrowness of the EIT window. When the probe is turned on suddenly it exhibits a very broad spectrum of frequencies as is given by the Fourier-theorem. The EIT window then only allows the low frequency components to enter the system. It acts as a low-pass filter. In other words, it is also possible to say, that the transmission needs a long time to build up, because the system needs a long time to evolve into the dark superposition state. When the probe light is then turned off at $t = 200\,\mu s$, the most of the transmission falls off with the cavity decay constant κ, as if it would be an empty cavity. This is due to the fact, that higher excitation rungs in the dark state ladder almost decay like the empty cavity would (see also Equation A.19). A small fraction slowly falls off with the same time constant as the build-up process. This is due to the slow decay from the first dark state of the cavity EIT ladder. Shaping the input light field as such, that it would only excite the first dark state in e.g. a π-pulse, would lead to a significant slowing down of the light by a single atom.

C. Multi-mode closed cycle

This chapter presents very first and preliminary results on the closed cycling system with two cavity modes as discussed shortly in Section 7. There, the system is coherently closed via in total four different cavity modes, of which two are resonant to the D2-line of rubidium and two are resonant to the D1-line of rubidium. At each frequency two different polarization eigenmodes of the cavity are used, one in σ^+ and one in σ^-. In a first measurement, the polarization modes were not distinguished, meaning that effectively only two modes of the cavity are used, namely the ones with a different wavelength. Furthermore the coupling constants of both were almost equal at $\approx 10\,\mathrm{MHz}$. The system is then driven by two classical beams transversely addressing the atom and therefore closing the system. This leads to a continuous production of photons in both cavity modes, which is depicted in Figure C.1(a). The figure shows the time evolution of
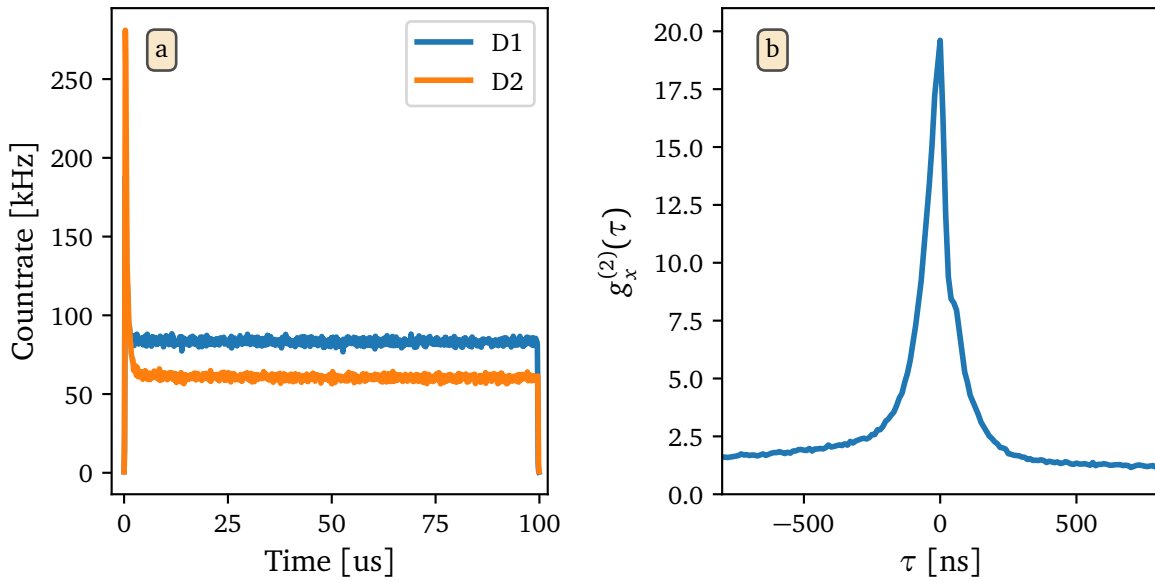
Figure C.1: (a) shows the photon detection rate of both considered cavity modes over time. (b) shows the cross-correlation function as defined in Equation C.1.

the photon detection rate behind the cavity for light stemming from the D1 and the D2 cavity mode (the atom is strongly coupled to both with its D1 and D2 line). The classical transverse laser beams are enabled at time $t = 0$. After the output light field shows initially a transient behavior, the photon rate stays constant for the full measurement duration of $100\,\mu\mathrm{s}$, after which the classical transverse driving fields were turned off. This is remarkable and indicates, that light is generated while the excited state of the atom and therefore spontaneous decay into uncoupled levels is avoided. The photon rate of D1-light at $795\,\mathrm{nm}$ and of D2-light at $780\,\mathrm{nm}$ evolve in parallel after the transient. As it is a completely closed cycle the photons are always created in the same amount, which means this difference reflects the difference in the total detection efficiency from cavity photon to actual detection. This also means, that photons are created in pairs,

which can be seen in Figure C.1(b), which shows the photon cross correlation function $g_x^{(2)}(\tau)$, which is defined in analogy to the ordinary photon correlation function but for one photon of each cavity mode:

$$g_x^{(2)}(\tau) = \begin{cases} \langle \hat{a}^\dagger \hat{b}^\dagger(\tau)\hat{b}(\tau)\hat{a}\rangle / \langle \hat{a}^\dagger \hat{a}\rangle \langle \hat{b}^\dagger \hat{b}\rangle & \tau > 0 \\ \langle \hat{b}^\dagger \hat{a}^\dagger(\tau)\hat{a}(\tau)\hat{b}\rangle / \langle \hat{a}^\dagger \hat{a}\rangle \langle \hat{b}^\dagger \hat{b}\rangle & \tau < 0 \end{cases} \tag{C.1}$$

with $\hat{a}^\dagger(\hat{a})$ and $\hat{b}^\dagger(\hat{b})$ the creation (annihilation) operators of the two cavity modes. For independent photons the cross-correlation function has a value of constant one. The measurement reveals that photons are indeed emitted predominantly in pairs. In theory these pairs should be polarization entangled, which was not measured yet because the state tomography setup was in the making and not yet finished as of writing this.

References

[1] S. Gleyzes, S. Kuhr, C. Guerlin, J. Bernu, S. Deléglise, U. Busk Hoff, M. Brune, J.-M. Raimond, and S. Haroche, "Quantum Jumps of Light Recording the Birth and Death of a Photon in a Cavity", *Nature* **446** (7133), 297–300, 2007.

[2] C. Guerlin, J. Bernu, S. Deléglise, C. Sayrin, S. Gleyzes, S. Kuhr, M. Brune, J.-M. Raimond, and S. Haroche, "Progressive Field-State Collapse and Quantum Non-Demolition Photon Counting", *Nature* **448** (7156), 889–893, 2007.

[3] M. Planck, "Ueber Das Gesetz Der Energieverteilung Im Normalspectrum", *Annalen der Physik* **309** (3), 553–563, 1901.

[4] P. Lenard, "Ueber Die Lichtelektrische Wirkung", *Annalen der Physik* **313** (5), 149–198, 1902.

[5] A. Einstein, "Über Einen Die Erzeugung Und Verwandlung Des Lichtes Betreffenden Heuristischen Gesichtspunkt", *Annalen der Physik* **322** (6), 132–148, 1905.

[6] A. H. Compton, "A Quantum Theory of the Scattering of X-Rays by Light Elements", *Physical Review* **21** (5), 483–502, 1923.

[7] R. P. Feynman, *QED: The Strange Theory of Light and Matter*, Princeton University Press, 2006, 194 pp.

[8] E. Schrödinger, "Are There Quantum Jumps? Part II", *The British Journal for the Philosophy of Science* **3** (11), 233–242, 1952.

[9] S. Nußmann, K. Murr, M. Hijlkema, B. Weber, A. Kuhn, and G. Rempe, "Vacuum-Stimulated Cooling of Single Atoms in Three Dimensions", *Nature Physics* **1** (2), 122–125, 2005.

[10] A. Kubanek, M. Koch, C. Sames, A. Ourjoumtsev, P. W. H. Pinkse, K. Murr, and G. Rempe, "Photon-by-Photon Feedback Control of a Single-Atom Trajectory", *Nature* **462** (7275), 898–901, 2009.

[11] P. W. H. Pinkse, T. Fischer, P. Maunz, and G. Rempe, "Trapping an Atom with Single Photons", *Nature* **404** (6776), 365–368, 2000.

[12] C. J. Hood, T. W. Lynn, A. C. Doherty, A. S. Parkins, and H. J. Kimble, "The Atom-Cavity Microscope: Single Atoms Bound in Orbit by Single Photons", *Science* **287** (5457), 1447–1453, 2000.

[13] R. J. Thompson, G. Rempe, and H. J. Kimble, "Observation of Normal-Mode Splitting for an Atom in an Optical Cavity", *Physical Review Letters* **68** (8), 1132–1135, 1992.

[14] T. H. Maiman, "Stimulated Optical Radiation in Ruby", *Nature* **187** (4736), 493–494, 1960.

[15] S. Haroche and J.-M. Raimond, *Exploring the Quantum: Atoms, Cavities, and Photons*, Oxford Graduate Texts, Oxford, New York: Oxford University Press, 2013, 616 pp.

[16] K. M. Birnbaum, A. Boca, R. Miller, A. D. Boozer, T. E. Northup, and H. J. Kimble, "Photon Blockade in an Optical Cavity with One Trapped Atom", *Nature* **436** (7047), 87–90, 2005.

[17] C. Hamsen, K. N. Tolazzi, T. Wilk, and G. Rempe, "Two-Photon Blockade in an Atom-Driven Cavity QED System", *Physical Review Letters* **118** (13), 133604, 2017.

[18] A. Kuhn, M. Hennrich, and G. Rempe, "Deterministic Single-Photon Source for Distributed Quantum Networking", *Physical Review Letters* **89** (6), 067901, 2002.

[19] H. P. Specht, C. Nölleke, A. Reiserer, M. Uphoff, E. Figueroa, S. Ritter, and G. Rempe, "A Single-Atom Quantum Memory", *Nature* **473** (7346), 190–193, 2011.

[20] S. Ritter, C. Nölleke, C. Hahn, A. Reiserer, A. Neuzner, M. Uphoff, M. Mücke, E. Figueroa, J. Bochmann, and G. Rempe, "An Elementary Quantum Network of Single Atoms in Optical Cavities", *Nature* **484** (7393), 195–200, 2012.

[21] B. Hacker, S. Welte, G. Rempe, and S. Ritter, "A Photon–Photon Quantum Gate Based on a Single Atom in an Optical Resonator", *Nature* **536** (7615), 193–196, 2016.

[22] G. Alzetta, A. Gozzini, L. Moi, and G. Orriols, "An Experimental Method for the Observation of r.f. Transitions and Laser Beat Resonances in Oriented Na Vapour", *Il Nuovo Cimento B* **36** (1), 5–20, 1976.

[23] K.-J. Boller, A. İmamoğlu, and S. E. Harris, "Observation of Electromagnetically Induced Transparency", *Physical Review Letters* **66** (20), 2593–2596, 1991.

[24] S. E. Harris, "Electromagnetically Induced Transparency with Matched Pulses", *Physical Review Letters* **70** (5), 552–555, 1993.

[25] S. E. Harris, "Electromagnetically Induced Transparency", *Physics Today* **50** (7), 36, 1997.

[26] M. Fleischhauer, A. İmamoğlu, and J. P. Marangos, "Electromagnetically Induced Transparency: Optics in Coherent Media", *Reviews of Modern Physics* **77** (2), 633–673, 2005.

[27] L. V. Hau, S. E. Harris, Z. Dutton, and C. H. Behroozi, "Light Speed Reduction to 17 Metres per Second in an Ultracold Atomic Gas", *Nature* **397** (6720), 594–598, 1999.

[28] M. M. Kash, V. A. Sautenkov, A. S. Zibrov, L. Hollberg, G. R. Welch, M. D. Lukin, Y. Rostovtsev, E. S. Fry, and M. O. Scully, "Ultraslow Group Velocity and Enhanced Nonlinear Optical Effects in a Coherently Driven Hot Atomic Gas", *Physical Review Letters* **82** (26), 5229–5232, 1999.

[29] C. Liu, Z. Dutton, C. H. Behroozi, and L. V. Hau, "Observation of Coherent Optical Information Storage in an Atomic Medium Using Halted Light Pulses", *Nature* **409** (6819), 490–493, 2001.

[30] T. Chanelière, D. N. Matsukevich, S. D. Jenkins, S.-Y. Lan, T. a. B. Kennedy, and A. Kuzmich, "Storage and Retrieval of Single Photons Transmitted between Remote Quantum Memories", *Nature* **438** (7069), 833–836, 2005.

[31] D. Tiarks, S. Schmidt, G. Rempe, and S. Dürr, "Optical π Phase Shift Created with a Single-Photon Pulse", *Science Advances* **2** (4), e1600036, 2016.

[32] S. Baur, D. Tiarks, G. Rempe, and S. Dürr, "Single-Photon Switch Based on Rydberg Blockade", *Physical Review Letters* **112** (7), 073901, 2014.

[33] D. Tiarks, S. Baur, K. Schneider, S. Dürr, and G. Rempe, "Single-Photon Transistor Using a Förster Resonance", *Physical Review Letters* **113** (5), 053602, 2014.

[34] H. Gorniaczyk, C. Tresp, J. Schmidt, H. Fedder, and S. Hofferberth, "Single-Photon Transistor Mediated by Interstate Rydberg Interactions", *Physical Review Letters* **113** (5), 053601, 2014.

[35] D. Tiarks, S. Schmidt-Eberle, T. Stolz, G. Rempe, and S. Dürr, "A Photon–Photon Quantum Gate Based on Rydberg Interactions", *Nature Physics* **15** (2), 124–126, 2019.

[36] M. Mücke, E. Figueroa, J. Bochmann, C. Hahn, K. Murr, S. Ritter, C. J. Villas-Boas, and G. Rempe, "Electromagnetically Induced Transparency with Single Atoms in a Cavity", *Nature* **465** (7299), 755–758, 2010.

[37] M. Mücke, "Elektromagnetisch Induzierte Transparenz Mit Einem Einzelnen Atom", Dissertation, München: Technische Universität München, 2011.

[38] M. Albert, A. Dantan, and M. Drewsen, "Cavity Electromagnetically Induced Transparency and All-Optical Switching Using Ion Coulomb Crystals", *Nature Photonics* **5** (10), 633–636, 2011.

[39] T. Kampschulte, W. Alt, S. Brakhane, M. Eckstein, R. Reimann, A. Widera, and D. Meschede, "Optical Control of the Refractive Index of a Single Atom", *Physical Review Letters* **105** (15), 153603, 2010.

[40] T. Kampschulte, "Coherently Driven Three-Level Atoms in an Optical Cavity", Dissertation, Universität Bonn, 2012.

[41] J. A. Souza, E. Figueroa, H. Chibani, C. J. Villas-Boas, and G. Rempe, "Coherent Control of Quantum Fluctuations Using Cavity Electromagnetically Induced Transparency", *Physical Review Letters* **111** (11), 113602, 2013.

[42] M. O. Scully and M. S. Zubairy, *Quantum Optics*, Cambridge University Press, 1997, 659 pp.

[43] E. Jaynes and F. Cummings, "Comparison of Quantum and Semiclassical Radiation Theories with Application to the Beam Maser", *Proceedings of the IEEE* **51** (1), 89–109, 1963.

[44] B. W. Shore and P. L. Knight, "The Jaynes-Cummings Model", *Journal of Modern Optics* **40** (7), 1195–1238, 1993.

[45] A. Kubanek, A. Ourjoumtsev, I. Schuster, M. Koch, P. W. H. Pinkse, K. Murr, and G. Rempe, "Two-Photon Gateway in One-Atom Cavity Quantum Electrodynamics", *Physical Review Letters* **101** (20), 203602, 2008.

[46] H. Chibani, "Photon Blockade with Memory and Slow Light Using a Single Atom in an Optical Cavity", Dissertation, München: Technische Universität München, 2016.

[47] J. Neumeier, "Optical Heterodyne Detection of a Cross-Phase Modulation Mediated by a Single Atom", Master thesis, Ludwig-Maximilians Universität, 2018.

[48] M. Lax, "Formal Theory of Quantum Fluctuations from a Driven State", *Physical Review* **129** (5), 2342–2348, 1963.

[49] J. R. Johansson, P. D. Nation, and F. Nori, "QuTiP 2: A Python Framework for the Dynamics of Open Quantum Systems", *Computer Physics Communications* **184** (4), 1234–1240, 2013.

[50] M. Koch, "Classical and Quantum Dynamics of a Strongly Coupled Atom-Cavity System", Dissertation, München: Technische Universität München, 2011.

[51] C. Sames, "Atomic Antiresonance and Parametric Feedback in a Strongly Coupled Atom-Cavity Quantum System", Dissertation, München: Technische Universität München, 2018.

[52] R. W. P. Drever, J. L. Hall, F. V. Kowalski, J. Hough, G. M. Ford, A. J. Munley, and H. Ward, "Laser Phase and Frequency Stabilization Using an Optical Resonator", *Applied Physics B* **31** (2), 97–105, 1983.

[53] C. Hamsen, "Interacting Photons in a Strongly Coupled Atom-Cavity System", Dissertation, München: Technische Universität München, 2017.

[54] D. A. Steck, "Rubidium 87 D Line Data", online at http://steck.us/alkalidata (revision 2.1.5, 13 January 2015).

[55] R. Grimm, M. Weidemüller, and Y. B. Ovchinnikov, "Optical Dipole Traps for Neutral Atoms", 1999, arXiv: `physics/9902072`.

[56] K. Murr, S. Nußmann, T. Puppe, M. Hijlkema, B. Weber, S. C. Webster, A. Kuhn, and G. Rempe, "Three-Dimensional Cavity Cooling and Trapping in an Optical Lattice", *Physical Review A* **73** (6), 063415, 2006.

[57] A. C. Eckl, "High-Resolution Imaging of a Single Atom Strongly Coupled to a Cavity", Master thesis, Ludwig-Maximilians Universität, 2013.

[58] C. Shannon, "Communication in the Presence of Noise", *Proceedings of the IRE* **37** (1), 10–21, 1949.

[59] The HDF Group, *Hierarchical Data Format, Version 5*.

[60] J. A. Barker, "A Quantum-statistical Monte Carlo Method; Path Integrals with Boundary Conditions", *The Journal of Chemical Physics* **70** (6), 2914–2918, 1979.

[61] R. Gehr, J. Volz, G. Dubois, T. Steinmetz, Y. Colombe, B. L. Lev, R. Long, J. Estève, and J. Reichel, "Cavity-Based Single Atom Preparation and High-Fidelity Hyperfine State Readout", *Physical Review Letters* **104** (20), 203602, 2010.

[62] J. Bochmann, M. Mücke, C. Guhl, S. Ritter, G. Rempe, and D. L. Moehring, "Lossless State Detection of Single Neutral Atoms", *Physical Review Letters* **104** (20), 203601, 2010.

[63] B. Wang, "Fluorescence State Detection of Single Atoms on a Non-Cycling Transition", Master thesis, Technische Universität München, 2017.

[64] A. Neuzner, "Resonance Fluorescence of an Atom Pair in an Optical Resonator", Dissertation, München: Technische Universität München, 2016.

[65] C. Monroe, D. M. Meekhof, B. E. King, W. M. Itano, and D. J. Wineland, "Demonstration of a Fundamental Quantum Logic Gate", *Physical Review Letters* **75** (25), 4714–4717, 1995.

[66] A. D. Boozer, "Theory of Raman Transitions in Cavity QED", *Physical Review A* **78** (3), 033406, 2008.

[67] A. Reiserer, S. Ritter, and G. Rempe, "Nondestructive Detection of an Optical Photon", *Science* **342** (6164), 1349–1351, 2013.

[68] D. J. Heinzen and D. J. Wineland, "Quantum-Limited Cooling and Detection of Radio-Frequency Oscillations by Laser-Cooled Ions", *Physical Review A* **42** (5), 2977–2994, 1990.

[69] A. M. Kaufman, B. J. Lester, and C. A. Regal, "Cooling a Single Atom in an Optical Tweezer to Its Quantum Ground State", *Physical Review X* **2** (4), 041014, 2012.

[70] A. Reiserer, C. Nölleke, S. Ritter, and G. Rempe, "Ground-State Cooling of a Single Atom at the Center of an Optical Cavity", *Physical Review Letters* **110** (22), 223003, 2013.

[71] A. J. Merriam, S. J. Sharpe, M. Shverdin, D. Manuszak, G. Y. Yin, and S. E. Harris, "Efficient Nonlinear Frequency Conversion in an All-Resonant Double-Lambda System", *Physical Review Letters* **84** (23), 5308–5311, 2000.

[72] Y. O. Dudin and A. Kuzmich, "Strongly Interacting Rydberg Excitations of a Cold Atomic Gas", *Science* **336** (6083), 887–889, 2012.

[73] A. Maser, B. Gmeiner, T. Utikal, S. Götzinger, and V. Sandoghdar, "Few-Photon Coherent Nonlinear Optics with a Single Molecule", *Nature Photonics* **10** (7), 450–453, 2016.

[74] F. Ripka, H. Kübler, R. Löw, and T. Pfau, "A Room-Temperature Single-Photon Source Based on Strongly Interacting Rydberg Atoms", *Science* **362** (6413), 446–449, 2018.

[75] C. Weinzetl, J. Görlitz, J. N. Becker, I. A. Walmsley, E. Poem, J. Nunn, and C. Becher, "Coherent Control and Wave Mixing in an Ensemble of Silicon-Vacancy Centers in Diamond", *Physical Review Letters* **122** (6), 2019.

[76] N. Bohr, "I. *On the Constitution of Atoms and Molecules*", *The London, Edinburgh, and Dublin Philosophical Magazine and Journal of Science* **26** (151), 1–25, 1913.

[77] B. Misra and E. C. G. Sudarshan, "The Zeno's Paradox in Quantum Theory", *Journal of Mathematical Physics* **18** (4), 756–763, 1977.

[78] B. R. Mollow, "Power Spectrum of Light Scattered by Two-Level Systems", *Physical Review* **188** (5), 1969–1975, 1969.

[79] J. T. Höffges, H. W. Baldauf, T. Eichler, S. R. Helmfrid, and H. Walther, "Heterodyne Measurement of the Fluorescent Radiation of a Single Trapped Ion", *Optics Communications* **133** (1), 170–174, 1997.

[80] W. B. Case, "Wigner Functions and Weyl Transforms for Pedestrians", *American Journal of Physics* **76** (10), 937–946, 2008.

[81] C. J. Villas-Boas, K. N. Tolazzi, B. Wang, C. Ianzano, and G. Rempe, "Continuous Generation of Quantum Light from a Single Ground-State Atom in an Optical Cavity", 2019, arXiv: 1906.11449 [quant-ph].

[82] C. Hamsen, K. N. Tolazzi, T. Wilk, and G. Rempe, "Strong Coupling between Photons of Two Light Fields Mediated by One Atom", *Nature Physics* **14** (9), 885, 2018.

[83] R. Loudon, "Non-Classical Effects in the Statistical Properties of Light", *Reports on Progress in Physics* **43** (7), 913–949, 1980.

[84] N. Imoto, H. A. Haus, and Y. Yamamoto, "Quantum Nondemolition Measurement of the Photon Number via the Optical Kerr Effect", *Physical Review A* **32** (4), 2287–2292, 1985.

[85] S. E. Harris and L. V. Hau, "Nonlinear Optics at Low Light Levels", *Physical Review Letters* **82** (23), 4611–4614, 1999.

[86] S. Ding, G. Maslennikov, R. Hablützel, and D. Matsukevich, "Cross-Kerr Nonlinearity for Phonon Counting", *Physical Review Letters* **119** (19), 193602, 2017.

[87] M. Lee, K. Friebe, D. A. Fioretto, K. Schüppert, F. R. Ong, D. Plankensteiner, V. Torggler, H. Ritsch, R. Blatt, and T. E. Northup, "Ion-Based Quantum Sensor for Optical Cavity Photon Numbers", *Physical Review Letters* **122** (15), 153603, 2019.

[88] M. Brune, P. Nussenzveig, F. Schmidt-Kaler, F. Bernardot, A. Maali, J. M. Raimond, and S. Haroche, "From Lamb Shift to Light Shifts: Vacuum and Subphoton Cavity Fields Measured by Atomic Phase Sensitive Detection", *Physical Review Letters* **72** (21), 3339–3342, 1994.

[89] D. I. Schuster, A. Wallraff, A. Blais, L. Frunzio, R.-S. Huang, J. Majer, S. M. Girvin, and R. J. Schoelkopf, "Ac Stark Shift and Dephasing of a Superconducting Qubit Strongly Coupled to a Cavity Field", *Physical Review Letters* **94** (12), 123602, 2005.

[90]   D. I. Schuster et al., "Resolving Photon Number States in a Superconducting Circuit", *Nature* **445** (7127), 515–518, 2007.

[91]   T. Inagaki, N. Matsuda, O. Tadanaga, M. Asobe, and H. Takesue, "Entanglement Distribution over 300 Km of Fiber", *Optics Express* **21** (20), 23241–23249, 2013.

[92]   M. Körber, O. Morin, S. Langenfeld, A. Neuzner, S. Ritter, and G. Rempe, "Decoherence-Protected Memory for a Single-Photon Qubit", *Nature Photonics* **12** (1), 18–21, 2018.

[93]   T. N. Dey and G. S. Agarwal, "Observable Effects of Kerr Nonlinearity on Slow Light", *Physical Review A* **76** (1), 015802, 2007.

[94]   M. Hosseini, S. Rebić, B. M. Sparkes, J. Twamley, B. C. Buchler, and P. K. Lam, "Memory-Enhanced Noiseless Cross-Phase Modulation", *Light: Science & Applications* **1** (12), e40, 2012.

[95]   K. M. Beck, M. Hosseini, Y. Duan, and V. Vuletić, "Large Conditional Single-Photon Cross-Phase Modulation", *Proceedings of the National Academy of Sciences* **113** (35), 9740–9744, 2016.

[96]   H. Schmidt and A. İmamoğlu, "Giant Kerr Nonlinearities Obtained by Electromagnetically Induced Transparency", *Optics letters* **21** (23), 1936–1938, 1996.

[97]   A. İmamoğlu, H. Schmidt, G. Woods, and M. Deutsch, "Strongly Interacting Photons in a Nonlinear Cavity", *Physical Review Letters* **79** (8), 1467–1470, 1997.

[98]   A. Feizpour, M. Hallaji, G. Dmochowski, and A. M. Steinberg, "Observation of the Nonlinear Phase Shift Due to Single Post-Selected Photons", *Nature Physics* **11** (11), 905–909, 2015.

[99]   Q. A. Turchette, C. J. Hood, W. Lange, H. Mabuchi, and H. J. Kimble, "Measurement of Conditional Phase Shifts for Quantum Logic", *Physical Review Letters* **75** (25), 4710–4713, 1995.

[100] J. H. Shapiro, "Single-Photon Kerr Nonlinearities Do Not Help Quantum Computation", *Physical Review A* **73** (6), 062305, 2006.

[101] W. J. Munro, K. Nemoto, and T. P. Spiller, "Weak Nonlinearities: A New Route to Optical Quantum Computation", *New Journal of Physics* **7** 137–137, 2005.

[102] A. Blais, R.-S. Huang, A. Wallraff, S. M. Girvin, and R. J. Schoelkopf, "Cavity Quantum Electrodynamics for Superconducting Electrical Circuits: An Architecture for Quantum Computation", *Physical Review A* **69** (6), 062320, 2004.

[103] G. F. Sinclair and N. Korolkova, "Effective Cross-Kerr Hamiltonian for a Nonresonant Four-Level Atom", *Physical Review A* **77** (3), 033843, 2008.

[104] Y. Hu, G.-Q. Ge, S. Chen, X.-F. Yang, and Y.-L. Chen, "Cross-Kerr-Effect Induced by Coupled Josephson Qubits in Circuit Quantum Electrodynamics", *Physical Review A* **84** (1), 012329, 2011.

[105] P. Grangier, J. A. Levenson, and J.-P. Poizat, "Quantum Non-Demolition Measurements in Optics", *Nature* **396** (6711), 537–542, 1998.

[106] M. D. Lukin, "Colloquium: Trapping and Manipulating Photon States in Atomic Ensembles", *Reviews of Modern Physics* **75** (2), 457–472, 2003.

[107] R. W. Boyd, *Nonlinear Optics*, 3rd ed, Amsterdam ; Boston: Academic Press, 2008, 613 pp.

[108] S. Rebic, "An Investigation of Giant Kerr Nonlinearity", Thesis, The University of Auckland, 2002.

[109] M. Hosseini, K. M. Beck, Y. Duan, W. Chen, and V. Vuletić, "Partially Nondestructive Continuous Detection of Individual Traveling Optical Photons", *Physical Review Letters* **116** (3), 033602, 2016.

[110] J. Gambetta, A. Blais, D. I. Schuster, A. Wallraff, L. Frunzio, J. Majer, M. H. Devoret, S. M. Girvin, and R. J. Schoelkopf, "Qubit-Photon Interactions in a Cavity: Measurement-Induced Dephasing and Number Splitting", *Physical Review A* **74** (4), 042318, 2006.

[111] K. Murr, "On the Suppression of the Diffusion and the Quantum Nature of a Cavity Mode. Optical Bistability: Forces and Friction in Driven Cavities", *Journal of Physics B: Atomic, Molecular and Optical Physics* **36** (12), 2515, 2003.

[112] A. Neuzner, M. Körber, O. Morin, S. Ritter, and G. Rempe, "Interference and Dynamics of Light from a Distance-Controlled Atom Pair in an Optical Cavity", *Nature Photonics* **10** (5), 303–306, 2016.

[113] P. Virtanen et al., "SciPy 1.0–Fundamental Algorithms for Scientific Computing in Python", 2019, arXiv: `1907.10121 [physics]`.

[114] R. L. Sutherland, D. G. McLean, and S. Kirkpatrick, *Handbook of Nonlinear Optics*, 2nd ed., rev. and expanded, Optical Engineering 82, New York: Marcel Dekker, 2003, 971 pp.

[115] C. Sames, H. Chibani, C. Hamsen, P. A. Altin, T. Wilk, and G. Rempe, "Antiresonance Phase Shift in Strongly Coupled Cavity QED", *Physical Review Letters* **112** (4), 043601, 2014.

[116] J. Sinclair, D. Angulo, N. Lupu-Gladstein, K. Bonsma-Fisher, and A. M. Steinberg, "Observation of a Large, Resonant, Cross-Kerr Nonlinearity in a Free-Space Rydberg Medium", 2019, arXiv: `1906.05151`.

[117] Z.-Y. Liu, Y.-H. Chen, Y.-C. Chen, H.-Y. Lo, P.-J. Tsai, I. A. Yu, Y.-C. Chen, and Y.-F. Chen, "Large Cross-Phase Modulations at the Few-Photon Level", *Physical Review Letters* **117** (20), 203601, 2016.

[118] R. Reimann, W. Alt, T. Kampschulte, T. Macha, L. Ratschbacher, N. Thau, S. Yoon, and D. Meschede, "Cavity-Modified Collective Rayleigh Scattering of Two Atoms", *Physical Review Letters* **114** (2), 023601, 2015.

[119] K. P. Nayak, J. Wang, and J. Keloth, "Real-Time Observation of Single Atoms Trapped and Interfaced to a Nanofiber Cavity", *Physical Review Letters* **123** (21), 213602, 2019.

[120] Z. K. Minev, S. O. Mundhada, S. Shankar, P. Reinhold, R. Gutiérrez-Jáuregui, R. J. Schoelkopf, M. Mirrahimi, H. J. Carmichael, and M. H. Devoret, "To Catch and Reverse a Quantum Jump Mid-Flight", *Nature* **570** (7760), 200–204, 2019.

[121] C. Laflamme, D. Yang, and P. Zoller, "Continuous Measurement of an Atomic Current", *Physical Review A* **95** (4), 043843, 2017.

[122] U. Harbola, S. Rahav, and S. Mukamel, "Quantum Heat Engines: A Thermodynamic Analysis of Power and Efficiency", *EPL (Europhysics Letters)* **99** (5), 50005, 2012.

[123] M. H. Ansari, "Entropy Production in a Photovoltaic Cell", *Physical Review B* **95** (17), 174302, 2017.

[124] S. K. Giri and H. P. Goswami, "Geometric Phaselike Effects in a Quantum Heat Engine", *Physical Review E* **96** (5), 052129, 2017.

[125] B. Casabone, K. Friebe, B. Brandstätter, K. Schüppert, R. Blatt, and T. E. Northup, "Enhanced Quantum Interface with Collective Ion-Cavity Coupling", *Physical Review Letters* **114** (2), 023602, 2015.

[126] M. Endres, H. Bernien, A. Keesling, H. Levine, E. R. Anschuetz, A. Krajenbrink, C. Senko, V. Vuletic, M. Greiner, and M. D. Lukin, "Atom-by-Atom Assembly of Defect-Free One-Dimensional Cold Atom Arrays", *Science* **354** (6315), 1024–1027, 2016.

[127] D. Barredo, V. Lienhard, S. de Léséleuc, T. Lahaye, and A. Browaeys, "Synthetic Three-Dimensional Atomic Structures Assembled Atom by Atom", *Nature* **561** (7721), 79–82, 2018.

[128] D. F. James and J. Jerke, "Effective Hamiltonian Theory and Its Applications in Quantum Information", *Canadian Journal of Physics* **85** (6), 625–632, 2007.

Publication List

- *Giant Cross Kerr Nonlinearity Induced by a Single Atom*
  In preparation

- *Continuous quantum light from a dark atom*
  K. N. Tolazzi, B. Wang, C. Ianzano, J. Neumeier, C. J. Villas-Boas, G. Rempe
  In preparation

- *Continuous generation of quantum light from a single
  ground-state atom in an optical cavity*
  C. J. Villas-Boas, K. N. Tolazzi, B. Wang, C. Ianzano, G. Rempe
  arXiv 1906.11449 (quant-ph), accepted in Physical Review Letters

- *Strong coupling between photons of two light fields mediated by one atom*
  C. Hamsen, K. N. Tolazzi, T. Wilk, G. Rempe
  Nature Physics **14**, 885-889 (2018)

- *Starke Kopplung zwischen Photonen*
  C. Hamsen, K. N. Tolazzi, T. Wilk, G. Rempe
  Physik in unserer Zeit **49**, 216-217 (2018)

- *Two-Photon Blockade in an Atom-Driven Cavity QED System*
  C. Hamsen, K. N. Tolazzi, T. Wilk, G. Rempe
  Physical Review Letters **118**, 133604 (2017)

- *A single-atom heat engine*
  J. Roßnagel, S. T. Dawkins, K. N. Tolazzi, O. Abah, E. Lutz, F. Schmidt-Kaler,
  K. Singer
  Science **352**, 325-329 (2016)

- *Fast thermometry for trapped ions using dark resonances*
  J. Roßnagel, K. N. Tolazzi, F. Schmidt-Kaler, K. Singer
  New Journal of Physics **17**, 045004 (2015)

- *Nano-Motor aus einem einzelnen Atom*
  J. Roßnagel, K. N. Tolazzi, O. Abah, E. Lutz, F Schmidt-Kaler, K. Singer
  GIT Labor-Fachzeitschrift **6**, 51 (2014)

Acknowledgments

This work would not have been possible without the great people that accompanied me and helped me through all the ups and downs of a PhD during the past five years.

First I want to thank my supervisor Gerhard Rempe for giving me the opportunity to work at such a wonderful institution as the MPQ. I want to express my deep gratitude towards him for his constant support and the full freedom to follow my curiosity. I especially appreciate that he always plays devil's advocate in the discussions and points his finger to any weak points in an argumentation until it is bullet-proof. Also his desire for intuitive explanations greatly helped to improve the understanding of physics.

I also want to thank the *old crew* of the experiment: Tatjana Wilk, my supervisor at the beginning, who always had an open door for all our sorrows and introduced me into the world of science slams. Gang Li, a visiting professor from China, with whom I shared many walks and interesting discussions. And my old master student and now roommate Jonas Neumeier, whom I want to thank, among countless other things, for showing me how to deal with plants.

I also owe a lot to the *new crew* of the Cavies experiment: Bo Wang, who is maybe the most creative person I know, the person with whom I shared plenty of often frustrating time in the lab and who helped me countless times in understanding new phenomena with his intuitive views on physics. Chris Ianzano whose contributions for the success of this thesis are essential. Was it measuring with me in the lab, writing text for papers, getting *Math-coffee* together, training in the gym or proof-reading my thesis, he was always there for me. Saibin Zhou, our newest team member, for providing me with an endless stream of sweets, Chinese hot sauces and being such a gentle person.
I also want to thank our technicians Tobias Urban, Florian Furchtsam, Johannes Siegl and Thomas Wiesmeier for their fast and competent help in all situations. They are a big factor in the success of any experiment.

I also want to thank my predecessor Christoph Hamsen for the wonderful time we had while working in the lab together, playing kicker and having political discussions and especially for teaching me all the little quirks of the experiment and so much more. We shared many memorable moments in and outside of MPQ.

A special thanks goes to Matthias Körber, for so many discussions, scientifically and non-scientifically and so many fun evenings together. And I especially want to thank him for therapeutic table tennis and for welcoming me into his home when I needed it.

I would also like to thank my office neighbor Isabel Rabey for bringing sunshine into the office and for precious advice in a difficult time. I also immensely enjoyed our *Warenannahme-walks*.

I cannot thank my family enough for their constant support in so many respects throughout all these years, that only enabled me to perform research. They shaped me into the person I am today.

Finally I want to thank Nathalie for all the change and the joy she brought into my life.

Thank you all!